# An Approach to Incorporate Additive Manufacturing and Rapid Prototype Testing for Aircraft Conceptual Design to Improve MDO Effectiveness

Alex M. Friedman

Thesis submitted to the faculty of the Virginia Polytechnic Institute and State University in partial fulfillment of the requirements for the degree of

Master of Science
In
Aerospace Engineering

Pradeep Raj, Chair
Seongim S. Choi
William H. Mason

May 1, 2015
Blacksburg, Virginia

Keywords: Additive Manufacturing, Surrogate-Based Optimization, Aircraft Conceptual Design Effectiveness, Design of Experiments

# An Approach to Incorporate Additive Manufacturing and Rapid Prototype Testing for Aircraft Conceptual Design to Improve MDO Effectiveness

Alex M. Friedman

## ABSTRACT

The primary objectives of this work are two-fold. First, additive manufacturing (AM) and rapid prototype (RP) testing are evaluated for use in production of a wind tunnel (WT) models. Second, an approach was developed to incorporate stability and control (S&C) WT data into aircraft conceptual design multidisciplinary design optimization (MDO). Both objectives are evaluated in terms of data quality, time, and cost.

FDM™ and PolyJet AM processes were used for model production at low cost and time. Several models from a representative tailless configuration, ICE 101, were printed and evaluated for strength, cost and time of production. Furthermore, a NACA 0012 model with 20% chord flap was manufactured. Both models were tested in the Virginia Tech (VT) Open-Jet WT for force and moment acquisition. A $1/15^{th}$ scale ICE 101 model was prepared for manufacturing, but limits of FDM™ technology were identified for production.

An approach using WT data was adapted from traditional surrogate-based optimization (SBO), which uses computational fluid dynamics (CFD) for data generation. Split-plot experimental designs were developed for analysis of the WT SBO strategy using historical data and for WT testing of the NACA 0012. Limitations of the VT Open-Jet WT resulted in a process that was not fully effective for a MDO environment. However, resolution of ICE 101 AM challenges and higher quality data from a closed-section WT should result in a fully effective approach to incorporate AM and RP testing in an aircraft conceptual design MDO.

This material is partially based on research sponsored by Air Force Research Laboratory under agreement number FA8650-09-2-3938. The U.S. Government is authorized to reproduce and distribute reprints for Governmental purposes notwithstanding any copyright notation thereon. The views and conclusions contained herein are those of the authors and should not be interpreted as necessarily representing the official policies or endorsements, either expressed or implied, of the Air Force Research Laboratory or the U.S. Government.

# Acknowledgements

I would like to express my sincere gratitude to my advisor, Dr. Pradeep Raj, for his support and guidance through this research. Dr. Raj helped come up with an interesting research topic working with state-of-the-art technologies which I found exciting. Furthermore, with all his experience in the Aerospace field, Dr. Raj was not only able to provide technical advice for my research, but he was also able to help me grow as a professional. I always looked forward to our conversations because I knew that I would get valuable information for my future. I couldn't have asked for a better advisor to enable me to grow as an Aerospace Engineer and professional. I would also like to thank my other committee members, Dr. Seongim Choi and Dr. Bill Mason. Dr. Choi and Dr. Mason always provided challenging questions and valuable advice throughout my research.

In addition, I would like to extend my deepest gratitude to my family and friends for their support and encouragement throughout my graduate education. At the start of my graduate education I was left without funding or a research project, but with their support and advice I continued on my education and was able to work on a research topic I found both exciting and rewarding. I would also like thank my peers for their input during our weekly meetings and for their assistance with CAD modeling. In addition, I would like to thank the Aerospace and Ocean Engineering department faculty and staff for their kindness during my many questions regarding wind tunnel testing and additive manufacturing. Furthermore, I would like to thank Stratasys Direct Manufacturing for their guidance on model production with additive manufacturing.

Finally, I would like to thank the Air Force Research Laboratory for their support of this research under CCMS Task 2.1.1.4. I would like to specifically thank Dr. Ed Alyanak for his input and guidance as the direction of this research project was progressing.

All photos by author, 2015.

# Table of Contents

# List of Figures

# List of Tables

# List of Abbreviations

| | |
|---|---|
| ABS | Acrylonitrile Butadiene Styrene |
| AFIT | Air Force Institute of Technology |
| AFRL | Air Force Research Laboratory |
| AM | Additive Manufacturing |
| AMT | All-Moving Wing Tip |
| AoA | Angle of Attack, α |
| AOE | Aerospace and Ocean Engineering |
| CCMS | Collaborative Center for Multidisciplinary Studies |
| CFD | Computational Fluid Dynamics |
| $C_L$ | Lift Coefficient |
| $C_l$ | Rolling Moment Coefficient |
| $C_m$ | Pitching Moment Coefficient |
| $C_N$ | Normal Force Coefficient |
| $C_n$ | Yawing Moment Coefficient |
| DLEF | Differential Leading Edge Flap |
| DoE | Design of Experiments |
| DRUD | Deployable Rudder |
| ETC | Easy To Change |
| FDM™ | Fused Deposition Modeling |
| FFF | Fused Filament Fabrication |
| GLS | Generalized Least Squares |
| HTC | Hard To Change |
| ICE | Innovative Control Effector |
| LCC | Life Cycle Cost |
| LEF | Leading Edge Flap |
| LHS | Latin Hypercube Sampling |
| LMTAS | Lockheed Martin Tactical Aircraft Systems |
| LSP | Lower Surface Spoiler |
| NACA | National Advisory Committee for Aeronautics |
| OFAT | One Factor At a Time |
| OLS | Ordinary Least Squares |
| PC | Polycarbonate |
| PLA | Polylactic Acid |
| RANS | Reynolds-Averaged Navier-Stokes |

| | |
|---|---|
| REML | Restricted Maximum Likelihood |
| NRMSE | Normalized Root Mean Square Error |
| RP | Rapid Prototyping |
| RSM | Response Surface Model |
| S&C | Stability and Control |
| SBO | Surrogate-Based Optimization |
| SL | Stereolithography (also abbreviated SLA) |
| SLS | Selective Laser Sintering |
| SOTA | State Of The Art |
| SP | Subplot or Split Plot |
| SSD | Spoiler-Slot-Deflector |
| STL | Standard Tessellation Language |
| TED | Trailing Edge Down |
| TEF | Trailing Edge Flap |
| VLM | Vortex Lattice Method |
| VT | Virginia Tech |
| WP | Whole Plot |
| WSU | Wright State University |
| WT | Wind Tunnel |
| $\delta$ | Flap Deflection Angle |

# 1 Introduction

The work reported in this thesis is motivated by the need to develop improved aircraft design processes that will enable more cost-effective exploration of a larger design space necessary to accommodate more demanding performance requirements of future air vehicles and to address associated affordability issues. Design processes based on the multidisciplinary design optimization (MDO) concepts hold considerable promise for meeting this need; their role is highlighted in Section 1.1. However, further research is required in many aspects of MDO-based design processes [1-3].

The Collaborative Center in Multidisciplinary Sciences (CCMS) at Virginia Tech (VT) is focused on conducting MDO related research that is most relevant to the needs of the US Air Force. The CCMS was established in 2009 under the sponsorship of the Air Force Research Laboratory (AFRL) to facilitate collaborative execution of research tasks as jointly determined by researchers at AFRL's Multidisciplinary Science & Technology Center, and the CCMS team of VT and Wright State University (WSU).

The presented research is in direct support of a CCMS task (Task 2.1.1.4) which aims to develop a process for incorporating additive manufacturing (AM) and rapid prototype (RP) testing into a high-fidelity MDO environment suitable for the conceptual design of aerospace vehicles with emphasis on designing optimal control effectors for a tailless supersonic vehicle. A lack of vertical control surfaces on tailless vehicles requires non-traditional methods for control complicating stability and control (S&C) analysis; the challenges associated with S&C of tailless vehicles is addressed in Section 1.2.

## 1.1 Role of Multidisciplinary Design Optimization in Aircraft Design

As aircraft concepts become more complex due to demand for better performance, their cost have escalated dramatically [3]. There is renewed pressure on aircraft manufacturers to produce affordable aircraft. Therefore, aircraft design methods that reduce Life Cycle Cost (LCC) are highly desired. LCC is a measure of the overall cost to design, manufacture, and maintain an aircraft. One of the notable features of LCC is how large an impact early design decisions have as shown in Figure 1.1. Even though conceptual design only contributes 20% of the overall aircraft cost, the decisions made during this stage impact up to 70% of the cumulative LCC. Therefore,

methods for improving the quality and time required of conceptual design, such as MDO, are pivotal to decreasing cost of next-generation aircraft.

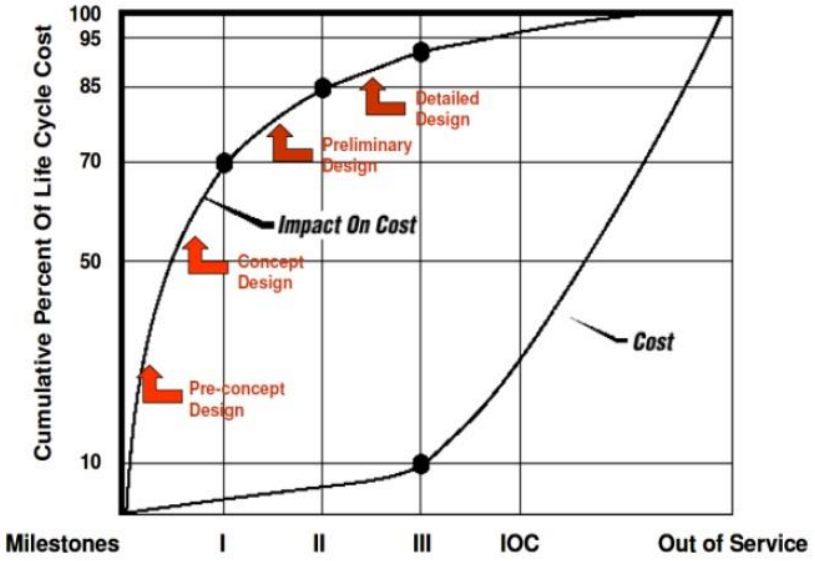


**Figure 1.1: Conceptual Design impact on LCC. Raj, P., and Friedman, A. M. "On timely and cost-effective prediction of aerodynamic data to meet aircraft design needs," presented at the RAeS Applied Aerodynamic Conference, Bristol, UK. 22-24 July 2014. Used under fair use, 2015.**

MDO based aircraft design approach is aimed at reducing the cost of designing next-generation aircraft by considering all of the disciplines of an aircraft design together and capturing key effects of multidisciplinary interactions early. An MDO framework is composed of many different tools which correspond to the various disciplines of an aircraft, such as aerodynamics, structures, propulsion, etc. For an MDO to produce a quality optimal design, the inputs to each of the tools must be of high quality.

Researchers at Virginia Tech (VT) have developed an MDO framework for aircraft design. An $n^2$ diagram of the VT MDO framework, shown in Figure 1.2, illustrates the coupling of different disciplines and their interdependencies. Detailed information on the creation of the VT MDO framework and the discipline modules are found in works by Allison [1] and Morris [2]. The module of investigation in this work, S&C, historically was not addressed in extensive detail until after the conceptual design phase. The crucial role of the S&C module in aircraft conceptual design is highlighted in the next section.

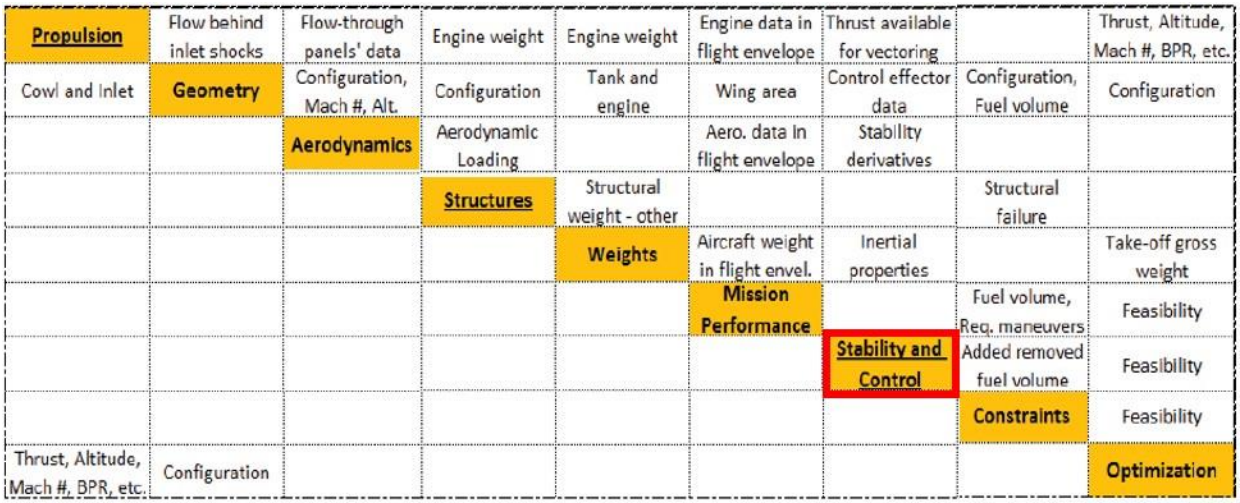


**Figure 1.2: VT MDO $n^2$ diagram. Allison, D. "Multidisciplinary Analysis and Design Optimization of an Efficient Supersonic Air Vehicle," Ph.D. Dissertation, Aerospace and Ocean Engineering Dept., Virginia Polytechnic Institute and State University, Blacksburg, Virginia, 2013. Used under fair use, 2015.**

## 1.2 Stability and Control in MDO

Typical conceptual design S&C analyses use the tail volume coefficient and look at the basic static stability of an aircraft [2]. The flight dynamics of an aircraft, even more so for a tactical, tailless aircraft, are not fully captured by static stability analysis. Therefore, analysis of the dynamic stability characteristics in conceptual design are important to understanding the flight characteristics of the aircraft. Furthermore, tailless vehicles, a focus area of the CCMS research task, complicate S&C even further. Since there are no vertical control surfaces, non-traditional methods are required for control. These non-traditional control surfaces have aerodynamic influences in multiple axes making the equations of motion for the aircraft highly-coupled. Critical flight regimes for controlling tailless aircraft are takeoff and landing due to the low speeds and high angles of attack (AoA). In these regimes, the demand for control power is much greater.

The key challenge of incorporating a S&C module into an MDO framework that determines the static and dynamic stability of conceptual designs is generating the necessary data in a timely, and cost-effective manner. The data needed for a S&C module can be generated with wind tunnel (WT) testing or computational fluid dynamics (CFD) analysis; however, neither WT testing nor CFD analysis is fully effective for use in an MDO framework as discussed in the next section.

## 1.3 Effectiveness

The suitability of WT testing or CFD analysis for data generation in a conceptual design MDO framework can be quantified by effectiveness. Effectiveness is defined by Miranda [4] as

$$Effectiveness = Quality \times Acceptance \tag{1.1}$$

Quality factors are measures of predicted data credibility, and acceptance factors are divided into timeliness and cost to deliver the data [3]. Modules within an MDO framework should have the highest effectiveness possible to come up with a best design.

### 1.3.1 Effectiveness of CFD

CFD analysis often can generate data in a short amount of time; however, quality of the data is not always assured. For a tailless military aircraft with non-traditional control surfaces, the elementary pitching moment data is difficult for even high-fidelity CFD analysis to capture.

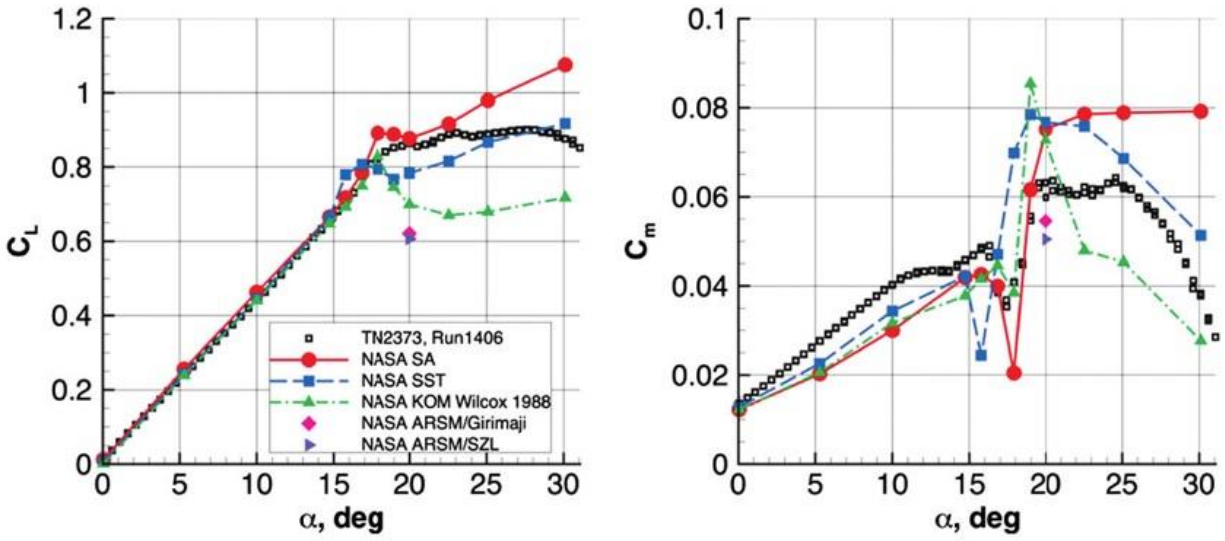


**Figure 1.3: High Fidelity CFD (RANS) and Experimental Data. Frink, N. T., Tormalm, M., and Schmidt, S. "Three Unstructured Computational Fluid Dynamics Studies on Generic Unmanned Combat Aerial Vehicle," *Journal of Aircraft* Vol. 49, No. 6, 2012, pp. 1619-1637. Used under fair use, 2015.**

Low-fidelity CFD analysis, such as the Vortex Lattice Method (VLM), for a S&C module does not have high enough quality. Even though the acceptance of the data is high, roughly 1 second/CPU for each data point, the low quality data for complex flow physics results in insufficient effectiveness. Furthermore, high-fidelity CFD analysis takes more time, roughly 2 hours/64 CPU for each data point with Reynolds-Averaged Navier-Stokes (RANS) analysis [5].

Figure 1.3, where black data points are experimental data and all other points are RANS CFD results, depicts the inability of RANS CFD to accurately capture the experimental pitching moment, thus not being a fully effective method for generating S&C data for an MDO framework [6]. Low-fidelity CFD analyses do not have the required quality due to the simplified representation of flow physics. Even high-fidelity CFD analyses also do not have the required effectiveness due to limitations of turbulence models along with larger computational cost. Research is being conducted to improve CFD analysis effectiveness for aircraft conceptual design MDO, but this is outside the scope of this work.

### 1.3.2 Effectiveness of Wind Tunnel Testing

The second tool for generating S&C data is WT testing of scale models; however, traditional methods of fabricating models and WT testing are not fully effective for an MDO environment. WT models are costly to fabricate, on the order of tens to hundreds of thousands of dollars, and take on the order of months to complete [7]. Therefore, traditional methods of producing WT models are not fully effective for use in an MDO environment. Also, traditional methods of WT testing have a rough order of magnitude cost of hundreds of thousands of dollars and can take weeks to months [8]. If the time and cost to produce and test models were reduced, then WT testing may become an effective method for S&C data generation to be used in an MDO framework. AM and RP offer considerable promise to improve the effectiveness of WT testing.

## 1.4 Research Objectives

The objectives of this work are two-fold. First, evaluate state-of-the-art (SOTA) AM and RP technologies for their effectiveness in generating WT models and acquiring quality S&C data by reducing elapsed time to hours and days rather than weeks and months of traditional WT testing, and by reducing cost to a few hundred or a few thousand dollars rather than tens and hundreds of thousands of dollars. The testing is limited to static S&C analysis in the VT Open-Jet WT (Appendix A) to date, but the exclusion of dynamic testing is not a fundamental limitation to the WT testing of AM models. Second, develop a process to incorporate quality S&C data using AM and RP technologies for control effector optimization and demonstrate feasibility of the process. Moreover, the exclusion of dynamic WT testing is not a fundamental limitation for process development.

Based on a literature review, Chapter 2 gives an overview of the current SOTA in AM, the tailless supersonic vehicle configuration, ICE 101, used in this work, and surrogate-based optimization (SBO) strategies. Next, Chapter 3 addresses WT model fabrication using AM. From current SOTA AM practices, parts are manufactured and are used for WT data acquisition. Chapter 4 addresses process development for incorporating WT data into an MDO environment. Modifications to current SBO strategies are presented. Chapters 5 and 6 detail and discuss the results of AM and process development in this research. Finally, conclusions and future work are presented in Chapter 7.

# 2 Literature Review

In order to achieve the research objectives of this work, a literature review was conducted to investigate SOTA AM technologies and SBO strategies. Section 2.1 introduces AM and applicability for WT model fabrication. Next, Section 2.2 presents representative tailless configurations with innovative control effectors. Lastly, Section 2.3 introduces the SBO strategy and the components within.

## 2.1 Additive Manufacturing

AM processes are discussed in Section 2.1.1 with emphasis on FDM™ and PolyJet. Next, Section 2.1.2 compares FDM™ and PolyJet technologies with AM metrics: operations, part characteristics, and material options. Lastly, Section 2.1.3 introduces research investigating applicability of AM to WT model production.

### 2.1.1 AM Processes

First introduced by Hideo Kodama [9] in the early 1980s, the method for creating three-dimensional plastic models from an ultraviolet cured polymer was the beginning of almost all additive manufacturing processes today. Next, came the coining of the term Stereolithography by Chuck Hull in 1984. Even though Kodama already invented the process, Hull created the file type STereoLithography (STL which now stands for Standard Tessellation Language) a common file type used by most additive manufacturing processes today. Also, Hull [10] developed methods for slicing CAD models and infill structures for printing with AM.

Present day AM encompasses a wide range of processes that span from ultraviolet curing of liquid material to deposition of molten plastic to laser sintering of metal particles. Two of the most prominent AM processes used today, and utilized in this work, are Fused Deposition Modeling (FDM™) and PolyJet printing. Pham and Gault [11] provide a categorical breakdown of AM and details on how each process creates a three-dimensional model from a CAD geometry.

FDM™ consists of heating a thermoplastic filament to 0.5°C above the melting point to make the material molten for extrusion. A thread of the molten filament is then deposited layer by layer solidifying in 0.1s and cold-welding to previous layers, depicted by Figure 2.1.

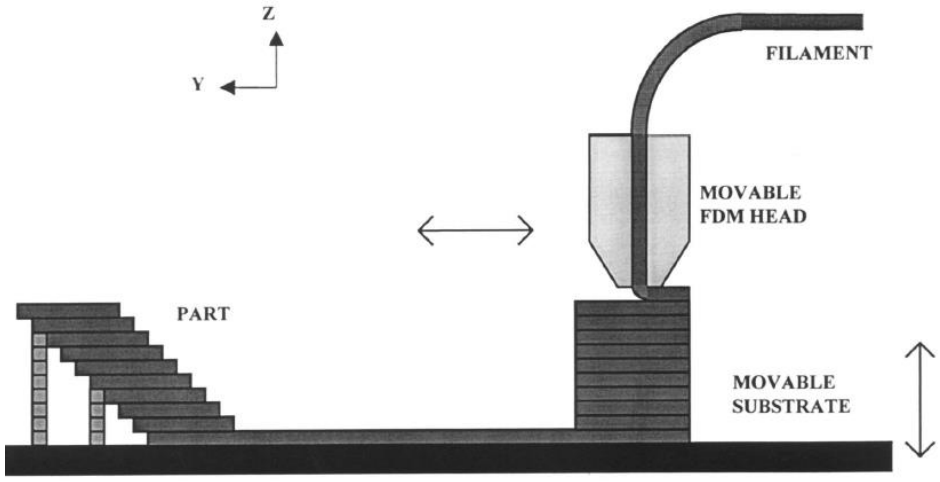


**Figure 2.1: Illustration of Fused Deposition Modeling. Pham, D. T., and Gault, R. S. "A comparison of rapid prototyping technologies," *International Journal of Machine Tools and Manufacture* Vol. 38, 1997, pp. 1257-1287. Used with permission of Elsevier, 2015.**

PolyJet printing is similar to traditional two-dimensional inkjet printing. Layers of a liquid photopolymer are deposited onto a print bed and then the polymer is cured through exposure to ultraviolet light [12]. An illustration of PolyJet printing can be seen in Figure 2.2.

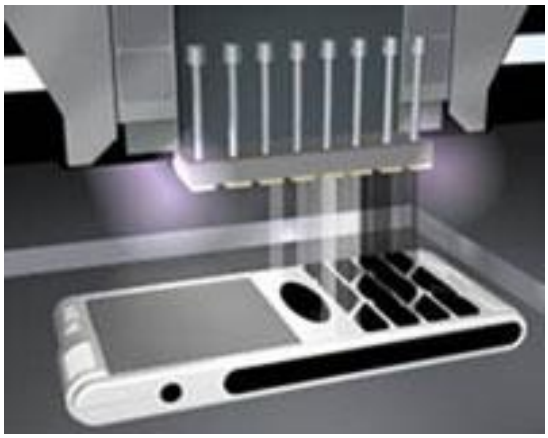

**Figure 2.2: Illustration of PolyJet printing. (14 October 2014) "How PolyJet 3D Printing Works." Stratasys Ltd., 2014. Available: http://www.stratasys.com/3d-printers/technologies/polyjet-technology. Used with permission of Ruth Jacques, Stratasys, 2015.**

### 2.1.2 FDM™ and PolyJet Comparison

FDM™ and PolyJet AM technologies can span small desktop machines to large scale factory floor machines. Therefore, these two technologies have a wide range of applications and are constantly being advanced through addition of new materials and improvement of the technology. A

comparison of the FDM™ and PolyJet processes is made in this section. Many comparative studies of the various AM processes have been completed [11, 13, 14]. After Pham and Gault [11] discuss how each of the AM processes (available in 1997) function, applications are suggested for RP, and tables are presented comparing the commercially and non-commercially available AM processes using data from manufactures or other benchmark studies. Also, a flowchart is developed for selection of processes for various applications.

Kim and Oh [13] performed benchmark tests to determine the material properties and heat resistance of AM processes and materials. Stratasys [14], whose founder invented FDM™ and who merged with Objet Geometries, the inventors of PolyJet, gives a detailed comparison of FDM™ and PolyJet. Furthermore, roughness, manufacturing speed, and material costs are compared. Since AM's inception, research has been conducted on the emerging technologies within the field and suggestions for applications have been made. As AM advances further with new processes and materials, research will continue to improve AM's suitability for rapid prototyping and low-cost, fast, part production.

AM processes are generally compared on the bases of three criteria: 1) operations, 2) part characteristics, and 3) material options. Some of the key properties within these criteria are part size, materials, resolution, print speed, support material type/removal, ease of use, pre-/post-processing, and surface finish. The operation criteria of FDM™ or PolyJet has the properties: speed, pre-/post-processing, environment conditions, ease of use, and operating expense.

#### 2.1.2.1 Operations

For AM, speed is a difficult property to measure, and making comparisons of speed is often infeasible. The speed to produce a part is highly dependent on the part geometry. FDM™ and PolyJet do have speeds at which the print heads operate, but this does not give a good measure to compare print times. Pre- and post-processing time, amount and type of support material, part size, and print resolution have a large impact on part production speed that cannot be easily generalized. Kim and Oh [13] use benchmark tests to compare the speed of AM processes by producing the same parts on each machine. However, even this does not give a general rule for which AM processes is faster because each process may handle support material differently requiring the print head to switch materials more or less frequently. Stratasys [15] gives a good explanation as to all of the variables that go into determining the speed of part production and why it is infeasible to

claim a general rule for prediction of AM speed. However, from the various benchmark tests in the above references, the production time for FDM™ and PolyJet is comparable.

One aspect of production speed that can be determined is the steps and time needed for pre- and post-processing of a part. Both FDM™ and PolyJet require limited work in pre-processing. An STL file is added to the printer software, and then the CAD model is sliced for printing and tool paths are drawn. This is all accomplished by the software of the printers with limited input from the user. One major difference in the pre-processing of FDM™ is that it allows the user to locally select the infill of a part. If certain regions of a part need more strength, then the region can be made solid, but if the rest of the model does not need the same strength, then the model can be sparse filled. When it comes to comparison of the post-processing time for FDM™ and PolyJet, the two processes are quite different. PolyJet uses a water-jet for removal of support material which requires an operator but can be quick. FDM™ can either use dissolvable support material or breakaway supports. The dissolvable support does not require an operator but does take more time to remove the support material. The breakaway supports use the same material as the model material which can cause adverse effects to the model during removal. Breakaway support removal is much faster than the dissolvable support removal, but breakaway supports may require further post-processing, such as sanding supported regions.

Some AM processes use toxic materials or lasers with small particulates that could go airborne requiring special environmental conditions to reduce safety hazards [14]. However, both FDM™ and PolyJet use non-toxic materials and do not need special environments for use. FDM™ and PolyJet just need power and a water supply for support material removal. Since no special environment is needed for FDM™ and PolyJet, the printers are easy to use; material placement requires the operator to simply exchange the old material cartridge with a new one. FDM™ does require addition of a build sheet for each build, but this is a simple addition to the print process.

Operating expenses for PolyJet tend to be higher due to the need to replace the print heads more frequently (after 2,000 hours). Even though FDM™ requires replacement of a build sheet each print, this cost is inexpensive when compared to the cost of PolyJet print head replacement. Furthermore, PolyJet tends to use more support material for each build because more is needed to restrain the photopolymer droplets. FDM™ can use less support material since the molten plastic

solidifies quickly after extrusion. Also, the cost of standard material per weight for FDM™ and PolyJet is comparable making PolyJet have a higher operating cost [14].

#### 2.1.2.2 Part Characteristics

The second criterion for comparison of FDM™ and PolyJet is part characteristics, which includes surface finish, resolution, and size. The PolyJet process is known for its ability to produce parts at high resolution with a smooth surface finish. PolyJet can even automatically create a gloss finish layer on the upper surface of a print. Moreover, PolyJet can produce layers with thicknesses down to 16 microns. FDM™ does not produce parts with resolution and surface finish comparable to PolyJet. With FDM™, the path of extrusion and the individual layers can often be seen, but these can be eliminated with extra post-processing, such as machine or hand sanding. The minimum resolution FDM™ can print is 127 microns (0.005”); although this is not as fine as PolyJet, the resulting surface finish can be made smooth by orienting the model in an optimum way for surface finish. As mentioned previously, both FDM™ and PolyJet range from small desktop to large scale manufacturing printers. On the small scale range, the smallest build volume starts at approximately 5 x 5 x 5 inches for FDM™ and approximately 9 x 8 x 6 inches for PolyJet. On the large scale range both FDM™ and PolyJet have printers with build volumes of approximately 2 x 3 x 2 feet. The range of build volumes for FDM™ and PolyJet make them suitable for a wide range of applications.

#### 2.1.2.3 Material Options

The last criterion for comparing FDM™ and PolyJet is the material options. Between the two processes there are close to six hundred different options. These materials range from engineering grade plastics to rubber like materials to heat resistant materials to bio-compatible materials. Figure 2.3 from Stratasys [14] gives a breakdown of some of the material groupings for FDM™ and PolyJet with each of their unique qualities.

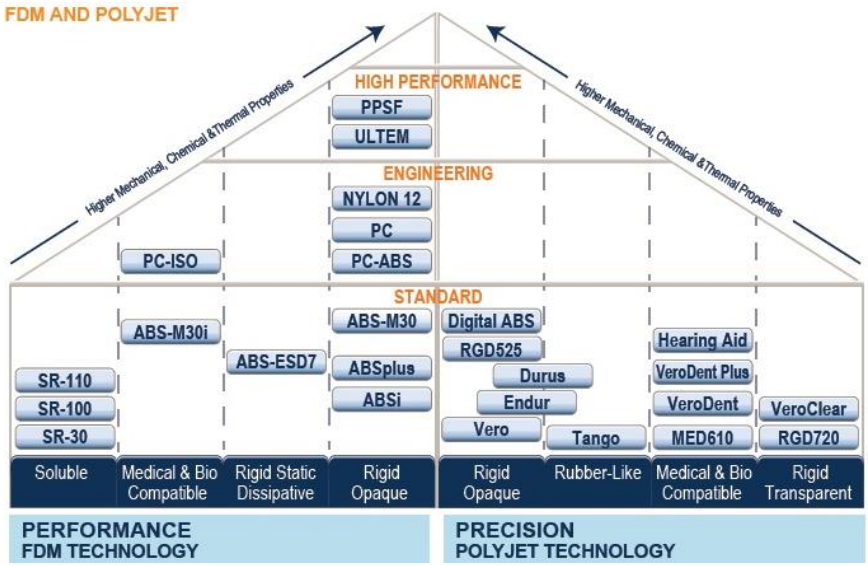


**Figure 2.3: Comparison of FDM™ and PolyJet materials with divisions based on properties and applications. (July 10, 2014) Fischer, F. "FDM and PolyJet 3d Printing: Determining which technology is right for your application." Stratasys Ltd., 2014. Available: http://www.stratasys.com/~/media/Main/Files/White%20Papers/SSYS-WP-SSYS-InkjetComparison-07-13.pdf. Used with permission of Ruth Jacques, Stratasys, 2015.**

Finally, Stratasys provides a table of the criteria described above for direct comparison of FDM™ and PolyJet for selecting a process for an application. Table 2.1 should not be used as the only resource for selecting between FDM™ and PolyJet; however, it does provide a good guide as to the strengths and weaknesses of each process.

| | PolyJet 3D Printing | Fused Deposition Modeling (FDM) |
|---|---|---|
| **Operations** | | |
| Process Time | ●●● | ●●◖ |
| Pre-process | ●● | ●●● |
| Post-process | ●●● | ●●● |
| Office Environment | ●●● | ●●● |
| Ease of Use | ●●● | ●●● |
| **Characteristics** | | |
| Surface Finish | ●●● | ● |
| Feature Detail | ●●● | ● |
| Accuracy | ●● | ●●● |
| Size | ●●● | ●●● |
| **Materials** | | |
| Rigid | ●●● | ●●● |
| Flexible | ●●● | ◖ |
| Durable | ●◖ | ●●● |
| Transparent | ●●● | ● |
| High-performance | ● | ●●● |
| Bio-compatible | ●●● | ●●● |

**Table 2.1: Comparison of FDM™ and PolyJet for various selection criteria. (July 10, 2014) Fischer, F. "FDM and PolyJet 3d Printing: Determining which technology is right for your application." Stratasys Ltd., 2014. Available: http://www.stratasys.com/~/media/Main/Files/White%20Papers/SSYS-WP-SSYS-InkjetComparison-07-13.pdf. Used with permission of Ruth Jacques, Statasys, 2015.**

### 2.1.3 Applicability of AM to Wind Tunnel Models

Since the inception of AM there have been many studies on producing WT models with AM [16-31]. Almost all of these studies have employed the use of a metal strongback for added model strength. However, an AFRL study [23-27] with a Striker Tanker configuration, Figure 2.4, used Selective Laser Sintering (SLS) to create a wind tunnel model out of steel.

**Figure 2.4: AFRL Striker Tanker SLS model at AFIT low-speed wind tunnel (left) and UCAV X45-A SL at AFRL Subsonic Aerodynamic Research Laboratory (SARL) (right). Tyler, C., Braisted, W., and Higgins, J. "Evaluation of Rapid Prototyping Technologies for Use in Wind Tunnel Model Fabrication," presented at the 43rd AIAA Aerospace Sciences Meeting and Exhibit, Reno, NV. January 10-13, 2005. AIAA-2005-1301. Used under fair use, 2015.**

As the name suggests, SLS uses a laser to fuse, or sinter, particles to form a model. SLS can create models out of plastic or metal. An advantage of using SLS and steel is the ability to post-process the model with traditional manufacturing practices, such as tapping holes. Also, CFD was used in the AFRL study to determine the wing loads that the model would experience in the Air Force Institute of Technology (AFIT) low-speed WT. The criteria Tyler *et al* [26] used to evaluate the model included the ability to not deform under load, the ability to incorporate pressure taps for flow field measurements, and the cost/time required to produce the model. The study of creating pressure tap tubes with AM was done on the UCAV X-45A configuration shown in right image of Figure 2.4. This model was produced using Stereolithography (SL) since it is water-tight, a necessity for pressure taps, with a metal strengthening plate. AFRL determined that the diameter of each hole should be 0.035 inches with a minimum bend radius of 0.05 inches near the pressure tap location, and a bend radius of at least 0.125 inches throughout the rest of the model.

Another study performed by Springer *et al* [19-21] compared several wing-body launch vehicle models constructed with FDM™, SL, and SLS to a traditionally manufactured metal model, shown in Figure 2.5. The focus of the work was to determine if using AM to produce WT models could reduce the cost and time required for providing WT data earlier in the design process.

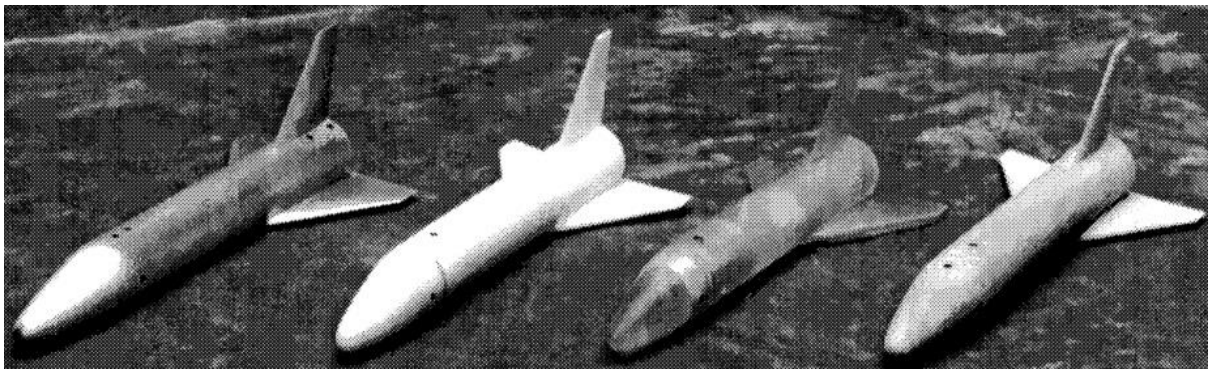

**Figure 2.5: Launch vehicle models: Aluminum, FDM™, SL, SLS (from left to right). Springer, A., and Cooper, K. "Comparing the Aerodynamic Characteristics of Wind Tunnel Models Produced by Rapid Prototyping and Conventional Methods," presented at the 15th Applied Aerodynamics Conference, Atlanta, GA. 1997. AIAA-97-2222. Used under fair use, 2015.**

At the time of the study in 1997, the materials for AM were not as mature as they are today; so the conclusions drawn were that the cost and time savings were significant for producing WT models, but there are issues and concerns with model strength. Using the same vehicle configuration as Springer *et al*, Ahmadi *et al* [22] produced three models of varying layer resolution. The purpose of this study was to determine the effect of surface finish (layer resolution) on aerodynamic data. Ahmadi *et al* found in general that the different models only varied by about 5% in longitudinal aerodynamic data. The testing performed was throughout the subsonic and transonic regimes. As the surface roughness increased, the model cost and time of production decreased while still maintaining acceptable accuracy in aerodynamic data making the low surface roughness acceptable for preliminary design data generation.

Zhu *et al* [28] from the State Key Laboratory of Manufacturing Systems Engineering and Kroll *et al* [30, 31] from the Technion Institute of Technology, both looked at production of fully configured WT models with exchangeable control surfaces. Zhu used CFD to determine the loads on an SL manufactured model with a metal core, which would be used for comparison to an all metal model of traditional manufacturing process. Also, leading edge flaps (LEF), trailing edge flaps (TEF), and the rudder were produced with SL with the focus on how to fix the control surfaces to the model since AM models (except metal SLS models) are not suitable for tapping screw holes. Kroll implemented the use of AM WT models to enhance aerospace engineering students' learning. The models in this study were produced with PolyJet and due to printer volume

limitations, the models used metal plates for joining several pieces together. The metal plates were also used for mounting the control surfaces to the model.

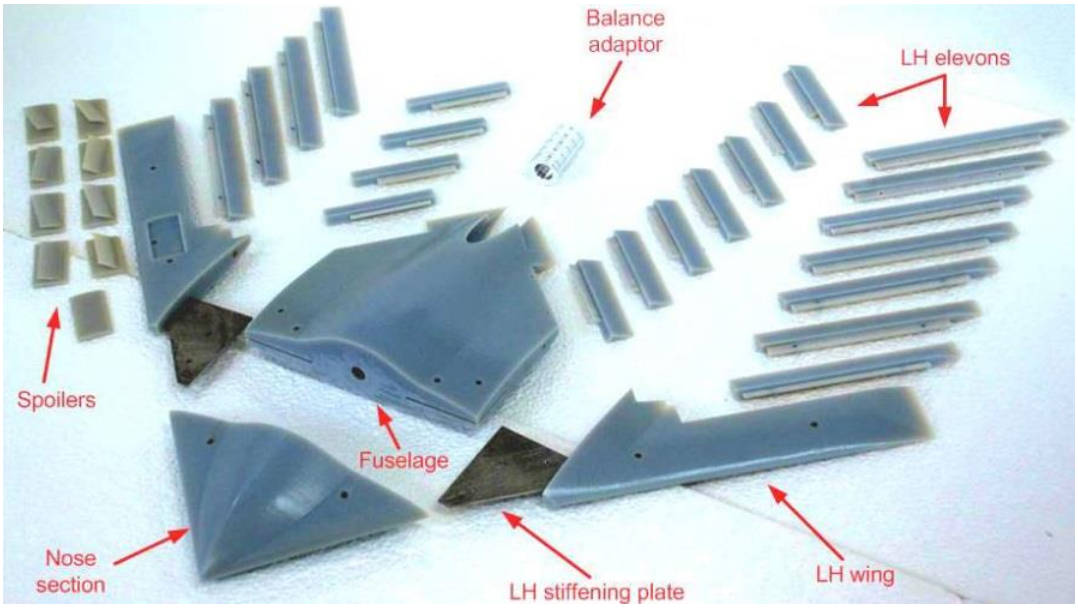


**Figure 2.6: Technion produced CERBERUS model with control surfaces using PolyJet printing. Kroll, E., and Artzi, D. "Enhancing aerospace engineering students' learning with 3D printing wind-tunnel models," *Rapid Prototyping Journal* Vol. 17, No. 5, 2011, pp. 393-402. Used under fair use, 2015.**

Kroll was able to produce small control surfaces with thicknesses of less than 0.6 mm. Figure 2.6 shows one of the configurations produced, CERBERUS, with all of the exchangeable control surfaces. Although there were the structural and durability challenges, the model was used to acquire aerodynamic WT data that compared will with Tornado, a VLM software, data, and was produced at a lower cost and time than a traditionally manufactured WT model.

## 2.2 Tailless Aircraft Configurations & Innovative Control Effectors

As noted in Section 1.2, tailless aircraft configurations with innovative control effectors are the focus of this work due to complexity of S&C data generation for such a geometry. Section 2.2.1 presents the representative tailless configurations investigated for use this work, Stability and Control Configuration (SACCON) and Innovative Control Effector (ICE) 101. Furthermore, Section 2.2.2 introduces several innovative control effectors accompanying the ICE 101 configuration.

### 2.2.1 ICE 101 Configuration

First, SACCON from Cummings *et al* [32-35], Frink *et al* [6], Loeser *et al* [36], Tomac *et al* [37], and Vicroy *et al* [38], was investigated for use as a representative tailless vehicle configuration.

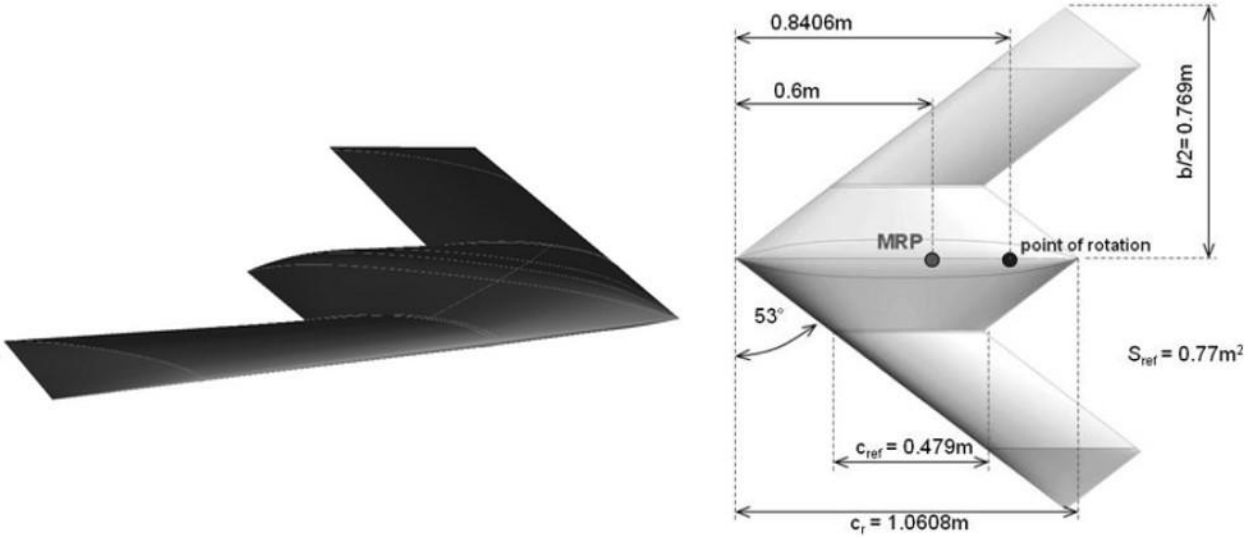


**Figure 2.7: SACCON configuration. Vicroy, D. D., Loeser, T. D., and Schutte, A. "SACCON Forced Oscillation Tests at DNW-NWB and NASA Langley 14x22-Foot Tunnel," presented at the 28th AIAA Applied Aerodynamics Conference, Chicago, IL. June 28 - July 1, 2010. Used under fair use, 2015.**

However, at the start of this work, the SACCON configuration did not have any control surfaces, and the CAD geometry was not open for public release, which prompted the search for a different representative tailless configuration. The next configuration considered is the ICE 101 configuration sponsored by Wright Laboratory and the Naval Air Warfare Center Aircraft Division. Research on the ICE 101 configuration was also conducted by Dorsett [39] and Dorsett *et al* [40, 41] from Lockheed Martin Tactical Aircraft Systems (LMTAS). The ICE 101 configuration was developed to determine the control effectiveness of several novel control effectors as discussed in the next section. ICE 101, shown in Figure 2.8, is a delta wing configuration with a leading edge sweep angle of 65° and a full suite of control effectors. The chord and span of the full scale ICE 101 are 43.1 ft and 37.5 ft, respectively, resulting in an aspect ratio of 1.74. The wind tunnel models of ICE 101 had faired over inlets and nozzle.

Phase I [40] of the ICE 101 study focused on evaluation of the innovative control concepts for a highly-maneuverable fighter aircraft without vertical control surfaces. The innovative control concepts are compared to conventional control concepts for ability to provide needed lateral-

directional control power. The top three concepts were selected for further evaluation in Phase II [41] of the research. Moreover, Phase II focused on expanding the experimental database for ICE 101 and the selected innovative control effectors. Also, flying qualities constraints were evaluated with the selected innovative control effectors.

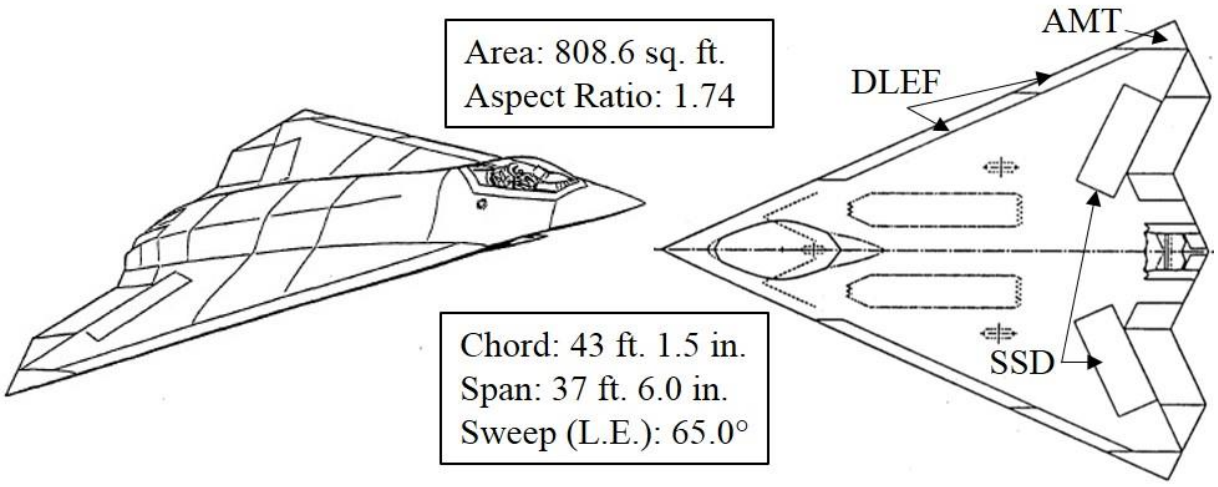


**Figure 2.8: Innovative Control Effector (ICE) 101 configuration with the top three control effector concepts. Dorsett, K. M., and Mehl, D. R., AFRL, "Innovative Control Effectors (ICE)." LMTAS. 1996. Report Number: WL-TR-96-3043. Used under fair use, 2015.**

### 2.2.2 Innovative Control Effectors

There were five innovative control effectors on the ICE 101 configuration, and three of the five were selected based on control performance compared to conventional control effectors. The five original innovative control effectors are all-moving wing tip (AMT), spoiler-slot-deflector (SSD), differential leading edge flaps (DLEF), deployable rudder (DRUD), and lower surface spoiler (LSP). The three control concepts selected for further research were the AMT, SSD, and DLEF.

The AMT was found to have the highest control authority of the three selected control effectors and was found to be comparable to conventional control effectors such as spoilers, clamshell ailerons, etc. For ICE 101, small, skewed, and large AMTs were tested to determine what aspect of the AMT results in the greatest control authority. In Figure 2.9, the movement of the AMT can be seen. The AMT rotates about the span-wise direction; however, this is not the case for the skewed AMT. Asymmetric deflection of the AMTs results in the ability to generate large roll and yaw moments. An advantage of the AMT over clamshell ailerons is the ability to generate yawing moments through high AoA.

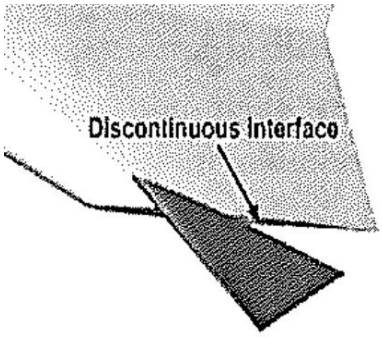


**Figure 2.9: ICE 101 deflected AMT. Dorsett, K. M., Fears, S. P., and Houlden, H. P., AFRL, "Innovative Control Effectors (ICE) Phase II." LMTAS. 1997. Report Number: WL-TR-97-3059. Used under fair use, 2015.**

The SSD has been under investigation from the 1950s for use as a novel control effector [42-44]. Both a spoiler and a slot are combined so the flow can move through the wing. This allows high pressure air from the lower surface to flow through to the upper surface energizing the flow. Although SSDs introduce structural issues with the wing box and skin, the performance at high AoA is favorable. Also, the performance is more linear when compared to a traditional spoiler. Furthermore, the SSD is effective though a wide range of angles and flow speeds.

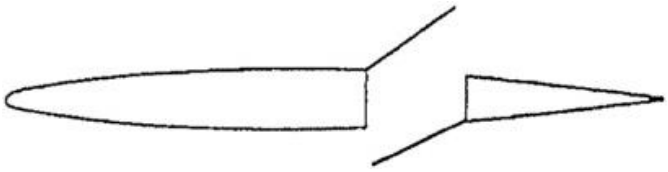

**Figure 2.10: 2D depiction of a SSD. Brown, A. E., and Hammond, A. D., NACA, "Results of an investigation at high subsonic speeds to determine lateral-control and hinge-moment characteristics of a spoiler-slot-deflector configuration on a 35 degree sweptback wing." Langley Aeronautical Lab, VA. 1957. Report Number: NACA RM L57C20. Used under fair use, 2015.**

Finally, the DLEF is found to provide needed yaw control moments at AoAs higher than fifteen degrees. This is accomplished through the restructuring of vortices on top of a highly swept, sharp leading edge wing. DLEF have many disadvantages, such as poor performance due to other neighboring control effectors and in sideslip [40].

## 2.3 Surrogate-Based Optimization

Design of an optimal control surface configurations can be performed using SOTA MDO processes and high-fidelity CFD analysis. A multidimensional design space can be simulated thousands of times for design optimization. However, with high-fidelity CFD analysis, each

simulation may take 4-5 hours on 4 cores to complete, creating an ineffective process for design optimization. For example, AoA sweeps may be performed for varying flap deflection angles, sizes, positions, and orientations. Without some design space filling strategy, discussed in the next section, generating the required data will have a large computational expense on the order of weeks or months. So when high-fidelity data is used for a design optimization process, a SBO strategy is commonly employed due to time and cost constraints.

SBO is a strategy for generating data to populate a design space with a model. The module is called a surrogate because the design space is not fully populated. Curve fitting techniques are applied a limited number of points in a design space to represent the space with a surface, or model [45]. Figure 2.11 shows the steps in an SBO strategy using CFD analysis for data generation. A space filling strategy known as Design of Experiments (DoE) is used for populating the design space with points to simulate. DoE is based on statistical analysis, specifically analysis of variance (ANOVA). Next, a response surface model (RSM) is generated from the data and then the surface is checked for adequacy and search for an optimum. Throughout this work the term "design" has two connotations. One connotation is the aircraft design to be optimized, and the second connotation is the experimental design for CFD analysis or WT testing generated from DoE. Section 2.3.1 contains a review of DoE strategies as well as reasons to perform WT testing with DoE. Section 2.3.2 reviews RSM generation techniques for a specific class of DoE, split-plot designs.

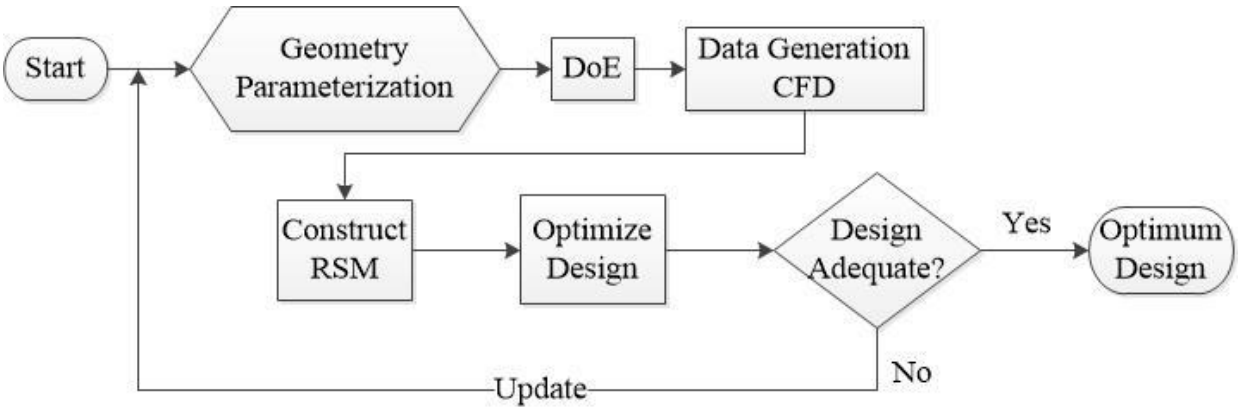


**Figure 2.11: Surrogate-based optimization strategy using CFD. Schematic developed by author, 2015.**

### 2.3.1 Design of Experiments

This section will focus on the experimental design that is implemented in this work, which is known as a split-plot design. Although, there are many resources available which give a background to DoE and methods for selecting designs for particular applications, the works of Montgomery [46, 47], were found to be particularly helpful for this research.

#### 2.3.1.1 OFAT v. DoE

As introduced in Section 1.4, the objectives of this work focus on utilizing AM and WT testing for timely, cost effective aircraft design optimization. The SBO schematic above will be modified to include data generation from WT testing; therefore, this section and subsequent sections will address the processes within the SBO schematic for use with WT testing.

Before addressing the experimental design used in this work, reasons for using DoE in WT testing applications are discussed. Traditional WT testing uses a process called one factor at a time (OFAT) testing. In this process, a sweep of AoA or sideslip is performed for each parameter change. For example, if an aircraft has a spoiler control surface with five different deflection angles, the OFAT procedure would perform a sweep of angle of attack at each deflection angle. For an MDO application such as this work, the OFAT procedure is impractical. For example, an aircraft MDO presented by Allison [1] has 26 different parameters to vary. OFAT would require $5^{26}$ or more than $1.5 \times 10^{18}$ data points if each parameter has five levels. Equation 3.1 below gives the precise number of data points that would be required.

$$5^{26} = 1,490,116,119,384,765,625 \tag{2.1}$$

If somehow it was possible to test one billion design points in a day, capturing the design space above with OFAT would still require over 4,000 millennia of constant testing! This extreme example illustrates the impracticality of using OFAT WT testing for a MDO. Since OFAT testing is not able to fully capture the design space, DoE is needed to populate a design space in a timely manner. DeLoach *et al* [48-55] present more arguments as to why DoE should be used for WT testing, such as how OFAT testing can only capture 1% of a design space with a limited budget and time constraint. Furthermore, methods for selection and analysis of DoE for WT testing are presented.

2.3.1.2 Split-Plot Designs

Split-plot designs were first developed in 1925 by Fisher for agricultural experiments. The general premise for a split-plot design is that an experiment has factors that are hard-to-change (HTC), otherwise known as whole plot (WP) factors, and easy-to-change (ETC), otherwise known as subplot (SP) factors. A typical experimental design for generating a response surface has all factors varied randomly and simultaneously; therefore, each factor changes with each design point. However, some applications, such as WT testing, required detailed, extensive procedures for changing a factor, which results in a time consuming experimental design when HTC factors change with each testing point. A major difference of split-plot designs and other experimental designs is total randomization. In a split-plot design, WP factors are randomized, and then within each WP, SP factors are randomized. The two-level randomization enables testing of a sequence of ETC factors for an individual HTC factor value before switching to another HTC factor value. The randomized structure of a split-plot design decreases the number of times HTC factors must be changed, but statistical analysis becomes more challenging as a result. A split-plot design problem from the origins of the experimental design technique is given below for a better understanding of the split-plot structure.

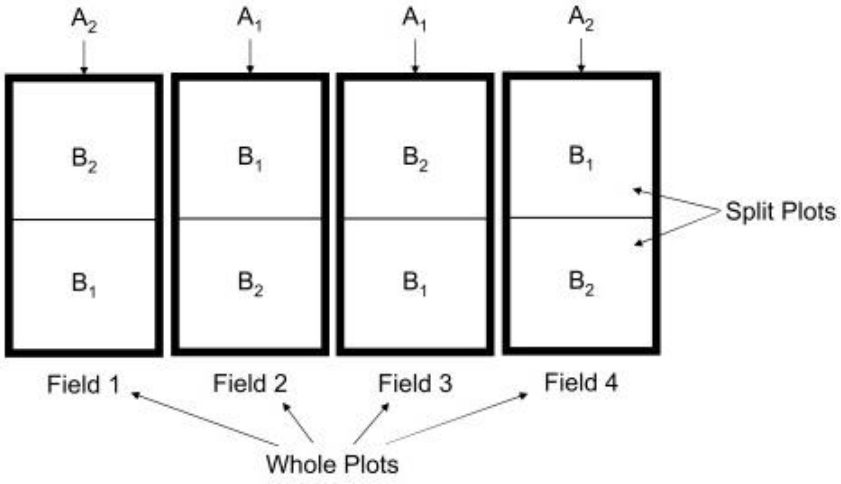


**Figure 2.12: Agricultural origins of split-plot designs, where As (WP) are irrigation methods and Bs (SP) are fertilizers. Jones, B., and Nachtsheim, C. "Split-Plot Designs: What, Why, and How," *Journal of Quality Technology* Vol. 41, No. 4, 2009, pp. 340 - 361. Used under fair use, 2015.**

In the case of the original agricultural experiment, HTC factors are irrigation methods (A) and ETC factors are fertilizers (B). Figure 2.12 shows how only one irrigation method can be applied to an entire field, or plot, and once the irrigation is in place, it is indeed difficult to change. Also,

more than one fertilizer can be applied to each plot and it is easy to change, thus making it a subplot factor. A split-plot design in this example, first randomizes the irrigation methods per field and then the fertilizers in each field are randomized [56]. The impact of two-level randomization on RSM generation will be introduced in the next section.

Split-plot designs are suitable for WT applications due to the difficulty of changing parts on a model. Mechanically actuated parts can reduce the need to replace control surfaces for each design point, which would change a control surface from a HTC factor to an ETC factor. However, mechanically actuated control surfaces increase complexity and cost of a model. If a model with replaceable control effectors at varying angles is to be tested in a WT, the tunnel must shut down between each change of control surface deflection. Along with shutting down the tunnel, the force balance will need to be recalibrated before more data can be acquired. For larger tunnels, this requires many safety procedures and calibrations which can take several hours to complete. A split-plot design for WT testing reduces the number of times that a HTC factor must be changed by testing multiple ETC factors per each WP. Further information on development and analysis of split-plot designs can be found in works by Montgomery [46], Goos *et al* [57, 58], English *et al* [59], and Parker *et al* [60, 61].

### 2.3.2 Split-Plot Response Surface Methods

A RSM is a mathematical surface that graphically represents the relationship between independent variables and a response variable. RSMs are common in industrial experiments for showing how input variables affect a performance measure or quality of a product or process. Furthermore, many industrial applications seek to optimize a product or process by searching a response surface for a minimum or maximum. Myers *et al* [62] introduces response surface methodology and provides explanations of the methods for building models for different DoEs.

As noted in the previous section, the split-plot experimental design employs two-level randomization, not a complete randomization of all factors in a design space. Certain factors are randomized at the WP level and then SP factors are randomized within each WP. This two-level randomization changes the regression equation for a RSM by introducing two error terms, one for WPs and one for SPs. The RSM regression equation for a split-plot model, $y_{ij}$, is given as

$$y_{ij}=\mu+\tau_i+\varepsilon_{WP}+\beta_j+(\tau\beta)_{ij}+\varepsilon_{SP}, \tag{2.2}$$

where $\mu$ is the overall mean, $\tau_i$ is the WP factor, $\varepsilon_{WP}$ is the WP error, $\beta_j$ is the SP factor, $(\tau\beta)_{ij}$ is the WP-SP interaction effect, and $\varepsilon_{SP}$ is the SP error. Equation 2.2 is a linear model with first order interaction effects. The two error terms require that the regression equation be solved using Generalized Least Squares (GLS) instead of the normal method of Ordinary Least Squares (OLS). Moreover, the two error terms can be determined through estimation of the error variance using the restricted maximum likelihood (REML) approach. Detailed explanations of solving split-plot RSM equations with GLS and REML can be found in: [46, 56, 57, 59, 60, 62-68]. However, for this work SAS JMP® Pro statistical software [47, 69] was used for creation of split-plot RSMs.

Since a RSM is constructed for the design space in an SBO strategy, searching for a maximum or minimum with optimization is computationally inexpensive. Therefore, optimization methods should be selected for their applicability to an RSM. Optimization methods such as gradient-based or genetic algorithms have been used for MDO applications in the past [1]. A genetic algorithm may be more suitable for an aircraft design MDO due to complex RSMs; however, a gradient-based optimization method is applied in this work for process development due to the simplicity of the method and the low-order design spaces being explored. Determining the best optimization technique for an application is an area of research that is beyond the scope of this work, but the following resources could be referenced for information on this topic [70-74].

# 3 AM Wind Tunnel Model Fabrication

This chapter focuses on the fabrication of AM parts and models selected to achieve the goals of this research. Section 3.1 introduces the various AM machines available for production of models in the Virginia Tech (VT) Aerospace and Ocean Engineering (AOE) department. Initial models, in Section 3.2, were created to determine AM's capability of producing innovative control effectors and to prepare the ICE 101 model for WT strut balance mounting. The ICE 101 1/45$^{th}$ scale model, in Section 3.3, was created for WT testing in the VT Open-Jet WT, introduced in Appendix B, for comparison to experimental data from Dorsett [39]. The NACA 0012 model, in Section 0, was selected for demonstration of the WT SBO strategy. Next, small spoiler control surfaces and a delta wing, in Section 3.5, were made to show how a WT SBO strategy would be performed for a full optimization of a control surface. Finally, plans for an ICE 101 1/15$^{th}$ scale model, in Section 3.6, were created for the VT Stability WT and issues requiring further research were identified.

## 3.1 VT AOE 3D Print Lab AM Machines

The VT AOE department 3D Print Lab houses nine AM machines with two different AM technologies, FDM™ and PolyJet, which were discussed in Section 2.1. The 3D Print Lab has 4 MakerBot Replicator 2 printers, 2 Objet30 Pro printers, 1 uPrint SE Plus printer, 1 Fortus 400mc, and 1 Objet500 Connex3 printer. The specifications for each of these printers is summarized below.

### 3.1.1 FFF: MakerBot Replicator 2 Specifications

The MakerBot Replicator 2 is a Fused Filament Fabrication (FFF[1]) type printer that uses polylactic acid (PLA) filament for printing with print volume of 11.2 x 6.0 x 6.1 inches and is capable of printing layers with thickness of 100 microns. The Replicator 2 is a single extruder printer which means that support structures are made with the same material as the model material and requires forced separation of the support material from the model during post-processing [75]. PLA has a

[1] FFF is the same process as Fused Deposition Modeling, but Stratasys has trademarked the term FDM™ so AM machines not produced by Stratasys using Fused Deposition Modeling cannot be referred to in this way.

density of 1.25 g/cm$^3$, an ultimate tensile strength of 50 MPa, and an elastic modulus of 3.5 GPa [76]. For comparison, 6061 aluminum has a density of 2.7 g/cm$^3$, an ultimate tensile strength of 124 MPa, and an elastic modulus of 68.9 GPa [77].

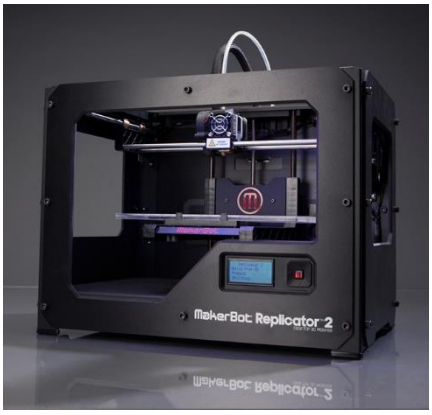


**Figure 3.1: MakerBot Replicator 2. (March 17, 2015) MakerBot. "MakerBot Replicator 2: Specifications." Available: http://downloads.makerbot.com/replicator2/MakerBot_Replicator2_brochure.pdf. Used with permission of MakerBot, 2015.**

### 3.1.2 FDM™: uPrint SE Plus and Fortus 400mc Specifications

The uPrint SE Plus is an FDM™ printer with a print volume of 8 x 8 x 6 inches and layer thicknesses down to 254 microns. The uPrint SE Plus uses acrylonitrile butadiene styrene *plus* (ABS*plus*™) filament due to the heated platform and environment of the printer. The support material for the uPrint SE Plus is soluble and can be removed through soaking the part in a heated chemical and water mixture during post-processing [78]. The density of ABS*plus*™ is 1.04 g/cm$^3$, the tensile strength is 33 MPa, and the elastic modulus is 2.2 GPa [79].

The Fortus 400mc is an FDM™ printer with a print volume of 16 x 14 x 16 inches and layer thicknesses down to 137 microns. The Fortus 400mc supports 11 different thermoplastics; some of the more common plastics used are ABS-M30 (the standard for the Fortus series), FDM™ Nylon 12 (for maximum toughness), polycarbonate (PC) (for mechanical properties and heat resistance), ABS-M30i (for biocompatibility), and ULTEM 9085 (for high strength-to-weight ratio). As with the uPrint SE Plus, the support material for the Fortus series is soluble during post-processing. ABS-M30 has a density of 1.04 g/cm$^3$, a tensile strength of 32 MPa, and an elastic

modulus of 2.23 GPa. More information on the other materials that the Fortus 400mc printer supports can be found on the Stratasys website [80, 81].

**Figure 3.2: uPrint SE Plus (left) and the Fortus 400mc (right). (March 17, 2015) Stratasys Ltd., "uPrint SE Plus Specifications." Available: http://www.stratasys.com/3d-printers/idea-series/uprint-se-plus. (March 17, 2015) Stratasys Ltd., "Fortus 360mc and 400mc Product Specs." Available: http://www.stratasys.com/3d-printers/production-series/fortus-360-400mc. Used with permission of Ruth Jacques, Stratasys, 2015.**

### 3.1.3 PolyJet: Objet30 Pro and Objet500 Connex3 Specifications

The Objet30 Pro is a PolyJet printer with a print volume of 11.57 x 7.55 x 5.85 inches and layer thickness down to 16 microns. The Pro edition supports the use of eight UV curable photopolymers (including the support material). The support material used is gel-like and can be removed using a water-jet during post-processing [82]. VeroWhitePlus, a standard material for the Objet30, has a density of 1.175 g/cm$^3$, a tensile strength of 58 MPa, and an elastic modulus of 2.5 GPa [83].

The Objet500 Connex3 is a multi-material PolyJet printer with a print volume of 19.3 x 15.4 x 7.9 inches and layer thicknesses down to 16 microns. As with the Objet30 Pro, the Connex3 uses a gel-like support material that is washed away with a water-jet during post-processing. Also, the Connex3 is capable of printing three different materials all in one part. A few of the material capabilities of the Connex3 are medical grade materials, high temperature materials, digital ABS, and rubber-like materials. The triple-jetting capability of the Connex3 enables a part to have rigid sections and flexible, rubber-like sections that are fused together. The Vero materials that are used with the Objet30 Pro are also used in the Connex3, but with more access to color palettes. More

information on the material properties of all the materials the Connex3 supports can be found on the Stratasys website [84].


**Figure 3.3: Objet30 Pro and Objet500 Connex3. (March 17, 2015) Stratasys Ltd., "Objet30 Pro Specifications." Available: http://www.stratasys.com/3d-printers/design-series/objet30-pro. (March 17, 2015) Stratasys Ltd., "Connex3 Systems Specifications." Available: http://www.stratasys.com/3d-printers/production-series/connex3-systems. Used with permission of Ruth Jacques, Stratasys, 2015.**

Table 3.1 summarizes the AM properties and machines within the VT AOE 3D Print Lab which are utilized in this work. Note that the AM machines are not limited to the materials listed in this table. Figure 2.3 provides a more detailed summary of the different materials for FDM™ and PolyJet for potential applications. Minimum layer thicknesses are important when selecting an AM process and machine for a specific application. Not only does the minimum layer thickness have an impact on surface roughness, but also impacts how thin parts can be manufactured, which is discussed further in Section 3.6. The following sections introduce the different models created and the AM machine used for each model.

| AM Machine | AM Type | Primary Material(s) | Size (in.) | Min. Layer Thickness (in.) |
|---|---|---|---|---|
| MakerBot Replicator 2 | FFF | PLA | 11.2 x 6.0 x 6.1 | 0.004 |
| uPrint SE Plus | FDM™ | ABS or PLA, soluble support | 8 x 8 x 6 | 0.01 |
| Fortus 400mc | FDM™ | ABS or PLA, soluble support | 16 x 14 x 16 | 0.005 |
| Objet30 Pro | PolyJet | Liquid Photopolymers, gel-like support | 11.6 x 7.6 x 5.9 | 0.0006 |
| Objet500 Connex3 | PolyJet | Liquid Photopolymers, gel-like support | 19.3 x 15.4 x 7.9 | 0.0006 |

**Table 3.1: Summary of the AM properties and machines in the VT AOE 3D Print Lab.**

## 3.2 ICE 101 1/27$^{th}$ Scale AMT and Mounting Block

The first prints of this work were completed on an Objet30 Pro machine since the other machines within the VT AOE 3D Print Lab were not in operation yet. Both the ICE 101 1/27$^{th}$ scale AMT and mounting block were printed with VeroWhitePlus material. The objectives of these prints were to investigate how well the PolyJet process could handle a slender, sharp-edge part like the AMT, to test the connection of the AMT to the main body, and to test the connection of ICE 101 to the strut balance to be used for WT testing. For the ICE 101 1/27$^{th}$ scale AMT pieces, a rectangular shaft was used to fix the AMT to the main body section. Then a countersunk screw was place on the main body connection to a hex nut on the underside of the main body, as seen in Figure 3.4c. The assembled AMT and main body section are shown in Figure 3.4b, with the AMT at a 30° deflection angle (+TED). The AMT part, shown in Figure 3.4, has a chord of approximately 5.5 inches and a span of approximately 2 inches.

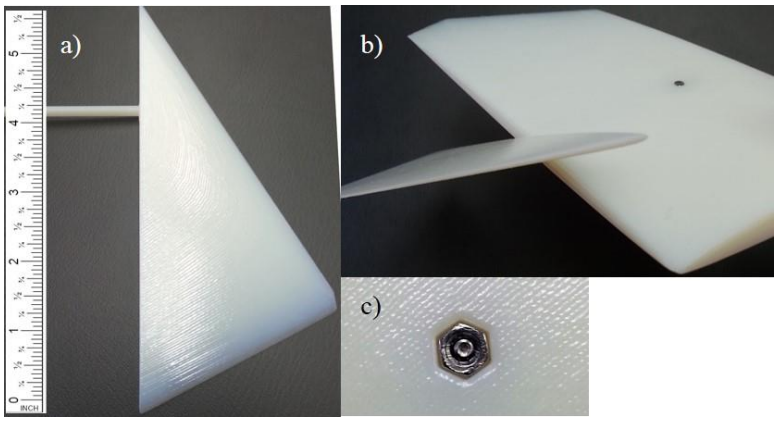


**Figure 3.4: ICE 101 1/27th Scale AMT; a) AMT at 30° with rectangular shaft, b) Assembly of AMT and main body section, c) Hex nut connection.**

Figure 3.5 shows a section of ICE 101 also at 1/27$^{th}$ scale. This print was to determine tolerances for the Objet30 Pro PolyJet machines in the lab. Since tolerances for AM are highly dependent on the calibration and accuracy of the machine, tolerances for close fitting parts are not universal. Also, the body section shown tests the connection of the ICE 101 AM model to the strut balance attachment. More information on the Open-Jet WT and instrumentation is provided in Appendix B. Moreover, the cover piece is attached in a similar manner as described in Figure 3.4, where a hex nut fits within a hexagon shaped hole for a countersunk screw to attach. Also, due to inconsistencies in the width of the strut balance mount, some of the model needed to be sanded to allow for connection of the model to the balance mount.

**Figure 3.5: ICE 101 1/27th scale strut balance mount.**

## 3.3 ICE 101 1/45$^{th}$ Scale Model

Next, a 1/45$^{th}$ scale ICE 101 model, CAD model courtesy of Bill Blake [85] with corrections to the model for AM made by another graduate student in the research group, was printed on the Objet500 Connex3 printer. The material used is of the same Vero family used for the 1/27$^{th}$ scale AMT parts. Also, this model has the same mounting configuration as in Figure 3.5. The 1/45$^{th}$ scale ICE 101 model has a chord of approximately 11.5 inches and a span of approximately 10 inches. For more accurate comparison to the experimental data from Dorsett [39], the ICE 101 model used in this work has fared over inlets. The exact fairing configuration of the original model is unknown, so attempts were made to create a smooth fairing transition. The model was printed in a horizontal configuration and a gloss finish was applied to the upper surface of the model by the Connex3 printer. Removal of the support material was completed using a water-jet; however, during this process, the thin wing tips chipped, which can be seen in Figure 3.6a. Wing tip

thickness issues reoccur and are addressed in Section 3.6. Figure 3.6b shows the countersunk screw holes used to attach the model to the balance mount. Prior to manufacturing of the 1/45$^{th}$ scale model, stress analysis was performed using low-fidelity CFD analysis for approximate load determination. The loads were then applied to the CAD geometry to ensure the AM material could withstand loads in the Open-Jet WT.

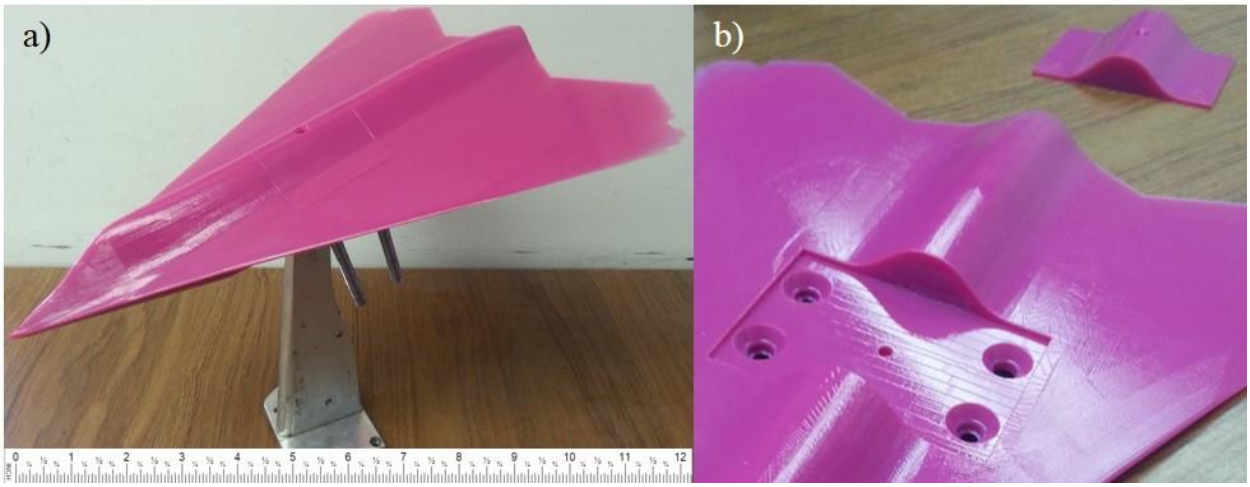


**Figure 3.6: ICE 101 1/45th scale model; a) Assembly attached to strut balance mount, b) detail of connection and cover.**

## 3.4 NACA 0012 Model

Due to size limitations of the Fortus 400mc machine, the NACA 0012 airfoil, shown in Figure 3.7 through Figure 3.9, was printed in three sections. The airfoil has a chord of 6 inches and a span of 21 inches with a 0.20c flap chord. The flap is a plain flap for simplicity of design. There are five different flap deflection angles, 0° through 20° by 5° increment. This NACA 0012 airfoil is composed of 19 pieces in total due to separation of the model into three sections.

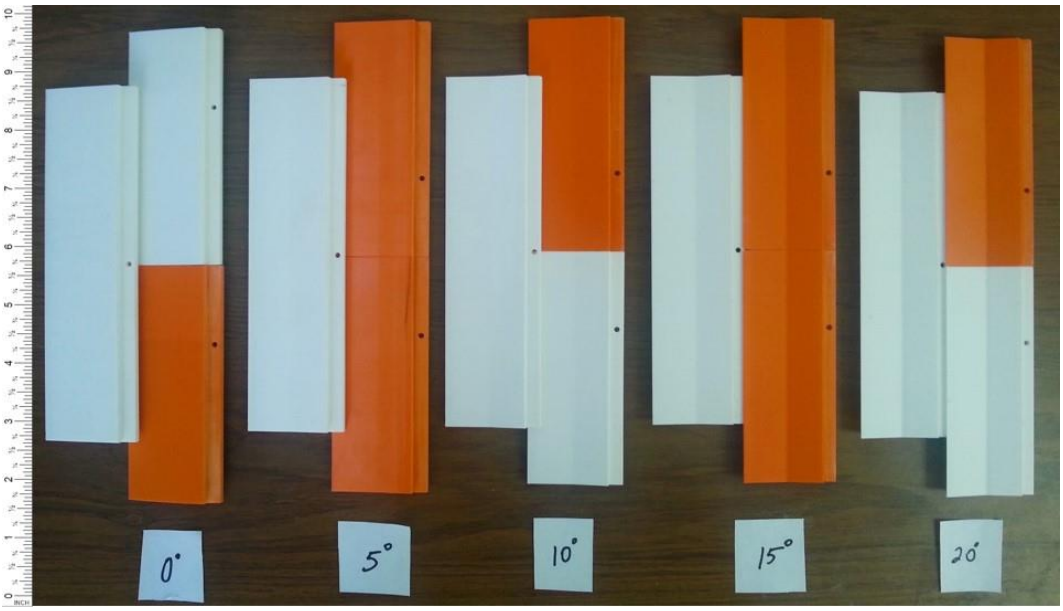


**Figure 3.7: 15 flap pieces for the NACA 0012 airfoil.**

The connection to the strut balance for WT testing is the same as described in Figure 3.5. Attempting to keep the flow over the model 2D, circular disk end plates of 8 inch diameter were printed on the two outermost parts. These endplates also help hold the flaps to the main body of the airfoil, which can be seen in Figure 3.8.

**Figure 3.8: Section of the NACA 0012 airfoil with 15° flap.**

Some of the flaps were printed in different colors because the Fortus 400mc and the uPrint SE Plus were both used to print these parts, with the uPrint containing orange ABS filament at the time. All parts are made of ABS with some slight differences; as mentioned in the description of the printers, the uPrint uses ABS*plus*™ and the Fortus 400mc uses ABS-M30. A complete

assembly of the NACA 0012 airfoil with 15° flaps mounted in the VT Open-Jet WT is shown below in Figure 3.9.

Data and RSMs from testing the NACA 0012 AM model is given in Sections 5.3 and 6.2. The threaded rods in the above figure are used to keep the sections of the model firmly pressed together and aligned. Also, the rod going through the flap pieces keeps the flaps held within the slot.

**Figure 3.9: NACA 0012 airfoil with 8" endplates mounted in VT Open-Jet WT.**

## 3.5 Delta Wing Control Surface AM

In order to get a better understanding of printing small replaceable parts, such as spoilers, with AM, a small delta wing with 6 spoilers was printed on the Replicator 2. This understanding is crucial to control surface optimization, where control surface size, position, deflection angle, and orientation may all be varied. The different spoiler configurations are shown in Figure 3.10. Furthermore, the parts are in the orientation in which they were printed. Due to the skewed nature of the bottom two parts, they could not be printed without support, which is why they were printed in the orientation shown. Each of the spoiler pieces is 0.75” chord, 1” span, and 0.25” thickness. The size of the spoilers differs since spoiler area was varied with some of the parts.

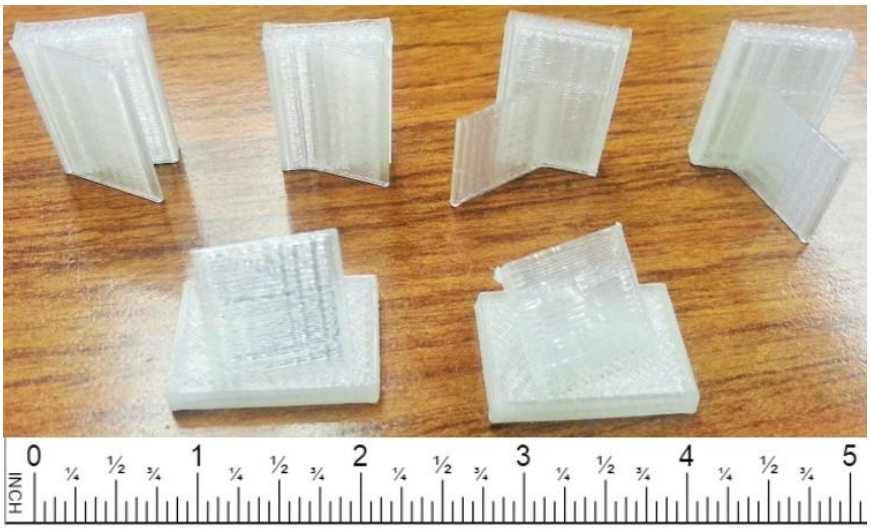


**Figure 3.10: Spoilers with different sizes, positions, orientations, and deflection angles.**

The spoilers were printed to fit within the delta wing shown in Figure 3.11. Note that there are no connections designed into the model. This model was not for WT testing but for analysis of the ability of the Replicator 2 to produce small parts and to determine the tolerance of the Replicator 2. The overall size of the delta wing is approximately 5" chord, 4" span, and 0.75" thickness.

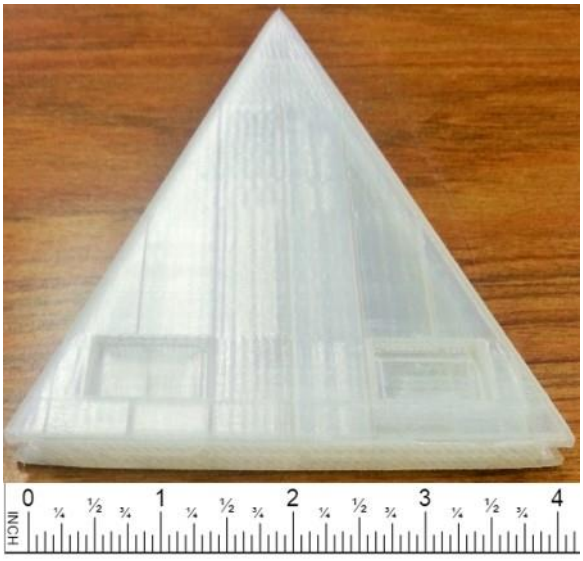


**Figure 3.11: Delta wing with replaceable spoilers.**

## 3.6 ICE 101 1/15th Scale Model

Construction of a 1/15th scale ICE 101 model was planned for further comparison to ICE 101 baseline data and for evaluating AM's ability to produce large WT models. The 1/15th scale ICE 101 model has a chord of approximately 34.5 inches and a span of approximately 30 inches.

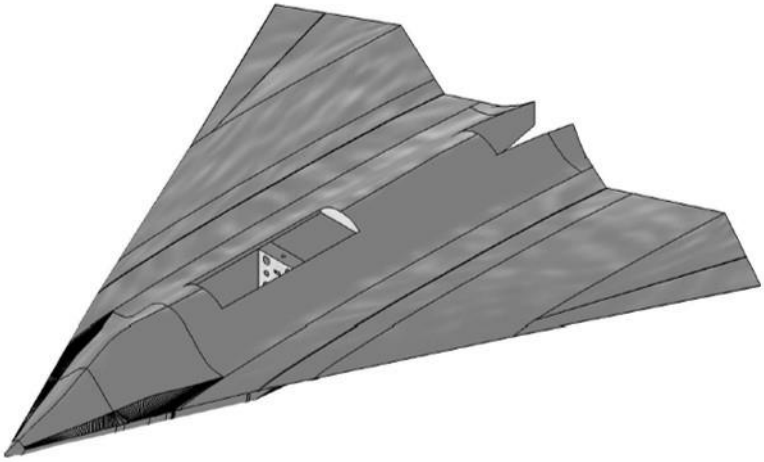

**Figure 3.12: ICE 101 1/15th scale model with sting balance connections.**

A model of this size was designed to fit the sting balance of the VT Stability Tunnel [86]. The balance is a 2 x 2 inch block, which is a challenge for the ICE 101 configuration to fit at smaller scales due to the supersonic, streamlined geometry. Furthermore, the model scale required to fit the sting balance results in limited AM machine options for printing the model in one piece for structural integrity. Only the Fortus 900mc [87] and Objet1000 [88] have print volumes capable of printing the 1/15th scale model in one piece. The Fortus 900mc was selected for further investigation of this model since the Fortus 900mc is an FDM™ machine and uses stronger engineering plastics, such as Nylon 12, than PolyJet machines. As the size of the Fortus series machines increase, the nozzle size on the print head also increases. The nozzle on the Fortus 900mc has a minimum nozzle diameter of 0.007 inches. However, the large print volume of the Fortus 900mc results in a nozzle size of 0.01 inches and above being most common.

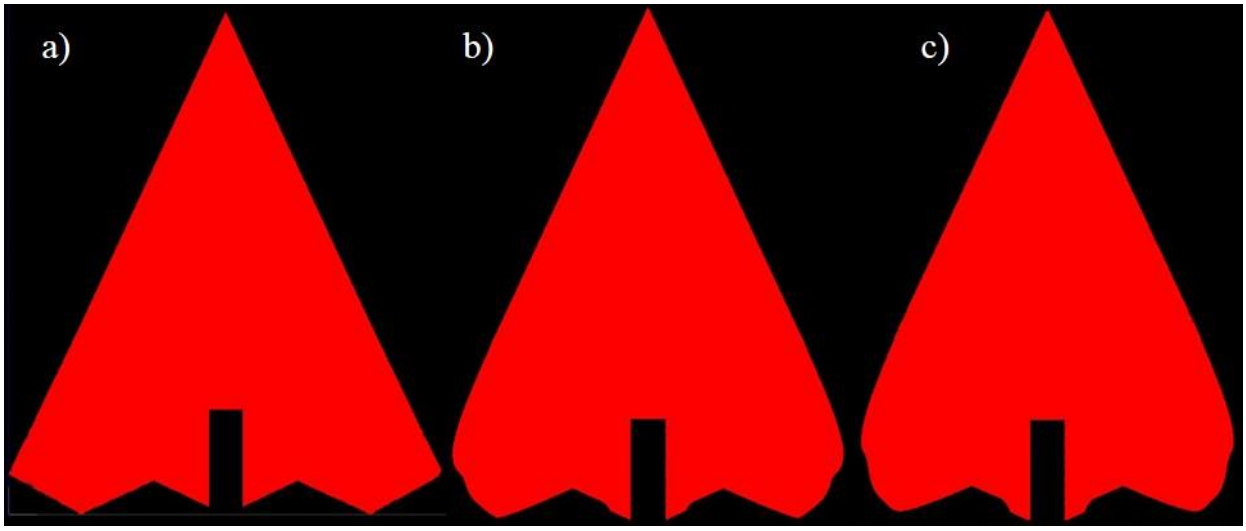


**Figure 3.13: ICE 101 1/15th scale model thickness analysis. Personal Communication, Wolf, J., "AM of the ICE 101 1/15th Scale Model," Stratasys Direct Manufacturing, 2015. Used under fair use, 2015.**

Further investigation of the ICE 101 1/15th scale model with a Stratasys representative [89] revealed issues with the thickness of the ICE 101 wing tips. Even at such a large scale, the thin wing tips of this geometry pose a challenge for AM. FDM™ is not able to produce models of this size being so thin without flexibility at this time, and PolyJet does not have the required material strength. Figure 3.13a is the 1/15th scale CAD model without any thickness analysis performed, Figure 3.13b is the model with 0.060 inch layer thickness constraints imposed, and Figure 3.13c is the model with 0.100 inch layer thickness constraints imposed. At layer thicknesses of 0.060 and 0.100 inches, wing tips and trailing edges are not faithfully produced. Even with minimum layers of 0.100 inches, there is a large potential for flexible wing tips which would bring error into WT testing. The current state of FDM™ technology is incapable of producing the ICE 101 1/15th scale model in one piece and preserving the model geometry at the wing tips and trailing edges. Alternative AM technologies and methods are proposed in Section 5.

# 4 AM Incorporation into MDO

In this chapter, the development of a strategy of incorporating AM into MDO is introduced. Section 4.1 describes the adaptations made the SBO strategy for WT data generation. Also, the DoE design implemented and the constraint optimization problem used throughout this work are given. Next, Sections 4.2 and 4.3 implement experimental data sponsored by AFRL and produced by LMTAS [41] in the development of the WT SBO strategy. In subsequent sections of this work, the data implemented in development of the WT SBO strategy is known as ICE 101 LMTAS data. Lastly, the WT SBO strategy is applied to the NACA 0012 model in Section 4.4.

## 4.1 Surrogate-Based Optimization with WT testing

This research seeks to create a process for integrating AM and WT testing into an MDO framework, which requires determination of how to use the current SOTA in AM, DoE, and RSM construction for rapid quality data generation. For this work, the SBO strategy usually involving CFD for data generation has been adapted for data generation from WT testing, shown in Figure 4.1 [90]. The green box in Figure 4.1 encompassing WT data generation is the adaptation of the typical SBO strategy of using CFD analysis for high-fidelity data generation.

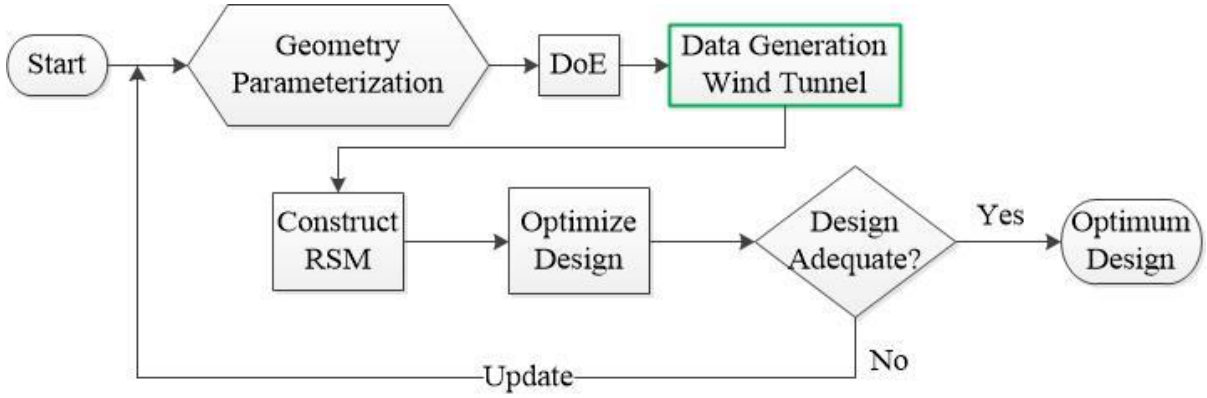


**Figure 4.1: SBO strategy adapted to incorporate WT testing. Schematic developed by author, 2015.**

The DoE block in Figure 4.1 fills a design space by creating a testing sequence for minimizing the number of design points to be WT tested while still having statistical significance for RSM. Since complete randomization is not suitable for WT testing, a split-plot design, Section 2.3.1.2, is implemented in this work. The specific HTC and ETC factors are explained later in this chapter for specific test problems. Furthermore, WT testing was performed in the VT Open-Jet

WT with a NACA 0012 airfoil and flaps. The following sections within this chapter discuss the DoE and RSM techniques implemented, as well as some test problems of the AM and WT SBO strategy.

### 4.1.1 Design of Experiments

Determining the number of points required for the DoE to populate the design space with statistical significance depends on the number of points required for a RSM. A split-plot RSM requires a minimum number of runs (design points) equal to two more than the number of terms in the RSM. The two extra runs are for estimation of the two error variance terms. However, more runs than the minimum are suggested to improve statistical significance.

A quadratic RSM has six coefficients, $\beta$ terms, which is shown in Equation 4.1. Therefore, if a two factor quadratic split-plot RSM is to be generated, 8 runs will be required as a minimum for construction of a split-plot RSM.

$$y = \beta_0 + \beta_1 x_1 + \beta_2 x_2 + \beta_{11} x_1^2 + \beta_{22} x_2^2 + \beta_{12} x_1 x_2 + \varepsilon_{WP} + \varepsilon_{SP}, \tag{4.1}$$

where $y$ is the response, $x_1$ is the WP factor, $x_2$ is the SP factor, the $\beta$ terms are the coefficients to be solved, and the ε terms are the error variances. Note that Equation 4.1 is a full quadratic response surface equation with the interaction effect between $x_1$ and $x_2$. The number of WPs is determined by the number of WP coefficients, the intercept, and the WP error variance. In this case, 4 WP runs are required to determine $\beta_0$, $\beta_1$, $\beta_{11}$, and the WP error variance [57]. The coefficients corresponding to the SP and the interaction coefficient are determined with the SP runs.

Split-plot design generation for this work was accomplished through SAS JMP® Pro software [69]. JMP® Pro is one of the only statistical software programs that has the capability of creating split-plot RSM designs. A split-plot RSM design is created through the custom design tool by noting that certain factors are HTC and that the design to be created is an RSM design. Goos *et al* [57] utilize the I-optimality design creation method which has also been implemented in this work through the JMP® Pro custom design tool. Further information on optimality for split-plot designs can be found in the following resources [58, 65].

### 4.1.2 Adaptation of Snyder's Trim Optimization Problem

The problem to be solved throughout this work is an adaptation of a test problem from Snyder's "A Toolkit for Trim" [91]. The original problem, shown in Figure 4.2, is an airfoil "trim" optimization with two factors and was implemented to test a trim optimization software.

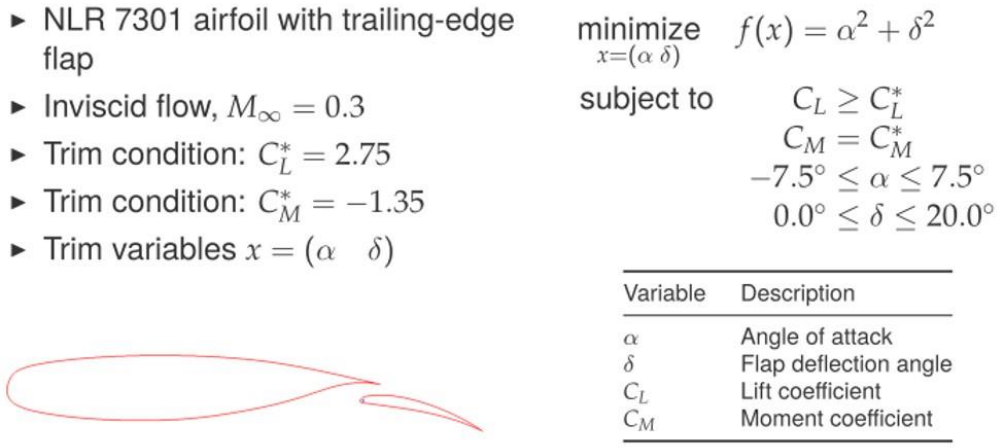


**Figure 4.2: Non-linear, fully determined "trim" problem. Personal Communication, Snyder, R., "A Toolkit for Trim," 2015. Used under fair use, 2015.**

Even though the objective function of this problem is not a take-off gross weight objective function, as is common in aircraft design, the problem is still useful for demonstrating the WT SBO strategy developed in this work. The key feature of Snyder's test problem is the deflection of a control surface on an aerodynamic body. Constraints are placed on two aerodynamic values that can be generated from WT testing, $C_L$ and $C_m$. Also, the only two variables are AoA and control surface deflection, which creates a relatively simple problem for process development and testing compared to the number of variables required for a full control surface suite optimization. Furthermore, the objective function is a simple, non-linear function with closed-form derivatives with respect to the design variables [91].

Two adaptations of this problem are implemented in this work. One is for using the WT SBO strategy developed in this work with ICE 101 LMTAS data (Section 4.2), and the other is for plain flap constraint optimization of a NACA 0012 airfoil (Section 4.4).

## 4.2 ICE 101 LMTAS Data Two Factor Optimization Problems

Utilizing ICE 101 LMTAS data allows for testing of the ability to incorporate WT data into an SBO strategy prior to AM model production and testing. The S&C data for high AoA

configurations will be nonlinear in most cases. Therefore, determining whether a split-plot RSM with a small number of points will accurately capture the design space is important. Therefore, the purpose of using the LMTAS data is not to get an optimum flap position and AoA for target conditions, but the purpose is to test the capabilities of the SBO strategy with WT data. Section 4.2.1 introduces the split-plot experimental designs developed for the WT SBO strategy using normal force coefficient, $C_N$, and pitching moment coefficient, $C_m$, ICE 101 LMTAS data with AMT deflections. Moreover, Section 4.2.2 performs similar data analysis, but with rolling moment coefficient, $C_l$, and yawing moment coefficient, $C_n$. In addition, the LMTAS data application to the WT SBO strategy is extended to three factors in Section 4.3.

### 4.2.1 $C_N$ & $C_m$ Analysis

The constraint optimization problem to be solved adapted from Snyder using ICE 101 AMT historical data is given below in Figure 4.3.

- ICE 101 w/ AMT (only 1 deflected)
- Target conditions:
  $C_N^* = 1.1, C_m^* = 0.022$
- Design Variables: $x = (\alpha\ \delta)$
  $\alpha$ = Airfoil angle of attack
  $\delta$ = AMT deflection angle

- Minimize $f(x) = \alpha^2 + \delta^2$
- Constraints:
  $C_N \geq C_N^*$
  $C_m = C_m^*$
  $0° \leq \alpha \leq 45°$
  $-10° \leq \delta \leq 60°$

**Figure 4.3: Constraint optimization problem with ICE 101 AMT normal force and pitching moment data. Developed by author, 2015.**

The target conditions were selected from Figure 4.4. Instead of selecting an arbitrary point, the particular target conditions in Figure 4.3 are selected because of their location in the non-linear region of the data, which is a potential challenge for a RSM to capture. In this constraint optimization problem, the ICE 101 aircraft is the aerodynamic body and the AMT is the control surface to be deflected. Note that the AMT data used is only for deflection of one AMT, while the other AMT is kept at its undeflected configuration of 0°.

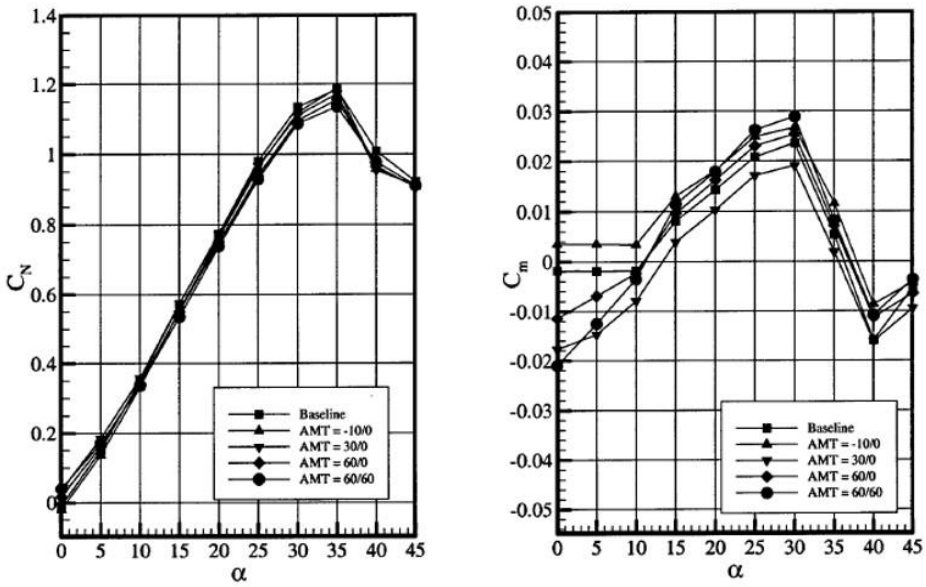


**Figure 4.4: ICE 101 LMTAS AMT data, normal force and pitching moment, for varying AoA. Dorsett, K. M., Fears, S. P., and Houlden, H. P., AFRL, "Innovative Control Effectors (ICE) Phase II." LMTAS. 1997. Report Number: WL-TR-97-3059. Used under fair use, 2015.**

Once the optimization problem is established, the split-plot RSM designs are created using the JMP® Pro custom design tool. Table 4.1 gives the settings in the custom design tool for each of the three designs that are introduced in this section. Each of the designs used an I-optimality criteria with 500 starts. The first design has both AMT deflection (HTC) and AoA (ETC) as continuous factors. This means that these factors can be any value within the range given in the design problem. The 2nd and 3rd designs have AMT deflection as a continuous factor and AoA as a discrete numeric factor. Also, there are differences in the RSMs applied to the data. A discussion of the impact of factor types and the selection of RSMs is in Chapter 6.3. Each of the designs have 4 WPs. The number of SPs per WP is 3, 5, and 10, respectively.

| Design # | # of Runs | Factor Type (AMT, AoA) | # Factor Levels | Optimality,# of Starts | Response Surface Power |
|---|---|---|---|---|---|
| **1** | 12 (4 WP) | Both Continuous | N/A, N/A | I, 500 | 2nd in AMT deflection and AoA |
| **2** | 20 (4 WP) | Continuous, Discrete Numeric | N/A, 7 | I, 500 | 2nd in AMT deflection, 5th in AoA |
| **3** | 40 (4 WP) | Continuous, Discrete Numeric | N/A, 11 | I, 500 | 2nd in AMT deflection, 5th in AoA |

**Table 4.1: ICE 101 AMT Normal Force and Pitching Moment DoE designs.**

The design points to fill the design space are shown in Table A.1 through Table A.3 and in Figure A.1 through Figure A.3. The table representation lists all of the design points and in which WPs the points reside. The figure representation show how the different WPs fill the design space. Note that in the figure representation some of the points are replicates, so there may not appear to be the full number of points as listed in the tables. Also, the tables and figures represent the design points in coded variables. For DoE, design points are usually expressed in coded variables which are within the range of -1 to 1. This makes comparison of surfaces and modification of ranges easier. Conversion from coded variables to natural variables is given by

$$x_i = \{2\xi_i - [\max(\xi_i) + \min(\xi_i)]\}/[\max(\xi_i) - \min(\xi_i)] \quad (4.2)$$

where $x_i$ are the natural variables and $\xi_i$ are the coded variables.

The data in Figure 4.4 does not align with the design points of the three split-plot designs so an interpolation scheme in two-dimensions was used to acquire the LMTAS AMT data at the design points for designs 1-3. Results and discussion of this problem are in Chapters 6.

### 4.2.2 $C_l$ & $C_n$ Analysis

Since the AMT control surface is more effective in yaw and roll control moments when only one AMT is deflected, data for the yaw and roll moments of the ICE 101 AMT configuration was used as another test case [41]. The constraint optimization problem from Snyder was adapted again to fit this data and is shown below in Figure 4.5.

- ICE 101 w/ AMT (only 1 deflected)
- Target conditions:
  $C_l^* = -0.005$, $C_n^* = -0.005$
- Design Variables: $x = (\alpha\ \delta)$
  $\alpha$ = Airfoil angle of attack
  $\delta$ = AMT deflection angle

- Minimize $f(x) = \alpha^2 + \delta^2$
- Constraints:
  $C_l \geq C_l^*$
  $C_n = C_n^*$
  $0° \leq \alpha \leq 32°$
  $-10° \leq \delta \leq 60°$

**Figure 4.5: Constaint optimization problem with ICE 101 AMT roll and yaw moment data. Developed by author, 2015.**

The changes from the last problem to this one are the target conditions, the range of AoA, and the range of AMT deflection. The target conditions are changed to roll and yaw moment coefficients, but the objective function remains the same.

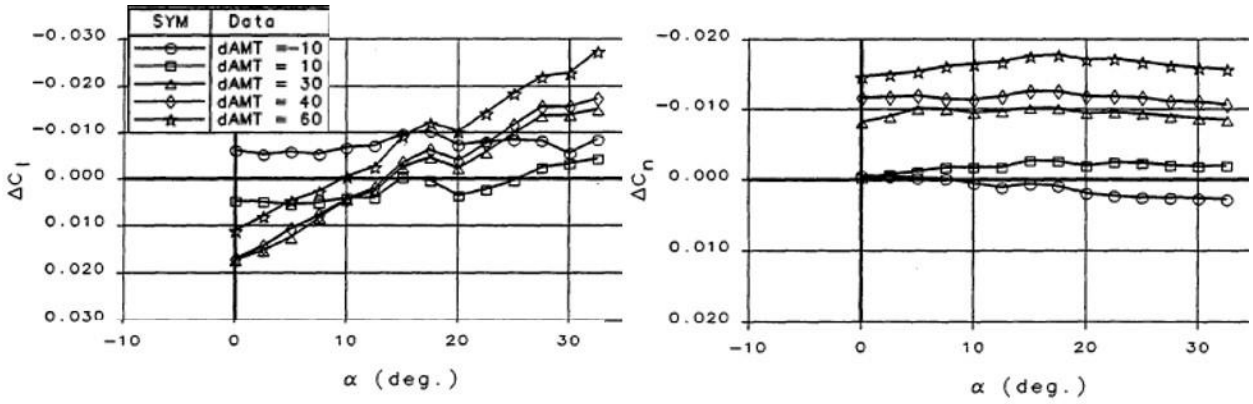


**Figure 4.6: ICE 101 LMTAS AMT data, roll and yaw moment, for varying AoA. Dorsett, K. M., Fears, S. P., and Houlden, H. P., AFRL, "Innovative Control Effectors (ICE) Phase II." LMTAS. 1997. Report Number: WL-TR-97-3059. Used under fair use, 2015.**

Three split-plot designs are created for this problem with the JMP® Pro custom DoE design tool. Once again, the designs are created with I-optimality with 500 starts. Table 4.2 shows the different design attributes. Learning from the results of the first LMTAS data problem, the roll and yaw problem started with a continuous, HTC AMT deflection factor, and a discrete numeric, ETC AoA factor with 7 levels. Also, this first design had 4 WPs and 5 SPs per WP. In the next two designs both factors are discrete numeric, with AMT deflection having 5 levels and AoA having 7 levels. Both designs have the same number of WPs (7), SPs (5 per WP), and factor types; the differences are in the RSM that was fit to the data. An explanation of changing AMT deflection from continuous to discrete numeric is in Chapter 6.

| Design # | # of Runs | Factor Type (AMT, AoA) | # Factor Levels | Response Surface Power |
|---|---|---|---|---|
| **1** | 20 (4 WP) | Continuous, Discrete Numeric | N/A, 7 | 2nd in AMT deflection, 5th in AoA |
| **2** | 35 (7 WP) | Both Discrete Numeric | 5, 7 | 2nd in AMT deflection, 5th in AoA |
| **3** | 35 (7 WP) | Both Discrete Numeric | 5, 7 | Max Power + Backwards Elimination |

**Table 4.2: ICE 101 AMT Roll and Yaw Moment DoE designs.**

As with the normal force and pitching moment problem, the design points of the above three designs are shown in Table A.4 and Table A.5. Also, a graphical representation of the design space is given in Figure A.4 and Figure A.5. Since designs 2 and 3 are the same except for the

RSMs, the design points and graphical representation are the same. Moreover, the same interpolation scheme is implemented again for generation of the response data at the design points.

## 4.3 ICE 101 LMTAS Data Three Factor Optimization Problem

The ICE Phase II report produced by LMTAS [41] contains roll and yaw moment experimental data for three sizes of AMT. The different AMT sizes are shown below in Table 4.3. Even though the skewed AMT has a slightly different configuration than the small and large AMT, the size of the skewed AMT is still in between the other two configurations. For the purpose of this test problem, the skewed AMT is treated as if it had the same configuration as the other two, thus making it roughly a medium AMT.

| Description | Area ($in^2$) | Arm (in) | Volume Ratio |
|---|---|---|---|
| **Small AMT** | 1.30 | 5.00 | 0.0079 |
| **Skewed AMT** | 1.79 | 6.24 | 0.0136 |
| **Large AMT** | 2.57 | 4.68 | 0.0147 |

**Table 4.3: ICE 101 LMTAS AMT sizes [41].**

The purpose of this test problem is to see how the WT SBO strategy scales up to three-dimensions. The WT data incorporation process is planned to be used for a full control effector suite that may have 20 or more factors, so scaling from two to three factors is a good first step to assess the impact on the process. Increasing the number of factors does change the problem to be solved, as seen in Figure 4.7.

- ICE 101 w/ AMT (only 1 deflected)
- Target conditions:
  $C_l^*$ = -0.005, $C_n^*$ = -0.005
- Design Variables: $x = (\alpha\ \delta\ A)$
  $\alpha$ = Airfoil angle of attack
  $\delta$ = AMT deflection angle
  A = AMT area/size

- Minimize $f(x) = \alpha^2 + \delta^2 + A^2$
- Constraints:
  $C_l \geq C_l^*$
  $C_n = C_n^*$
  $0° \leq \alpha \leq 32°$
  $-10° \leq \delta \leq 60°$
  A= S, M, or L

**Figure 4.7: Constraint optimization problem with ICE 101 AMT roll and yaw moment and AMT size data. Developed by author, 2015.**

The AMT size factor is a HTC, discrete numeric factor with three levels. Now the design has two HTC factors, AMT size and AMT deflection angle. The minimum number of WPs and runs for this design space is 8 WPs and 16 SPs; however, for additional replication and since AoA

is an ETC parameter, 2 more WPs were added and the number of SPs per WP was increased to 5 resulting in 50 runs total. The coded variable design points are shown in Table A.6. Since this problem is now three-dimensional, the same two-dimensional plots as with the other designs do not give a good representation of the design space with design points. Figure A.6 is a representation of the design space for the three factor problem with the different colors representing the WPs. The interpolation scheme was slightly adapted from previous problems now that a different data set is referenced for each AMT size.

## 4.4 NACA 0012

The NACA 0012 problem tests the developed WT SBO strategy with the use of an AM model and WT testing for data generation. Section 4.4.1 introduces the constraint optimization problem adapted from Snyder for use with the NACA 0012 model. Details of the WT facilities used for testing and corrections for the Open-Jet WT data are given in Appendix B. The Open-Jet WT was selected for this testing because the tunnel is readily available, easy to use, and has a low operation cost.

### 4.4.1 Experimental Design

The next SBO problem is for a NACA 0012 airfoil with plain flaps. For this problem, the data was collected from an AM model (Section 0) in the VT Open-Jet WT. The SBO problem to be solved is given below in Figure 4.8. Furthermore, the AM NACA 0012 model in the Open-Jet has a low Reynolds Number, so baseline (0° flap deflection) experimental data from Jacobs *et al* [92] is used for comparison.

- NACA 0012 w/ plain flap (0.2c)
  - 6 in chord
  - Mach = 0.073, Re = 0.23e6
- Target conditions:

  $C_L^* = 0.6,\ C_m^* = -0.06$
- Design Variables: $x = (\alpha\ \delta)$

  $\alpha$ = Airfoil angle of attack

  $\delta$ = flap deflection angle

- Minimize $f(x) = \alpha^2 + \delta^2$
- Constraints:

  $C_L \geq C_L^*$

  $C_m = C_m^*$

  $0° \leq \alpha \leq 10°$

  $0° \leq \delta \leq 20°$

**Figure 4.8: Constraint optimization problem with NACA 0012 WT data. Developed by author, 2015.**

Lessons learned from the application of AMT LMTAS data applied to an SBO strategy, drove the design for the NACA 0012 WT testing. A custom design was generated in JMP® Pro with I-optimality and 500 starts, Table A.7. The design has two discrete numeric factors, AoA (ETC) and flap deflection angle (HTC). The AoA factor has 7 levels and the flap deflection angle factor has 5 levels. Moreover, there are 7 WPs with 5 SP runs per WP resulting in a total of 35 runs. A graphical representation of the design is given in Figure A.7.

# 5 AM Results and Discussion

This section presents results of the different AM models introduced in Section 3 in terms of surface finish, print time, print cost, successes, and challenges. As mentioned previously, AM does not have a standard way of estimating print time. The time to produce a part is highly dependent on the geometry of the part. Tables detailing each of the parts printed for this work are presented to give a rough estimate of print times and cost. Although print time is difficult to determine for AM, cost can be roughly estimated from the CAD geometry. Since cost is dependent on the amount of material, model and support used, the cost can be estimated by the volume of the CAD geometry and a volume estimate support material needed. In addition, if an AM machine is accessible, most software for AM machines give a rough estimate of print time and material needed. However, the estimate of print time can often be overestimated. Also, the effectiveness of the AM results is discussed in Section 5.5.

## 5.1 ICE 101 1/27$^{th}$ Scale AMT & Mounting Block

As introduced in Section 3.2, the purpose of these first parts was to test the connection of the AMT to the main body and to test the connection of the ICE 101 body to the strut balance. An issue that arose with the AMT connection was the torsion of the square shaft. Since the shaft is a long slender piece and the AM material used for this part is not as strong as aluminum or steel, the shaft twists with relative ease. Another issue with the AMT connection was the difficulty of support material removal. This print was produced with PolyJet printing, which uses a gel-like material for support removed with a water-jet in post-processing. The geometry of the shaft, square, resulted in support material being left in the shaft cavity. A square shaft was chosen over circular because layers would be less visible with a square shaft. However, with the fine layer resolution ability of PolyJet, a circular shaft would be a better choice for support material removal.

For both the parts, the surface roughness was smooth with the exception of faceting from STL file generation. When the CAD files were converted to an STL file, the resolution of the conversion was not fine enough, resulting in faceting on the printed parts. An issue that arose with the mounting block parts was the tolerances; the top piece did have tolerances incorporated into it, but this was not enough for the machine that the part was printed on. The top cover does fit onto the main body part, but the part is difficult to remove since the tolerance is too tight. However, the

tolerances on the mounting section on the bottom side of the model were not correct. This was later found out to be an inconsistency of the dimensions on the strut balance mount. With some sanding during post-processing, the mounting block was able to fit on the strut balance mount. Table 5.1 below details the cost and time for the 1/27$^{th}$ scale ICE 101 AMT plus body section and the strut balance mounting configuration with top cover.

| **Part Name** | **1/27$^{th}$ scale AMT** | **1/27$^{th}$ scale Mounting Block** |
|---|---|---|
| **Material Cost** | ~$40 | ~$100 |
| **Pre-/Post-Processing Time** | ~30 min. - 1 hour | ~30 min. |
| **Print Time** | ~3 hours | ~ 7 hours |

**Table 5.1: First prints, total cost and print times.**

### 5.1.1 Control Surface Blowback Effect

As mentioned in the previous section, the long, slender AMT connection resulted in significant torsion in the part with a small force applied. The challenge of the AMT is the small size required of the connection. Although the torsion of the AMT connection may be attributed to the slender shaft and the material properties, control surface blowback is a common occurrence. Control surface blowback occurs when a control surface deflects in the flow to an angle other than the nominal angle of deflection. With high-lift devices fully deployed on transport aircraft, the angle of deflection can differ as much as 5° [93]. Figure 5.1 shows the results of testing the AMT in the Open-Jet WT. The AMT test model, and main body, was mounted in the test section while the flow speed was varied and pictures were taken. Using image processing software, the deflection angle was calcuated at the various flow speeds. In Figure 5.1, the dynamic pressure is plotted against the AMT deflection angle. By fitting a quadratic polynomial to the data, a 1 m/s change in flow speed results in approximately an 0.25° change in AMT deflection angle. If the deflection angle in flow differs from the nominal angle, then the quality of the data is likely to be poor.

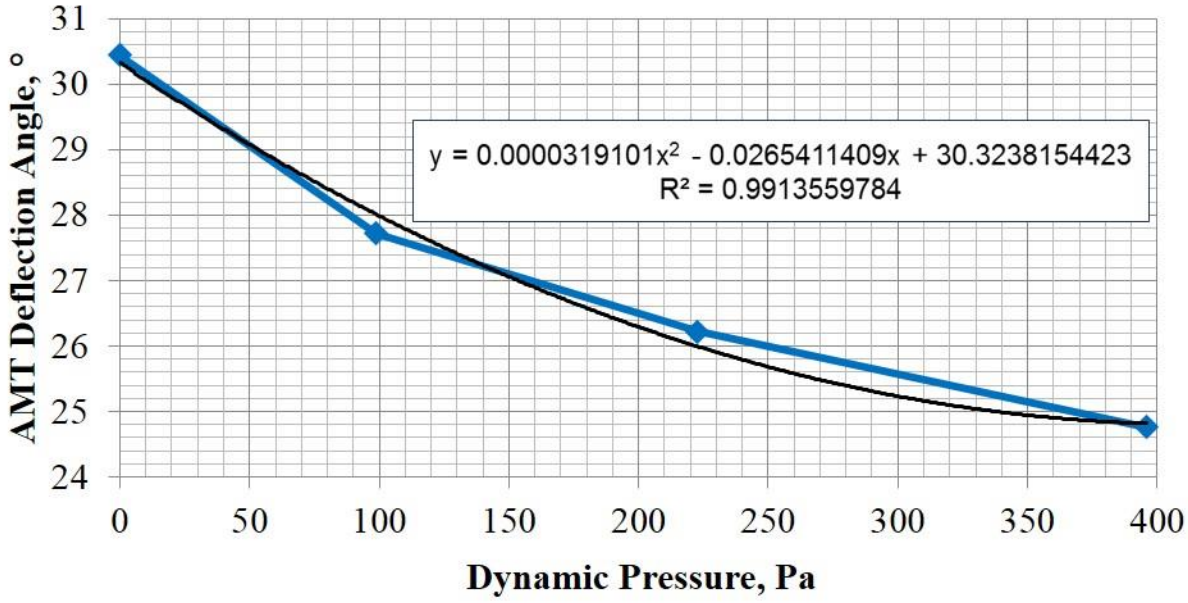


**Figure 5.1: Control surface blowback data for ICE 101 1/27th scale AMT.**

## 5.2 ICE 101 1/45th Scale Model

The 1/45$^{th}$ scale ICE 101 model was printed for testing in the VT Open-Jet WT for comparison to experimental data from Dorsett [39]. The model scale was decreased from the 1/27$^{th}$ scale printed first, in an attempt to minimize the deflection of the flow out of the open test section. However, the decrease in scale resulted in the wing tips of the model becoming more thin and fragile, chipping during post-processing. The wing tips were reshaped by sanding the model to prevent flapping of the thin tips and to prevent the model chipping further while in the WT. This modification of the geometry by sanding does introduce some unknown error into the WT testing since the changes in the data due to the sanding of the wing tips are unknown. After discoveries with tolerance on the first iteration of parts using PolyJet, the tolerances of the top cover and of the mounting configuration on the bottom were increased.

| **Part Name** | **1/45$^{th}$ scale ICE 101 Baseline** |
|---|---|
| **Material Cost** | ~$350 |
| **Pre-/Post-Processing Time** | ~30 min. - 1 hour |
| **Print Time** | ~10 hours |

**Table 5.2: ICE 101 baseline model, print time and cost.**

The above table gives the approximate cost and time to produce the 1/45$^{th}$ scale model. The pre-/post-processing time comes from preparation of the machine for printing and removal of support material once printing completed.

The model tested was a baseline configuration with control surfaces at a zero deflection angle. As with the NACA 0012 model, the 1/45$^{th}$ scale ICE 101 model was mounted on a strut strain gage balance for acquisition of forces and moments. Furthermore, the model was tested at a Reynolds number of approximately 0.51 x 10$^6$. The lift coefficient and pitching moment coefficient data are shown in Figure 5.2 and Figure 5.3 respectively.

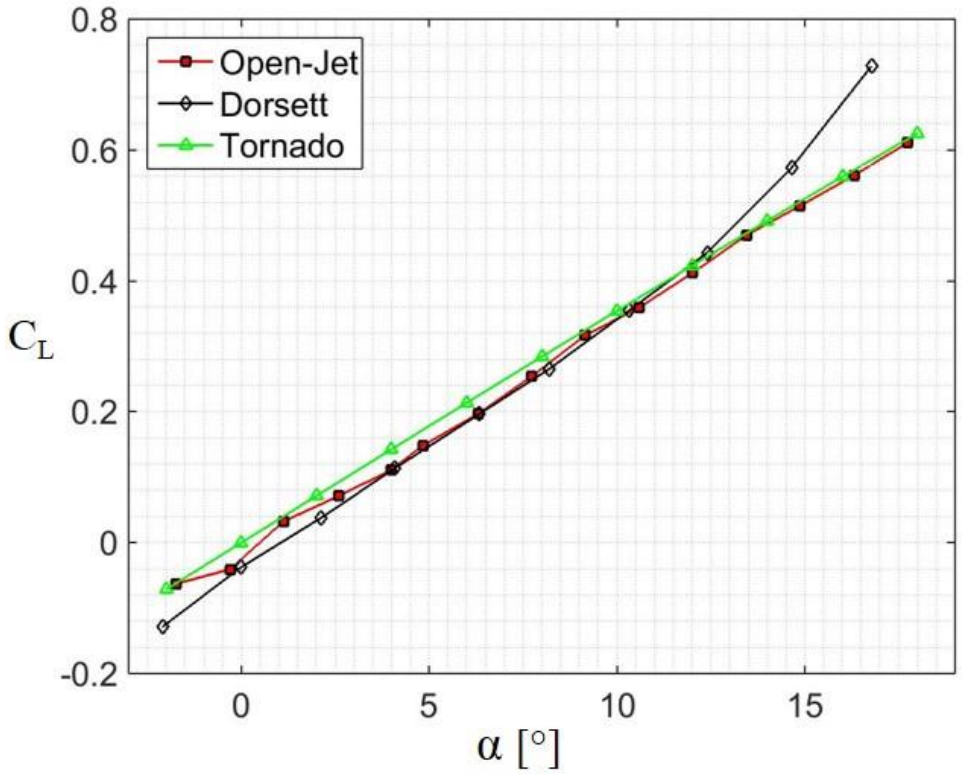


**Figure 5.2: ICE 101 1/45th scale Open-Jet WT lift coefficient versus AoA.**

The figures compare data from Dorsett [39] which is initial WT testing of the ICE 101 configuration tested at a Reynolds number of 2.0 x 10$^6$. Furthermore, a flat plate ICE 101 geometry was constructed and tested in Tornado [94]. In the range of 1 to 12 degrees AoA, the Open-Jet WT data compares well with the lift coefficient data from Dorsett. Above approximately 12 degrees AoA the Open-Jet WT becomes ineffective for data generation due to the flow being deflected out of the test section.

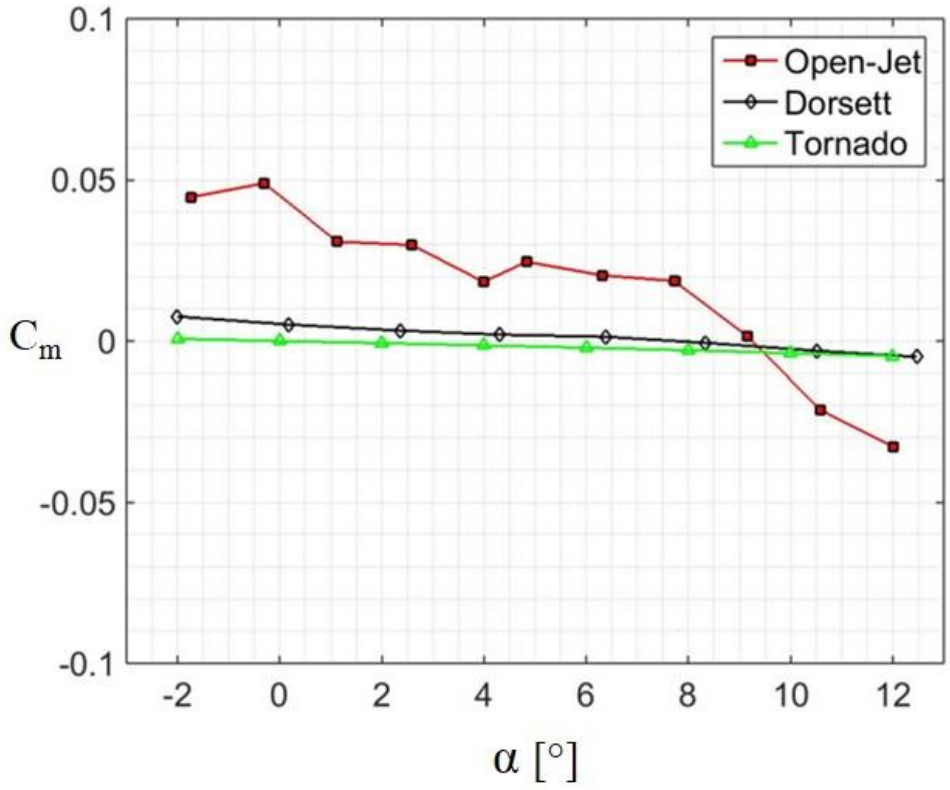


**Figure 5.3: ICE 101 1/45th scale Open-Jet WT pitching moment coefficient versus AoA data.**

The data in Figure 5.3 is pitching moment for the ICE 101 configuration about the moment reference point, which is 38% of the mean aerodynamic chord. The pitching moment data acquired from the Open-Jet WT does not match well with other data. The inability to accurately determine axial (drag) force with the strut balance in the Open-Jet WT is the primary contributor to the inaccurate pitching moment data. Another source of error is the flow being deflected out of the test section as noted for the lift coefficient above, which is seen in the slope decrease after 8 degrees AoA. More information on the corrections and challenges with the VT Open-Jet WT are given in Appendix B.

## 5.3 NACA 0012

The NACA 0012 airfoil model was printed on the Fortus 400mc and the uPrint SE Plus to reduce print time to meet a WT testing deadline. However, both printers used ABS material. Parts were oriented vertically for printing to preserve airfoil shape and minimize stair-stepping surface finish. Prior to the vertical orientation, two flaps were tested in the horizontal orientation to test the surface quality. Although the nozzle and print speed were not at the finest resolution, the Fortus 400 mc

and the uPrint SE Plus do not have the layer resolution to create an airfoil that is smooth in the horizontal orientation.


**Figure 5.4: Flaps printed in horizontal orientation with visible stair-step surface finish.**

Table 5.3 shows the overall print time and cost for the NACA 0012 model. The support material for the FDM™ machines is dissolvable resulting in a longer post-processing time. The total print time for all 19 parts was approximately 48 hours and the post-processing time was approximately 12 hours.

| Part Name | NACA 0012 with 5 flap deflections |
|---|---|
| **Material Cost** | ~$600 |
| **Pre-/Post-Processing Time** | ~12-14 hours |
| **Print Time** | ~72 hours |

**Table 5.3: NACA0012 model, print cost and time.**

## 5.4 Delta Wing Control Surface AM

Since the spoilers and delta wing are not meant for any aerodynamic or structural testing, the parts were printed with only ten percent infill. This results in a low amount of material use and fast print time. The 4 spoilers printed on their side, vertically, had a smoother surface finish and more strength compared to the skewed spoiler parts. The skewed spoilers were printed so that the flap

created an overhang during printing resulting in a part with poor surface finish and strength. Furthermore, the only post-processing for these pieces is removal of rafting, which is a layer below the parts to help with adhesion to the print bed since the Replicator 2 print bed is not heated.

| **Part Name** | **Delta wing and 6 spoilers** |
|---|---|
| **Material Cost** | < $5 |
| **Pre-/Post-Processing Time** | < 30 min. |
| **Print Time** | ~2 hour |

**Table 5.4: Delta wing and spoilers, total cost and time.**

## 5.5 AM Effectiveness

For AM, the quality factor is the ability of the AM technology to produce a part with dimensional accuracy, structural integrity, and a smooth surface finish. The acceptance factor is the cost and time to produce a model, including post-processing. In this work, PolyJet and FDM™ are evaluated for effectiveness with the above metrics. There are no general rules for AM cost or time because of the differences among AM technologies. Furthermore, even different machines of the same AM technology can have differences in effectiveness.

### 5.5.1 Quality Factors of AM Parts

There were several issues discovered with the quality of the AM parts produced in this work. Some of the issues were due to inexperience of the author in operating AM technology, and others were due to shortcomings of the AM technology itself.

#### 5.5.1.1 Torsional Resistivity

One of the first issues that arose was torsional resistivity of AM parts that are load/moment bearing. The ICE 101 1/27$^{th}$ scale AMT (Section 5.1 and Figure 3.4) part suffered from control surface blowback due to the long, slender shaft used to connect to the main body. The blowback effect (Figure 5.1) resulted from the low material strength and torsional rigidity of a small AM part, as well as from the design of the AMT connection. The thin wing tip section of the ICE 101 configuration does not leave much space for a connection at small model scales. To improve the control surface blowback effect, a new connection should be designed with possibly two shafts for connection to the main body. Another potential solution is to create AMT sections that are printed with part of the body attached and then two body sections attach to each other with multiple shafts.

This design requires more support material that increases as the deflection angle of the AMT increases, which was why the design was avoided in the first AMT part.

#### 5.5.1.2 Thin, Sharp Surfaces

Another issue faced with the ICE 101 models were the thin, sharp edges. With a supersonic configuration, such as ICE 101, the extremities of the model are quite thin, and composed of just a few layers of material. This results in the thin surfaces being too flexible to be tested in a WT, as the wing tips would flap in the flow. Furthermore, the model tends to chip easily in these regions of few layers. In the case of the $1/15^{th}$ scale model (Section 3.6), the larger scale resulted in selection of the Fortus 900mc machine because of the larger print volume. However, the larger machine has a minimum nozzle diameter that is larger than smaller FDM™ machines. The larger nozzle size in model geometry modification since the Fortus 900mc was unable to produce layer thicknesses near the wing tips.

#### 5.5.1.3 Support Material Removal and Material Strength

Model brittleness is a concern for PolyJet printing during post-processing because a water-jet is used for support material removal. Furthermore, support material removal from PolyJet printing can be challenging with small cavities because the support material is not soluble as with FDM™ support material. The materials used in this work, with the exception of the material planned for the ICE 101 $1/15^{th}$ scale model (Nylon 12), were not the strongest materials for PolyJet or FDM™. Newer, stronger AM materials have an increased cost compared to the baseline materials, which is why the baseline materials were used throughout most of this work. However, model strength can always be improved by increasing material strength or even adding metal stiffening plates.

#### 5.5.1.4 Print Orientation

Print orientation has a large impact on the overall quality of an AM model. For FDM™ processes, aerodynamic geometries were found to be of best quality when printed with aerodynamic shapes, i.e. airfoils, in vertical orientation. In a vertical orientation, layers are printed chord-wise resulting in the layer resolution of the printer not having an impact on the surface finish of an aerodynamic shape. Moreover, print orientation has a large impact on the cost and time of a part as discussed in the next section. For PolyJet printing, print orientation is not as important for surface finish due to the fine layer resolution ability of the Connex3. However, one factor that does impact the surface finish of the PolyJet parts is the resolution of the STL file. When creating a STL file from a CAD

geometry there are options for setting the resolution of the triangles used to create the file. A smaller resolution does result in a larger model file size, which will impact the time of pre-processing and time to produce a model.

Also, print orientation has an impact on the strength of the model. When a model is printed in a vertical orientation, resistance to load in the chord-wise direction is dependent on layer adhesion. FDM™ parts are anisotropic due to the layer-by-layer construction method; therefore, parts have less strength when loaded perpendicular to the layers. One way to strengthen the parts is to add filleting along sharp corners. Rounded edges increase the strength by decreasing stress concentrations. Another challenge with print orientation was discovered when printing small spoilers. The skewed spoilers, ones printed with orientation other than parallel to the span, were printed in a flat orientation requiring overhang for the spoiler section of the control surface part. Furthermore, the overhang was printed at an angle from the AM machine coordinate system which resulted in poor surface finish and strength of the skewed spoilers. A solution to this problem is to print the spoilers so that the spoiler orientation aligns with the AM machine XYZ coordinate system. The quality of the spoiler base will diminish as a result, but that can be fixed in post-processing by sanding.

#### 5.5.1.5 Tolerances

In addition to print orientation, determining tolerances for AM machines is an issue for model quality. The tolerances that should be applied to AM parts that fit together are difficult to determine due to the differences in each AM process and the dependence on machine calibration. Print bed leveling, daily weather conditions, and material type are just some of the factors that will affect the result of an AM part. For this work, the first prints made with PolyJet printing did not have the required tolerance for parts that were to fit together. Sanding during post-processing was able to fix this issue. Moreover, when creating parts with FDM™ after PolyJet, the tolerances determined for PolyJet proved too small. However, an advantage of AM is the ability to rapidly prototype. So a small model can be created to test tolerances needed for a specific machine and process before proceeding with a larger, final model.

To obtain the best quality for an AM part, the specifics of the AM process and machine being used must be known. Also, consideration of the most important attributes of a part should be understood. If a model needs to have superior surface finish, then an AM process that can use

traditional manufacturing processes in post-processing, such as SLS, may be advantageous. Or if a model is to be done quickly and at low cost, FDM™ or PolyJet may be good options. AM technology is constantly improving and new processes are being developed, so an understanding of the limitations of current technology will aid in producing models of high quality.

### 5.5.2 Acceptance Factors of AM Parts

One of the biggest challenges facing acceptance of AM is the inability to estimate print time accurately. The time required for a part is highly dependent on the individual geometry of the part. Print time is dependent on the geometry shape, size, print orientation, amount of support material, material type, CAD file size, and many more attributes of a model. Print orientation has a large impact on the time required to produce a model. For FDM™ and PolyJet, switching back and forth between model and support material is a slow process; furthermore, movement in the z-axis (vertical) is slow. Therefore, selecting a print orientation that decreases both the z height of a part and the amount of support material needed decreases the time to produce a part. Even though there is not a general rule for print time for each AM process, software for an AM machine can give an estimate of print time with the input of a CAD model. The software estimates the time based on the path that the print head will take, the amount of support material needed, and the number of times the print head will need to be switched from model to support and back. However, the estimates from the computer software can often be largely incorrect. For example, in this work the NACA 0012 parts were estimated to have a print time twice as long as the actual print time. Note that the computer software estimates were twice as long as the actual time; however, the best estimates are given by the actual AM machine itself.

The cost of producing a part with AM can be determined by the amount of model and support material needed. This can be determined by a volume calculation in CAD software. A more accurate representation of material use comes from software for each individual AM machine. The software will generate the support material structures needed. Furthermore, if a part is going to be sparse filled, a basic estimate of volume from CAD software will not be accurate. The best way to come up with an estimate of cost and time to produce a model is to process the STL file to the point which it has been uploaded to the AM machine for printing. However, this requires preparation of the AM machine for actual printing. The next best representation of the

cost and time required is to run a STL file through software which slices the file, generates tool paths, and determines support structures.

A goal of this work is to determine whether AM WT models can be produced with greater effectiveness than traditional manufacturing techniques. In order to accomplish this, a vendor quote using traditional manufacturing was generated for the ICE 101 1/15$^{th}$ scale model [7]. The estimated cost for the traditional manufacturing, CNC an aluminum block, of the ICE 101 1/15$^{th}$ scale model is $50,000, and the total time to delivery was estimated to be 45 days. Producing the same model with FDM™ and Nylon 12 material, with a machine not from a third party, would cost approximately $6,000 and take approximately 60 hours of print time with roughly 24 hours of pre-/post-processing [89]. Note that this is for a baseline model without control effectors. Spoilers were estimated to cost $1,250 each for the ICE 101 1/15$^{th}$ scale model using traditional manufacturing techniques, but using AM each spoiler would cost approximately $80.

For a control effector suite SBO strategy, there will be many small control surface parts which would result in considerable differences in AM cost versus traditional manufacturing costs. For a single control effector, 6 different parameters: chord length, span width, x-position, y-position, deflection angle, and orientation angle, can be varied for determining an optimum configuration. The previous parameters are all HTC in a split-plot design due to the necessity to exchange parts on a WT model. In addition, a split-plot design for a control effector optimization may have AoA and sideslip angle as ETC parameters. If each HTC (WP) factor has 5 discrete numeric levels and each ETC (SP) factor has 7 discrete numeric levels, the resulting split-plot design has 31 WP and 62 runs. Even using a DoE, this is an impractical number of parts to produce using traditional manufacturing processes. However, using DoE and AM results in a feasible number of parts to be produced for WT testing. In addition, the AM spoiler cost estimated above is for a large model, so smaller scale testing would decrease the cost of the parts considerably.

# 6 WT SBO Strategy Development Results and Discussion

Chapter 6 presents results of the WT SBO strategy development. Results from the ICE 101 LMTAS data analysis are given in Section 6.1. Also, results from the NACA 0012 testing problem are given in Section 6.2. Both the ICE 101 LMTAS data analysis results and the NACA 0012 results present RSMs generated from WT data in the WT SBO strategy, as well as optimum results from the RSMs. Furthermore, effectiveness of the WT SBO strategy is discussed in Section 6.3.

## 6.1 ICE 101 LMTAS Data Optimization Problems

Results for the AMT optimization problems introduced in Section 4.2 are given in this section. Each of the RSMs in this chapter correspond to split-plot designs in Appendix A. Furthermore, the RSMs are searched for an optimum value. Existing data allows for random sampling of the design space for testing quality of a RSM. A tool for random sampling of a design space, Latin Hypercube Sampling (LHS) is a multi-dimensional space-filing method; a Latin square is a square in which there is only one design point in each row and each column. Therefore, LHS generalizes the space-filling of a Latin square to multiple dimensions [95]. An example of a design space filled with LHS is shown in Figure 6.1.

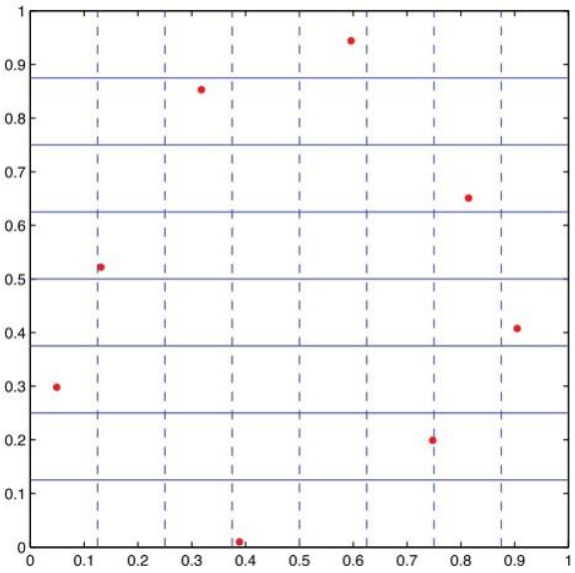


**Figure 6.1: LHS example. Fang, K., Li, R.-z., and Sudjianto, A. "Latin Hypercube Sampling and Its Modifications,"** ***Design and modeling for computer experiments*****. Chapman & Hall/CRC, Boca Raton, FL, 2006. Used under fair use, 2015.**

### 6.1.1 Two Factor $C_N$ & $C_m$ Data Results

As noted in Section 4.2, the data points for each of the experimental designs were generated using an interpolation scheme on the LMTAS data. The first design contains 4 WPs with 3 SPs in each WP for a total of 12 points in the design space. Furthermore, both the AMT deflection angle and AoA are continuous factors in the first design.

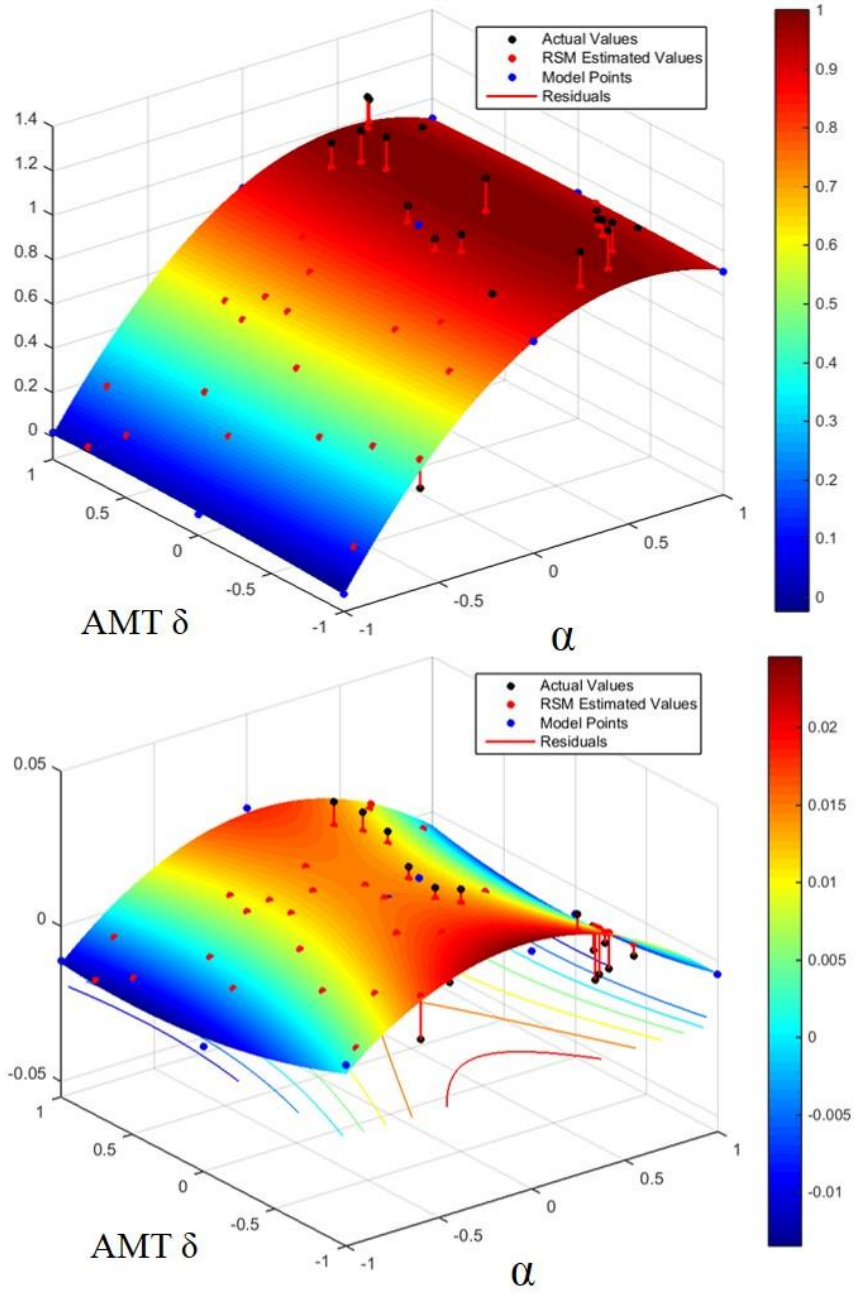


**Figure 6.2: 1st design RSMs, 4 WP & 12 SP, $C_N$ (top), $C_m$ (bottom).**

In the two RSMs of Figure 6.2, the black dots represent interpolated points according to a LHS and the red dots represent the same design points on the response surfaces. Also, the red lines are the residuals between the black and red dots. Furthermore, the blue dots are the DoE design points. The figure on the left is a plot of normal force coefficient with respect to variation in AMT deflection angle and AoA, and the figure on the right is a plot of pitching moment coefficient with respect to variation in AMT deflection and AoA. Note that the axes for AMT deflection angle and AoA are in coded units (-1 to 1). Furthermore, both the above response surfaces are quadratic polynomial regression fits to the data. The stall region (high AoA, coded units approximately > 0.5 in Figure 6.2) is not well captured by the RSM which brought about the next two designs. Two-dimensional residual plots for $C_N$ and $C_m$ are shown in Figure 6.3 to demonstrate the lack of fit in the AoA dimension.

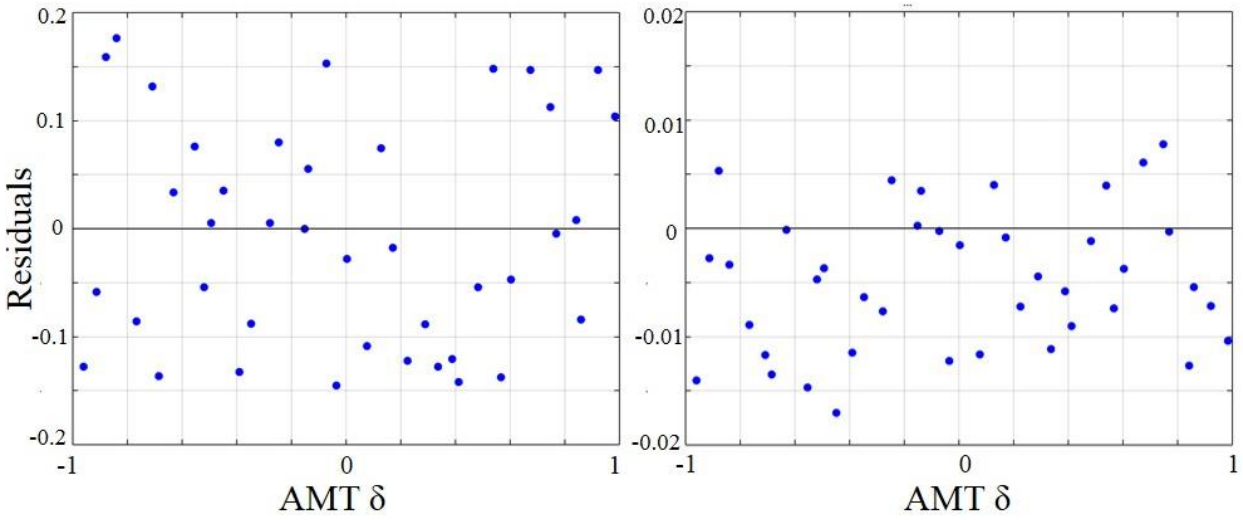


**Figure 6.3: 1st design $C_N$ (left) & $C_m$ (right) residuals v. AMT deflection angle.**

Figure 6.3 shows the residuals of $C_N$ and $C_m$ versus AMT deflection angle. The distribution of the residuals is scattered randomly which indicates a good response surface fit to the data. The only concern with the residuals versus AMT deflection angle is that the $C_m$ residuals do not have a mean of 0. So there is need to improve the 1st design.

Figure 6.4 shows the $C_N$ and $C_m$ residuals versus AoA. The distribution is not randomly scattered meaning the RSM does not fit the data well. The 2nd and 3rd designs attempt to alleviate this issue by increasing the number of factor levels in AoA.

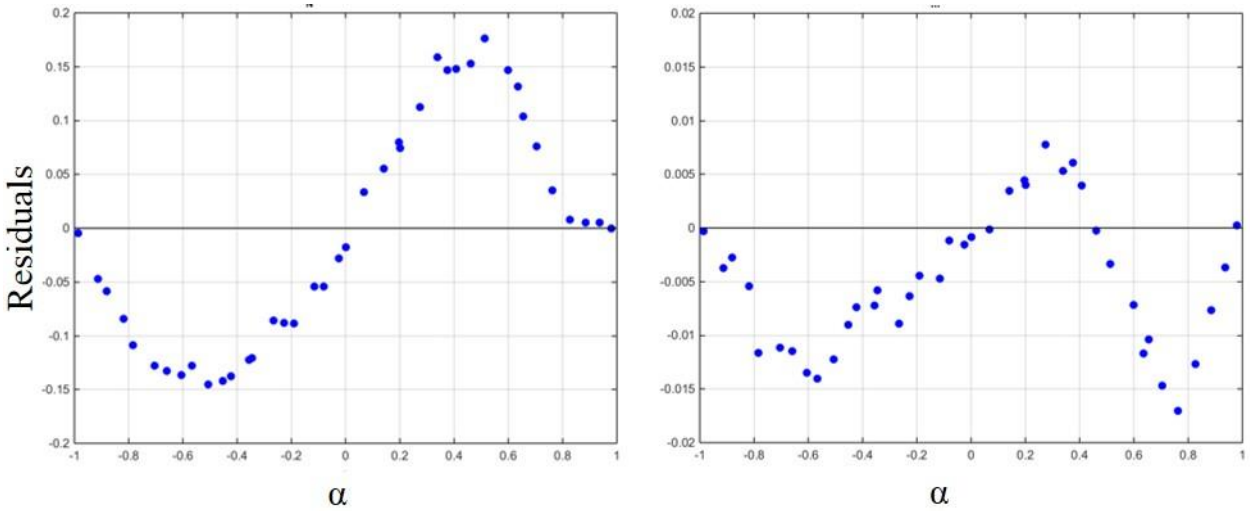


**Figure 6.4: 1st design $C_N$ (left) & $C_m$ (right) residuals v. AoA.**

The 2nd design changes the AoA factor from continuous to discrete numeric of 7 levels. AoA is an ETC factor so increasing the number of levels does not add a considerable cost or time to the WT testing. There are still 4 WPs in this design, but now there are 20 runs total, which means 5 SPs per WP.

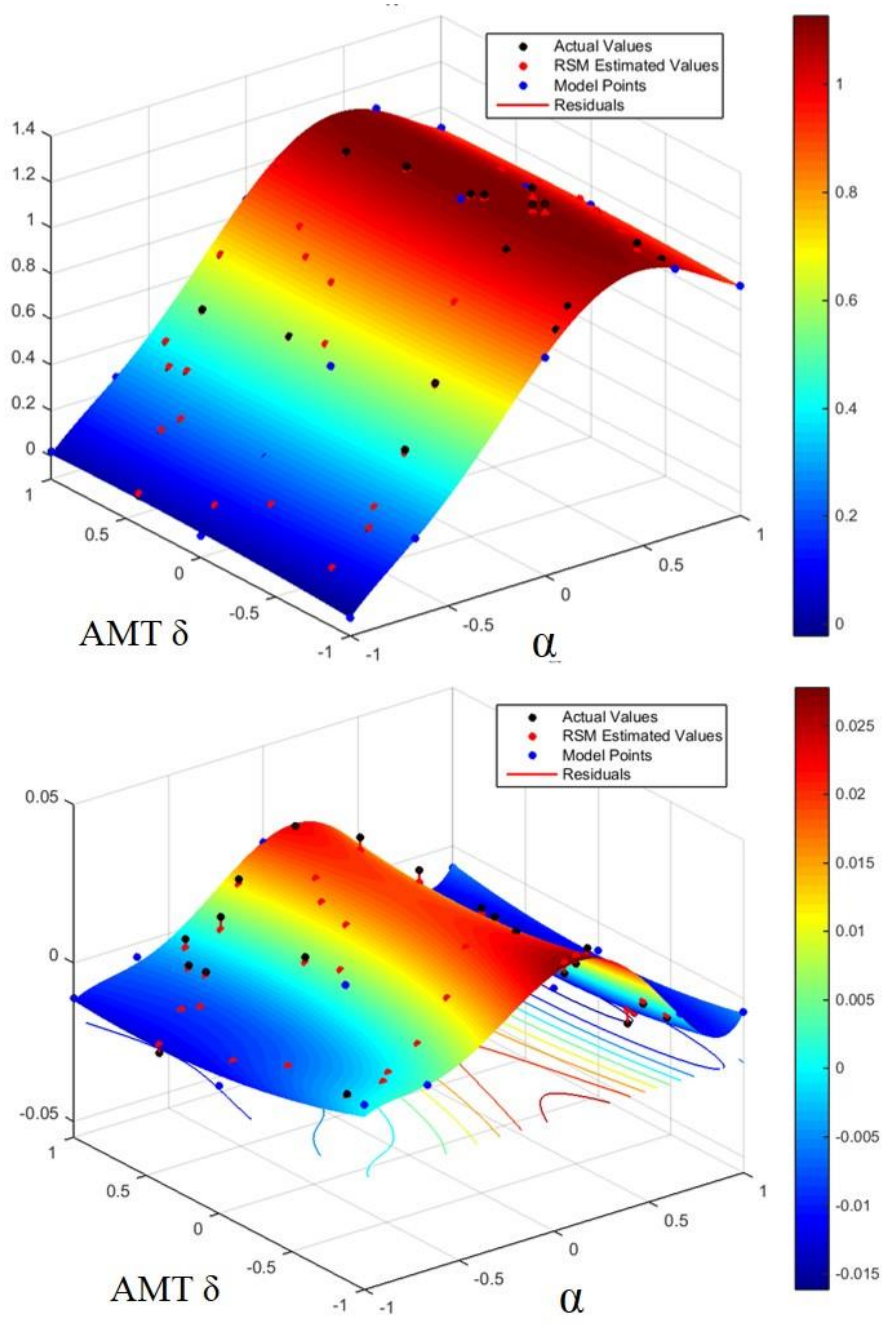


**Figure 6.5: 2nd design RSMs, 4 WP & 20 SP, $C_N$ (top), $C_m$ (bottom).**

The two RSMs in Figure 6.5 now are polynomial regressions to the 5th degree in the AoA factor. The AMT deflection angle factor is still polynomial regressions to the 2nd degree. The

residuals appear to be decreased in the response surface plots, which indicate a better fit of the response surface to the data. Further indication of this is shown in the residual plots below.

The residual distribution versus AMT deflection angle is again randomly distributed around a mean of zero as expected since the AMT deflection factor did not change for this design. Note the residuals in Figure 6.6 did decrease due to the changes in DoE and RSM.

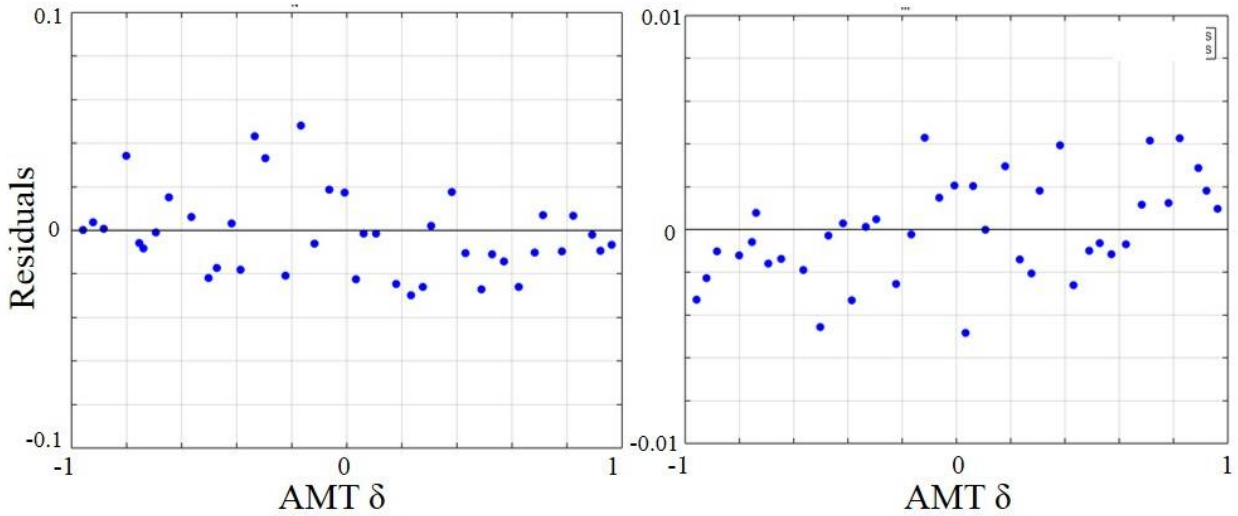


**Figure 6.6: 2nd design $C_N$ (left) & $C_m$ (right) residuals v. AMT deflection angle.**

However, the residual distribution versus AoA is still not completely random, but there is improvement in the residual magnitudes. The 3rd design increases the number of AoA levels to attempt to improve the model fit.

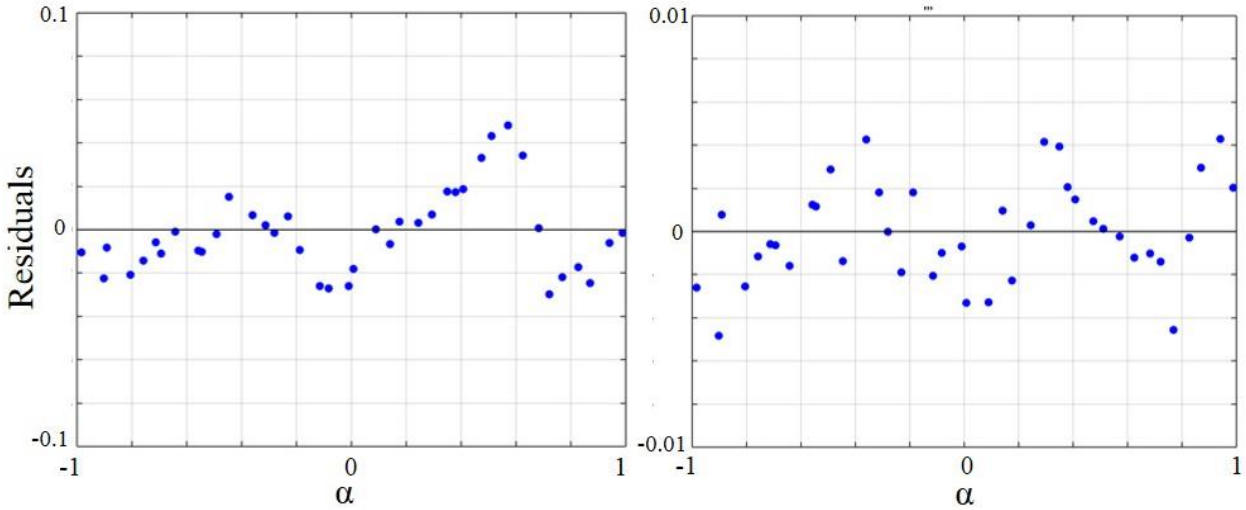


**Figure 6.7: 2nd design $C_N$ (left) & $C_m$ (right) residuals v. AoA.**

The number of AoA levels increased from 7 to 11 in the 3rd design to determine whether increasing the number of AoA levels decreased the residuals further and resulted in a better fit to the data. The 3rd design has 4 WPs and 10 SPs per WP.

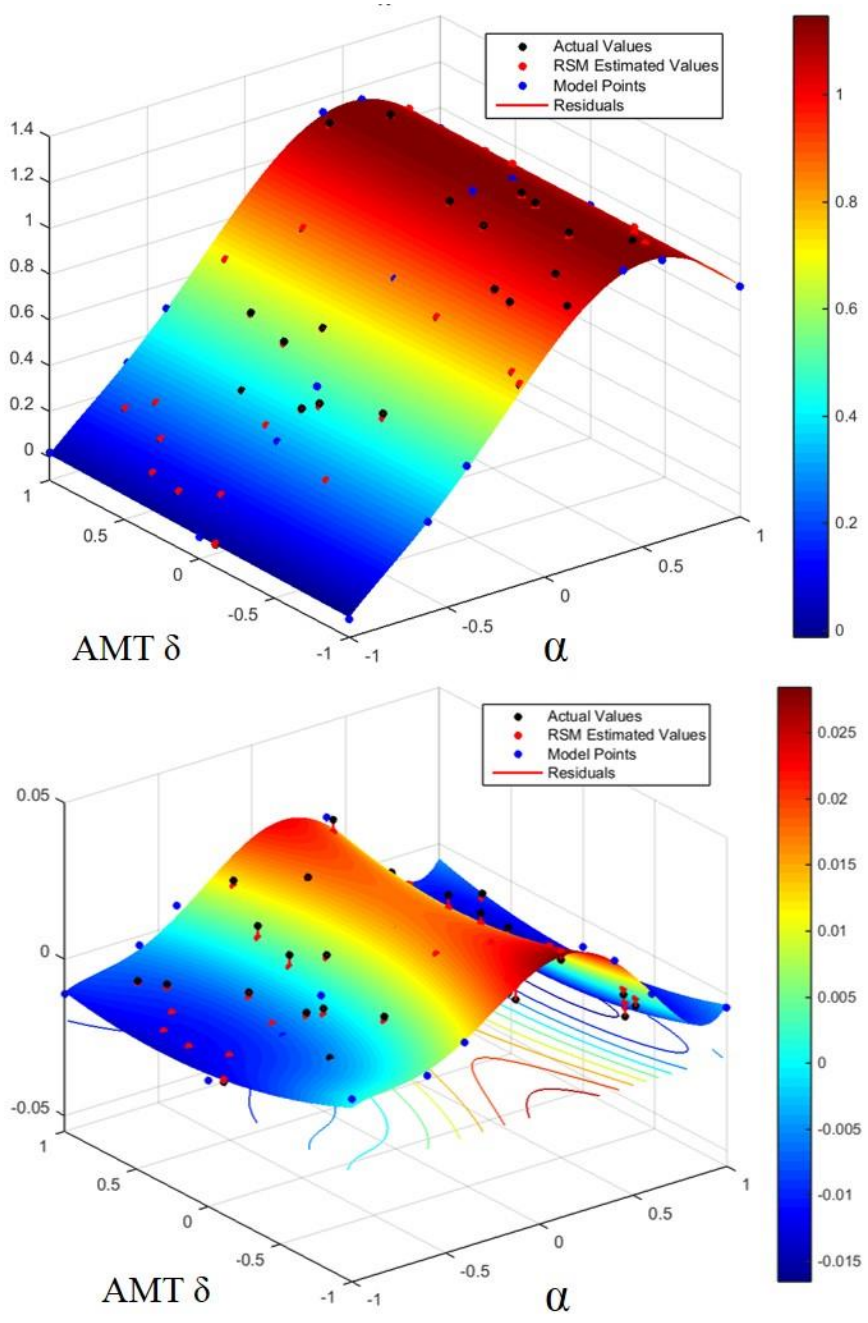


**Figure 6.8: 3rd design RSMs, 4 WP & 40 SP, $C_N$ (top), $C_m$ (bottom).**

The RSM equations for the 3rd design were the same that were used for the 2nd design. The differences between the 2nd and 3rd designs cannot be seen by just viewing the RSM plots; residual plots for further comparison are shown in Figure 6.9 and in Figure 6.10.

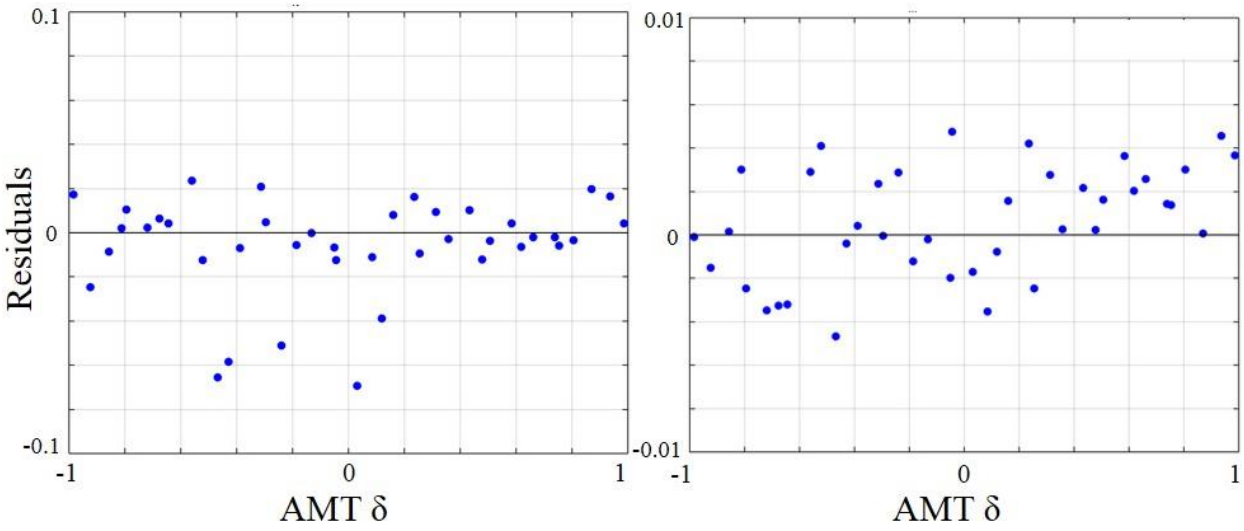


**Figure 6.9: 3rd design $C_N$ (left) & $C_m$ (right) residuals v. AMT deflection angle.**

The residual distribution versus AMT deflection angle is once again randomly distributed around a mean of zero. The residual magnitudes did not change much from the 2nd to 3rd design. For each design, the LHS changes since different programs are creating the sampling and plots. Therefore, even though there are some points of higher residuals for $C_N$ in the 3rd design that does not indicate that the model is worse at representing the data.

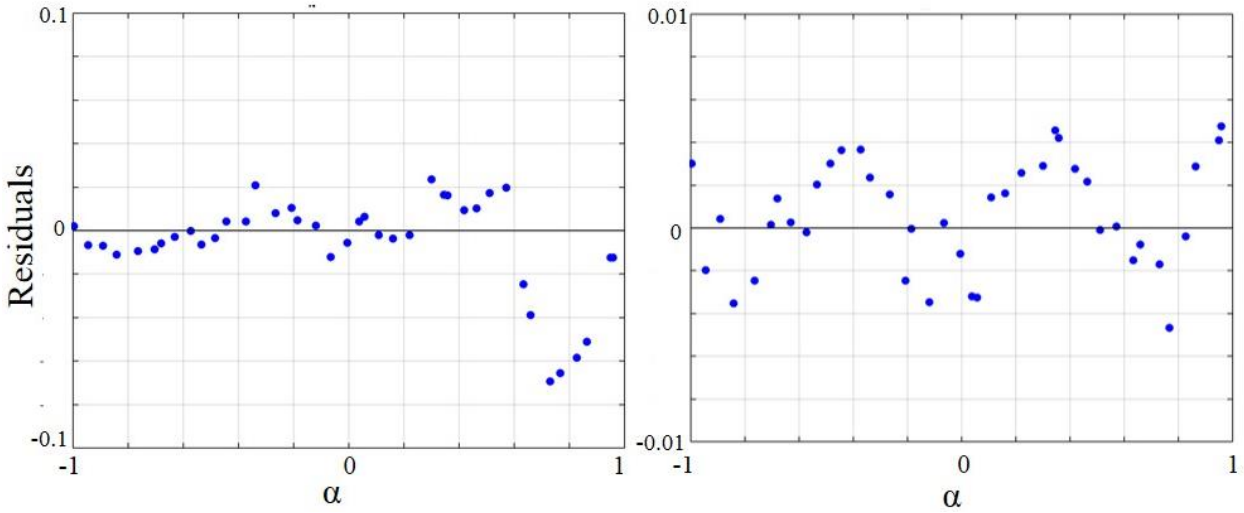


**Figure 6.10: 3rd design $C_N$ (left) & $C_m$ (right) residuals v. AoA.**

However, the residual distribution versus AoA is still not completely random. Increasing the number of AoA levels further did not improve the fit of the model. Methods for resolving the lack of fit for AoA are addressed in Section 6.3 and Chapter 7.

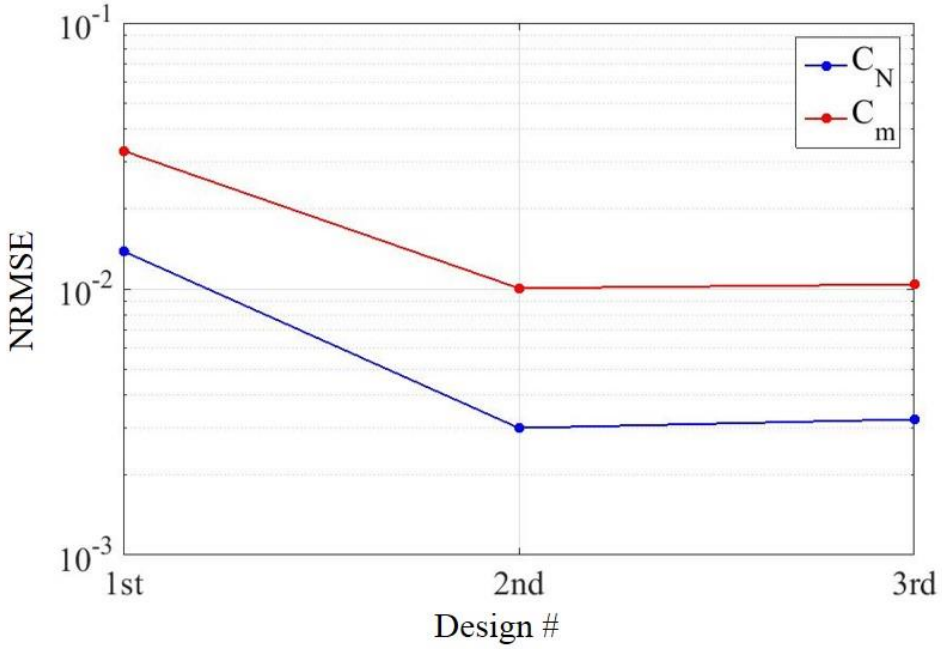


**Figure 6.11: NRMSE comparison of the three $C_N$ & $C_m$ designs.**

Figure 6.11 depicts the normalized root mean square error (NRMSE) for $C_N$ and $C_m$. There is improvement in the NRMSE from the 1st to 2nd design, but there is not significant improvement from the 2nd to 3rd design. In fact, the NRMSE for $C_N$ actually increased in the 3rd design. This indicates increasing the number of AoA levels from 7 to 11 does not benefit the RSM results for this data set.

| **Design #** | **1st** | **2nd** | **3rd** |
|---|---|---|---|
| **$\alpha$ (°)** | 34.9008 | 28.4167 | 28.6939 |
| **AMT $\delta$ (°)** | 29.8867 | 29.8385 | 25.0684 |
| **$\alpha^2 + \delta^2$** | 2111 | 1698 | 1452 |
| **$C_N$** | 1.0013 | 1.1000 | 1.1000 |
| **$C_m$** | 0.0075 | 0.0221 | 0.0219 |

**Table 6.1: $C_N$ & $C_m$ optimization results; Targets: $C_N \geq 1.100$, $C_m = 0.022$.**

Table 6.1 shows the optimization results from searching the three designs with the target conditions introduce in Section 4.2.1. The optimizations were performed using MATLAB's fmincon function which is a gradient-based constraint optimization function. The 1st design did

not converge because of RSM inaccuracy. The target constraints were not on the surface resulting in the optimizer not being able to locate a solution. The 2nd and 3rd designs have AoA and AMT deflection angles that are close to each other. However, the differences in the AMT deflection values is due to the lack of variation in $C_N$ and $C_m$ with changing AMT deflection. Therefore, any small difference in the RSMs results in a significant difference in the optimum values. The next data set is analyzed to ensure there are enough data points in the AMT deflection dimension when the variation in the data from AMT deflection is more significant.

### 6.1.2 Two Factor $C_l$ & $C_n$ Data Results

In this section, optimization results are presented for the problem outlined in Section 4.2.2. More analysis of the LMTAS data is performed because the $C_N$ LMTAS data does not have enough variation with changing AMT deflection to identify whether the split-plot design had enough AMT deflection levels. Furthermore, the purpose of using the LMTAS data is to determine whether a split-plot design can accurately or faithfully represent data characteristics with a small set of test points.

The major differences in the designs for this data set are the RSMs applied to each design. The 1st design still has a continuous AMT deflection factor, but the 2nd and 3rd designs both have a discrete numeric AMT deflection factor. The 1st design is created from knowledge of the first LMTAS data analysis; AoA must be a discrete numeric factor to more accurately capture the variation with angle of attack. Moreover, the 1st design has 4 WPs and 20 SPs.

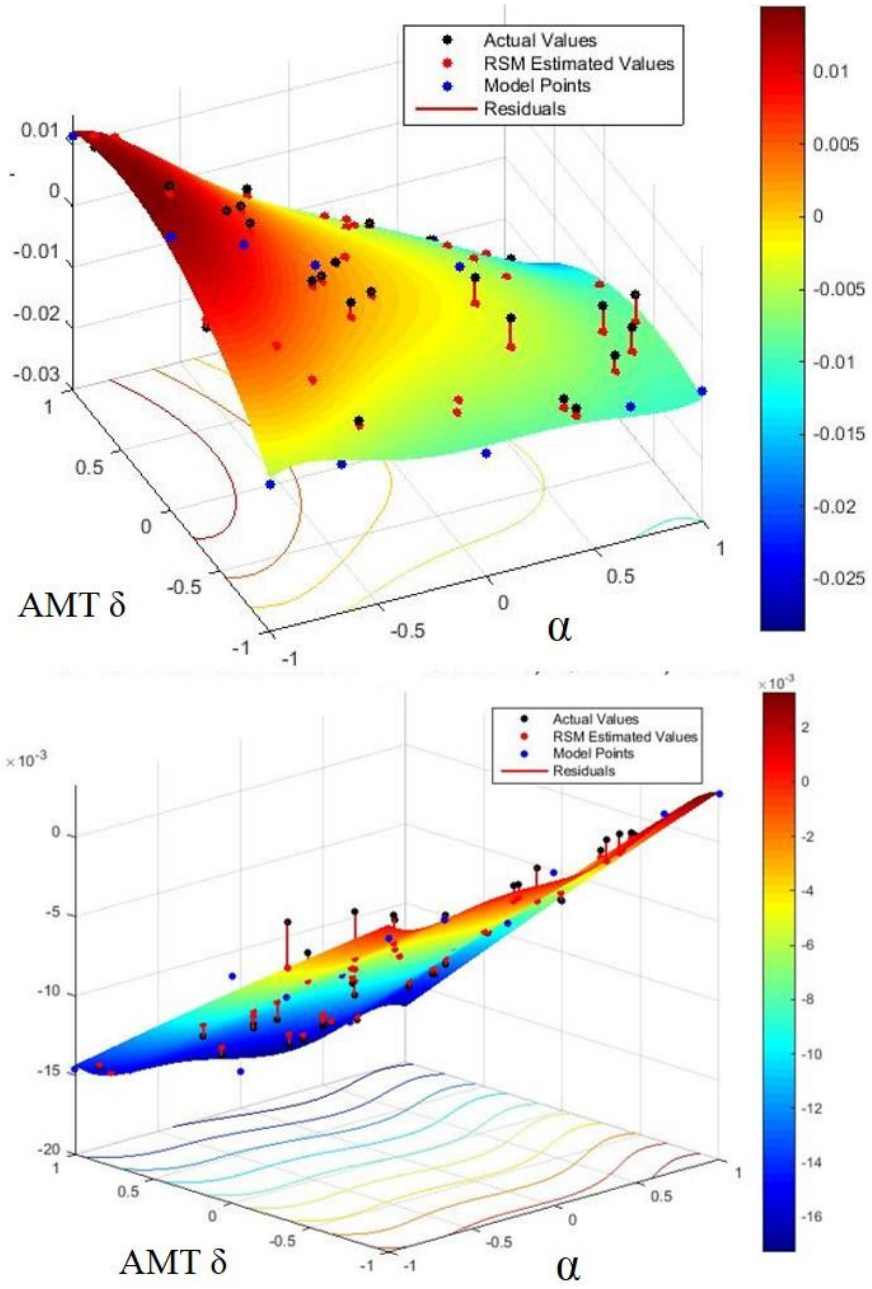


**Figure 6.12: 1st design RSMs, 4 WP & 20 SP, $C_l$ (top), $C_n$ (bottom).**

The $C_l$ and $C_n$ data provides more variation in AoA and AMT deflection than the $C_N$ and $C_m$ data, which can be seen in Figure 6.12. With increased variation, the AMT deflection as a continuous factor is not accurately captured. The lack of fit is reinforced with the residual plots in Figure 6.13 and in Figure 6.14.

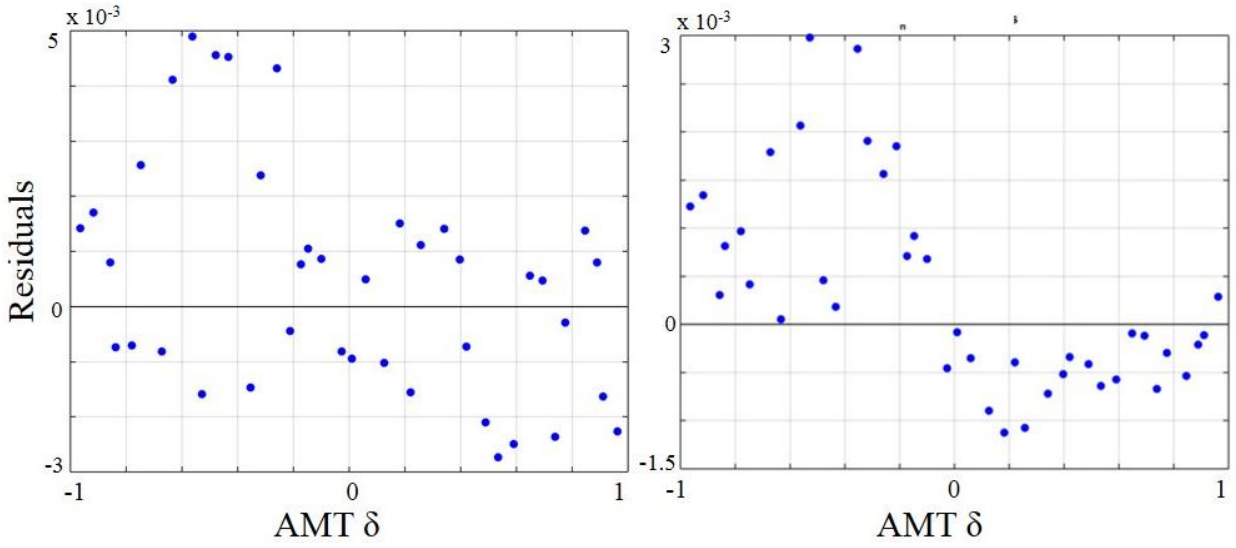


**Figure 6.13: 1st design $C_l$ (left) & $C_n$ (right) residuals v. AMT deflection angle.**

The RSM fit to this design was the same as the 2nd design for the $C_N$ and $C_m$ data, quadratic in the AMT deflection and quintic in AoA. There is a lack of fit for $C_n$ versus AMT deflection seen in the right plot of Figure 6.13. Therefore, AMT deflection must be discrete numeric of more than 3 levels rather than continuous.

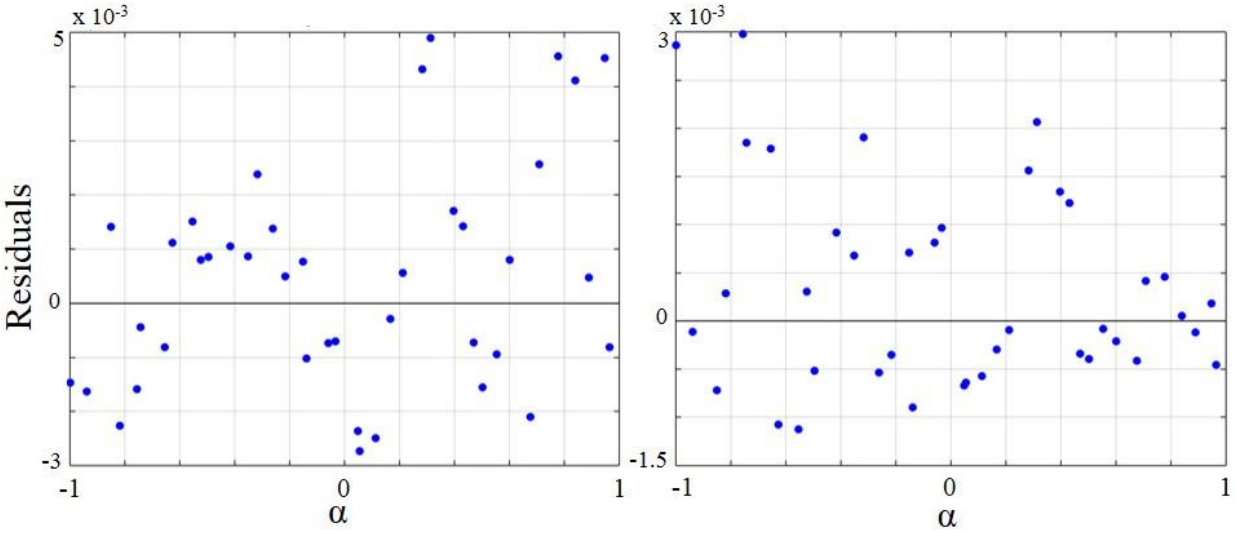


**Figure 6.14: 1st design $C_l$ (left) & $C_n$ (right) residuals v. AoA.**

The plots in Figure 6.14 of the $C_l$ and $C_n$ residuals versus AoA show there is good fit of the RSMs to this data when AoA is a 7 level discrete numeric factor. The next design changes the AMT deflection factor to discrete numeric of 5 levels.

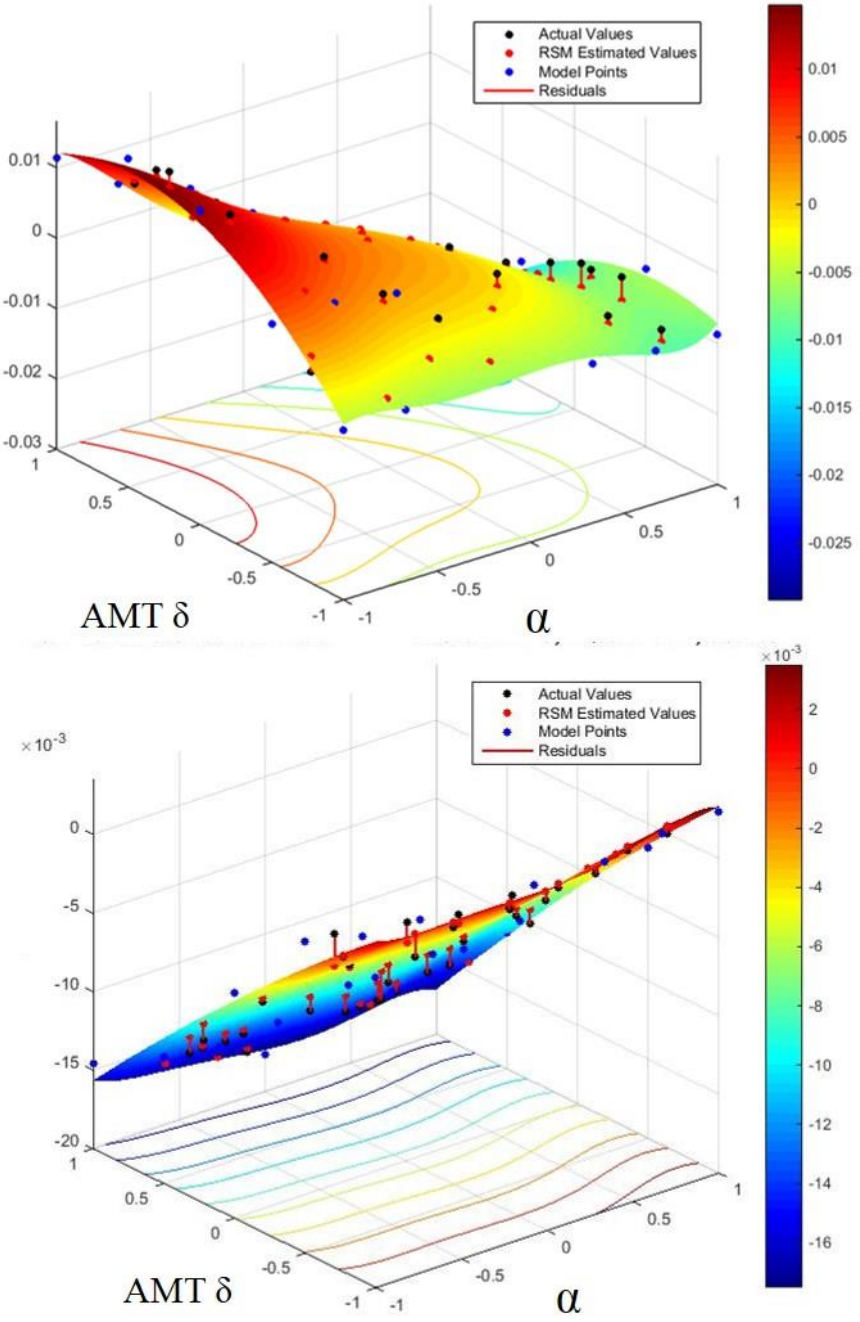


**Figure 6.15: 2nd design RSMs, 7 WP & 35 SP, $C_l$ (top), $C_n$ (bottom).**

The polynomial regression equation for the models above is the same as the 1st design. The difference with the 2nd design is the number of points in AMT deflection. There are now 7 WPs to account for the 5 levels of AMT deflection with extra WPs for replication.

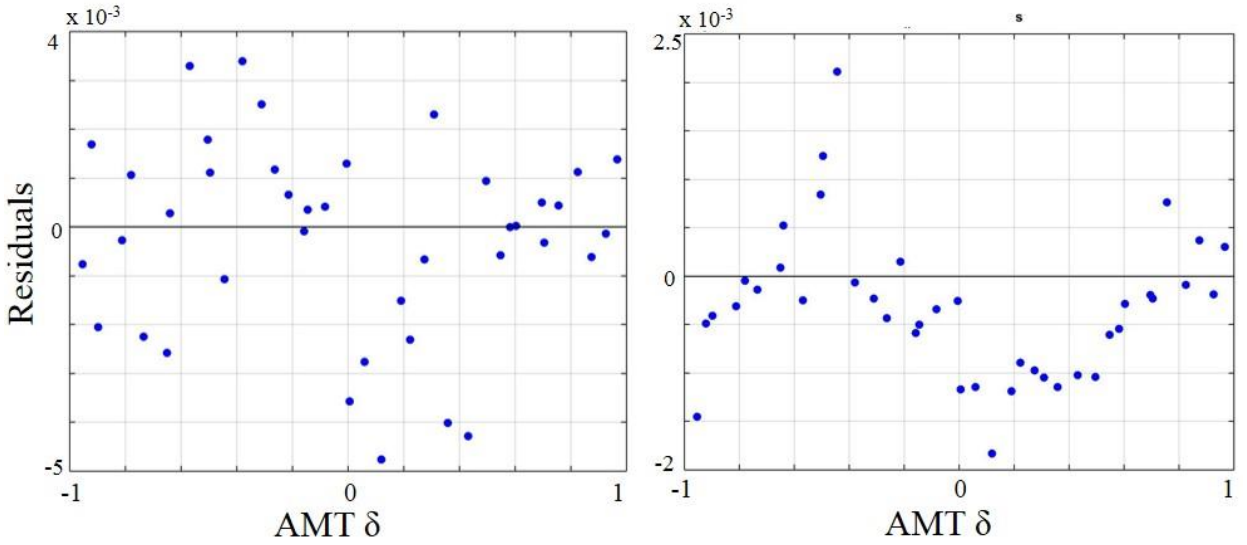


**Figure 6.16: 2nd design $C_l$ (left) & $C_n$ (right) residuals v. AMT deflection angle.**

The residuals decrease from the 1st design to the 2nd which is expected since the number of points in AMT deflection has been increased. There is still a lack of fit in the $C_n$ residuals versus AMT deflection angle. The number of AMT deflection levels was limited to 5 because the AMT deflection is a HTC factor and the number of levels should be minimized as much as possible. This rationale also guided Allison [1] to limit each parameter to 5 factor levels.

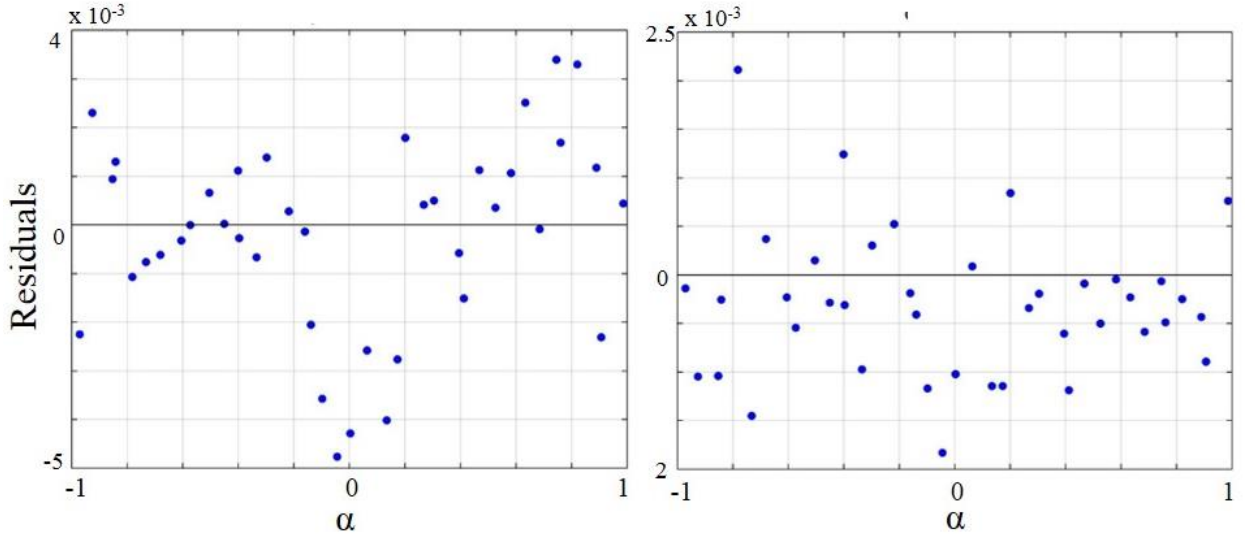


**Figure 6.17: 2nd design $C_l$ (left) & $C_n$ (right) residuals v. AoA.**

The 2nd design model fits the data well with respect to AoA which can be seen by the residuals in Figure 6.17. There is random scattering about an approximately zero mean. Another RSM is applied in Figure 6.18 to the same design in an attempt to improve the fit of $C_n$ with respect to AMT deflection.

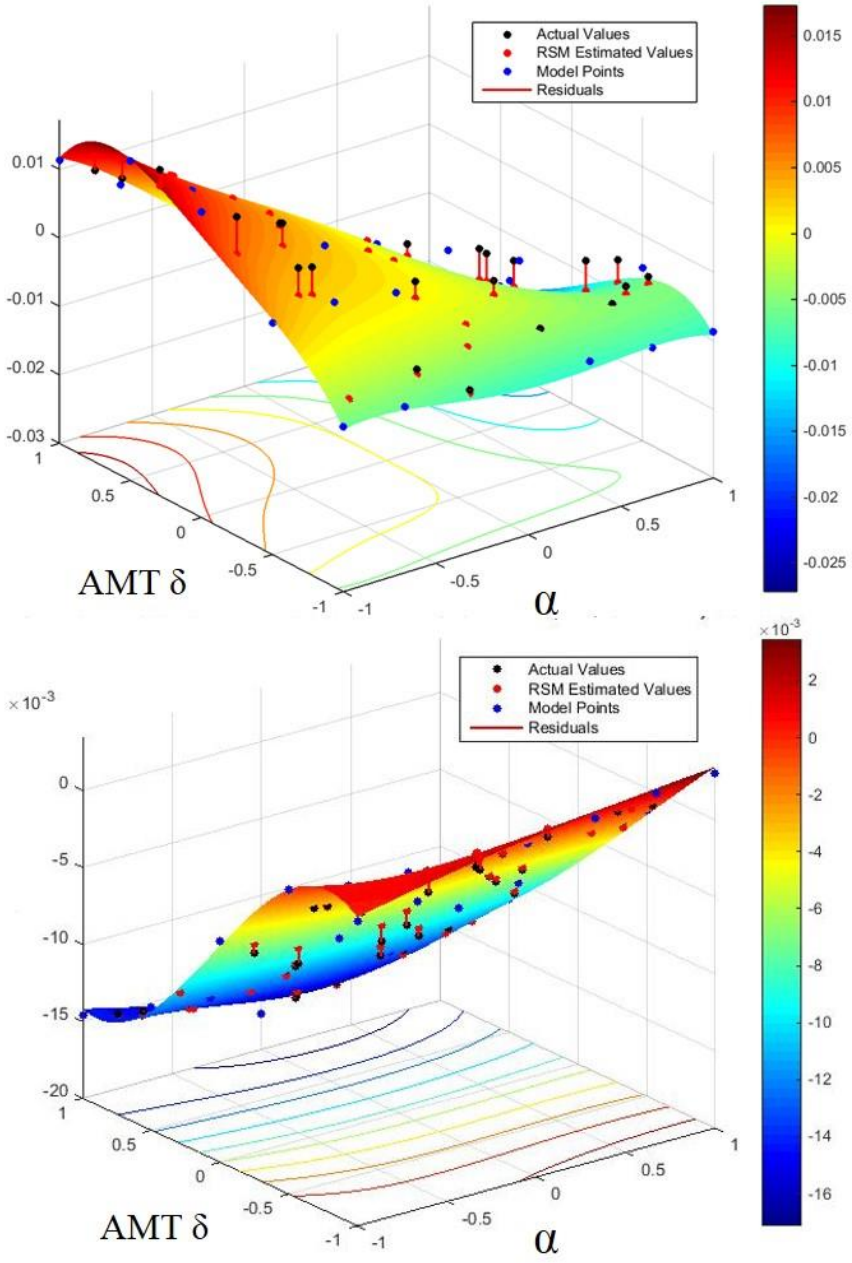


**Figure 6.18: 3rd design RSMs, 7 WP & 35 SP, $C_l$ (top), $C_n$ (bottom).**

The response surfaces in Figure 6.18 result from backward elimination starting from the maximum number of polynomial terms. The maximum power in AMT deflection is 3, and the maximum power in AoA is 5. Also, the initial maximum polynomial contains all interaction terms between the two factors. Terms that are not statistically significant are eliminated one at a time until all remaining polynomial terms are statistically significant. The significance is determined in JMP® Pro with t-tests performed on each term. The t-tests are a result of model creation in JMP® Pro. Therefore, the elimination of terms requires noting which value is least significant and then

repeating the model creation without that term. Note there some large residuals near the boundaries of the design space.

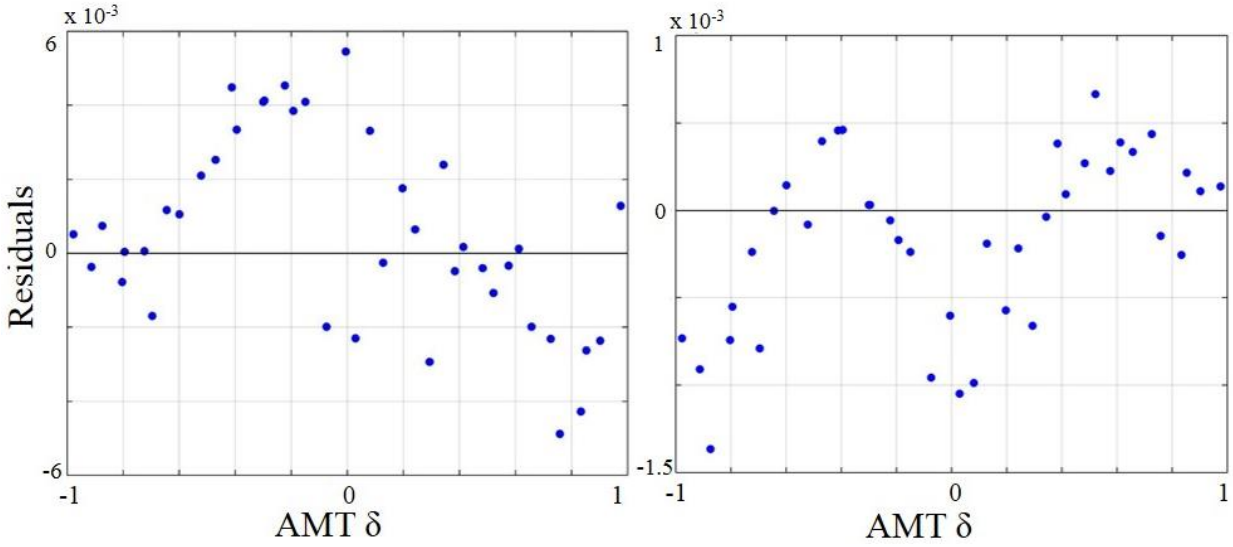


**Figure 6.19: 3rd design $C_l$ (left) & $C_n$ (right) residuals v. AMT deflection angle.**

The residuals in Figure 6.19 with respect to AMT deflection have increased in magnitude, which is confirmed by the NRMSE comparisons. The residuals with respect to AMT deflection still do not show random scattering indicating a lack of fit.

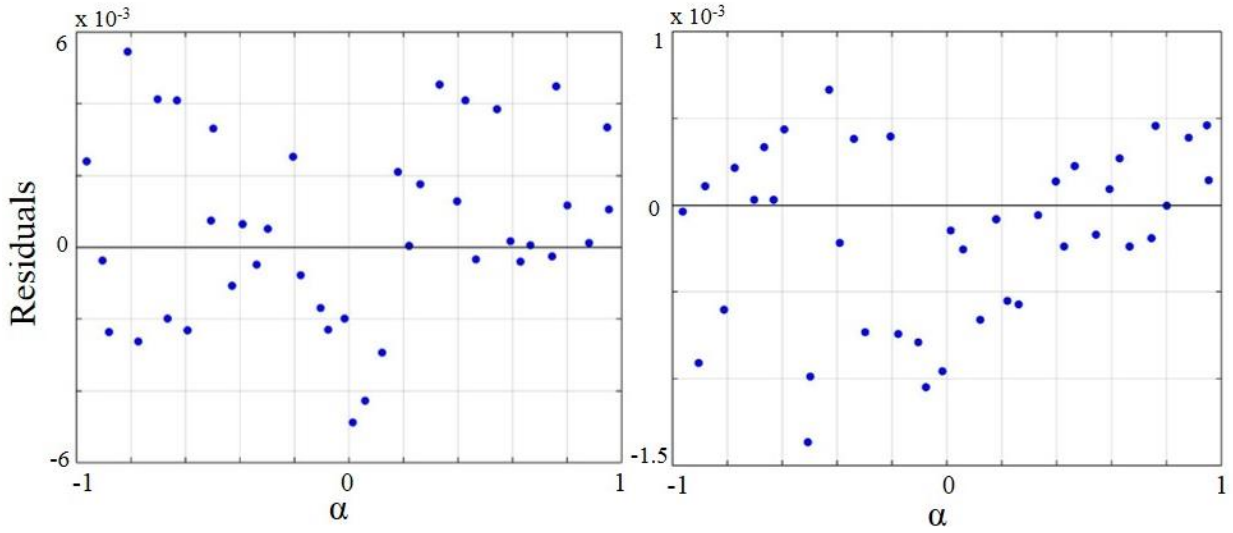


**Figure 6.20: 3rd design $C_l$ (left) & $C_n$ (right) residuals v. AoA.**

The scattering of residuals with respect to AoA is still randomly distributed about zero mean which indicates a good fit of the model for AoA. However, the residual values have once again increased when compared to the 2nd design of this data set. The increase in residuals is a

consequence of having a polynomial of too high a power for fitting the data. A data set can have a polynomial fit which has a power of one less than the number of values in the data set. However, there is often an issue with the fit becoming too extreme near the boundaries resulting in high residuals.

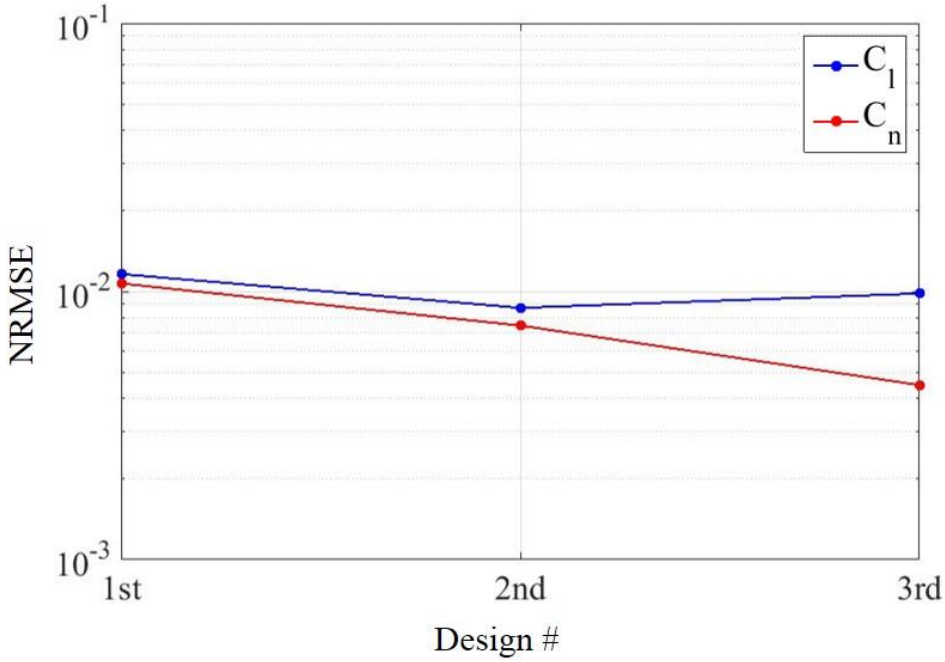


**Figure 6.21: NRMSE comparison of the three $C_l$ & $C_n$ designs.**

For $C_n$ there is an improvement in NRMSE from each design. This was also seen in the residual plots above because the fit for $C_n$ improved with each design. However, from the 2nd to 3rd design the NRMSE did not decrease for $C_l$. Due to a high power polynomial fit in the 3rd design, the residual at the right boundary was large resulting in a larger NRMSE than in the 2nd design.

| **Design #** | **1st** | **2nd** | **3rd** |
|---|---|---|---|
| **$\alpha$ (°)** | 24.6016 | 25.3229 | 22.3423 |
| **AMT $\delta$ (°)** | 15.8037 | 19.7154 | 18.2376 |
| **$\alpha^2 + \delta^2$** | 855.7 | 1029.9 | 831.8 |
| **$C_l$** | -0.0050 | -0.0050 | -0.0050 |
| **$C_n$** | -0.0050 | -0.0050 | -0.0050 |

**Table 6.2: $C_l$ & $C_n$ optimization results; Targets: $C_l \geq$ -0.005, $C_n$ = -0.005.**

Since the target constraints were not near the boundaries of the design space, the issues with the high power of the 3rd design do not largely affect in the optimum. The 1st design appears to have a low objective function value, but there is a lack of fit with this RSM to the true data so

the values resulting from this 1st design are not accurate. A discussion of the ICE 101 LMTAS AMT data results will take place in 6.3.

### 6.1.3 Three Factor $C_l$ & $C_n$ Data Results

The ICE 101 LMTAS AMT data problem is extended to three factors, AMT size (HTC), AMT deflection angle (HTC), and AoA (ETC), and is introduced in Section 4.3. Now that the $C_l$ and $C_n$ responses with respect to the three factors are four dimensional, the results cannot be visualized as before. However, by holding one of the factors constant, the responses can be viewed in a three-dimensional space. This extends to a greater number of factors as well; all factors except two can be held constant to view the responses over the range of two variable factors and n-2 constant factors, where n is the number of factors.

The interpolation scheme was modified to access each of the AMT size (small, medium, and large) data sets depending on each design point. Once an AMT size data set was selected, the interpolation scheme operated as before. Furthermore, the RSMs fit were generated by using backwards elimination starting with a 3rd order polynomials with all interaction effects. Figure 6.22 shows three variable RSMs with different factors held constant. A GUI was created to change the constants to see how the RSMs vary with all factors. Furthermore, an optimization was performed on this data set. Only minor changes were made to the objective function of the optimization problem to increase from two to three factors. The results of the optimization are shown in Table 6.3. Furthermore, to determine an optimum AMT size, two factors, chord and span, would have to be added instead of just optimizing for area. The AMT size result compares to an area which is close to the large AMT (coded = 1, natural = 2.57 $in^2$). The optimization results should not be directly compared to the two factor analysis due to the addition of the third factor.

| **Design** | **Three Factor** |
|---|---|
| $\boldsymbol{\alpha}$ **(°)** | 28.0182 |
| **AMT** $\boldsymbol{\delta}$ **(°)** | 20.8619 |
| **AMT size (coded, natural [in$^2$])** | 0.6071, 2.3205 |
| $\boldsymbol{\alpha^2 + \delta^2}$ | 1220.6 |
| $\boldsymbol{C_l}$ | -0.0050 |
| $\boldsymbol{C_n}$ | -0.0050 |

**Table 6.3: Three factor optimization results ; Targets: $C_l \geq -0.005$, $C_n = -0.005$.**

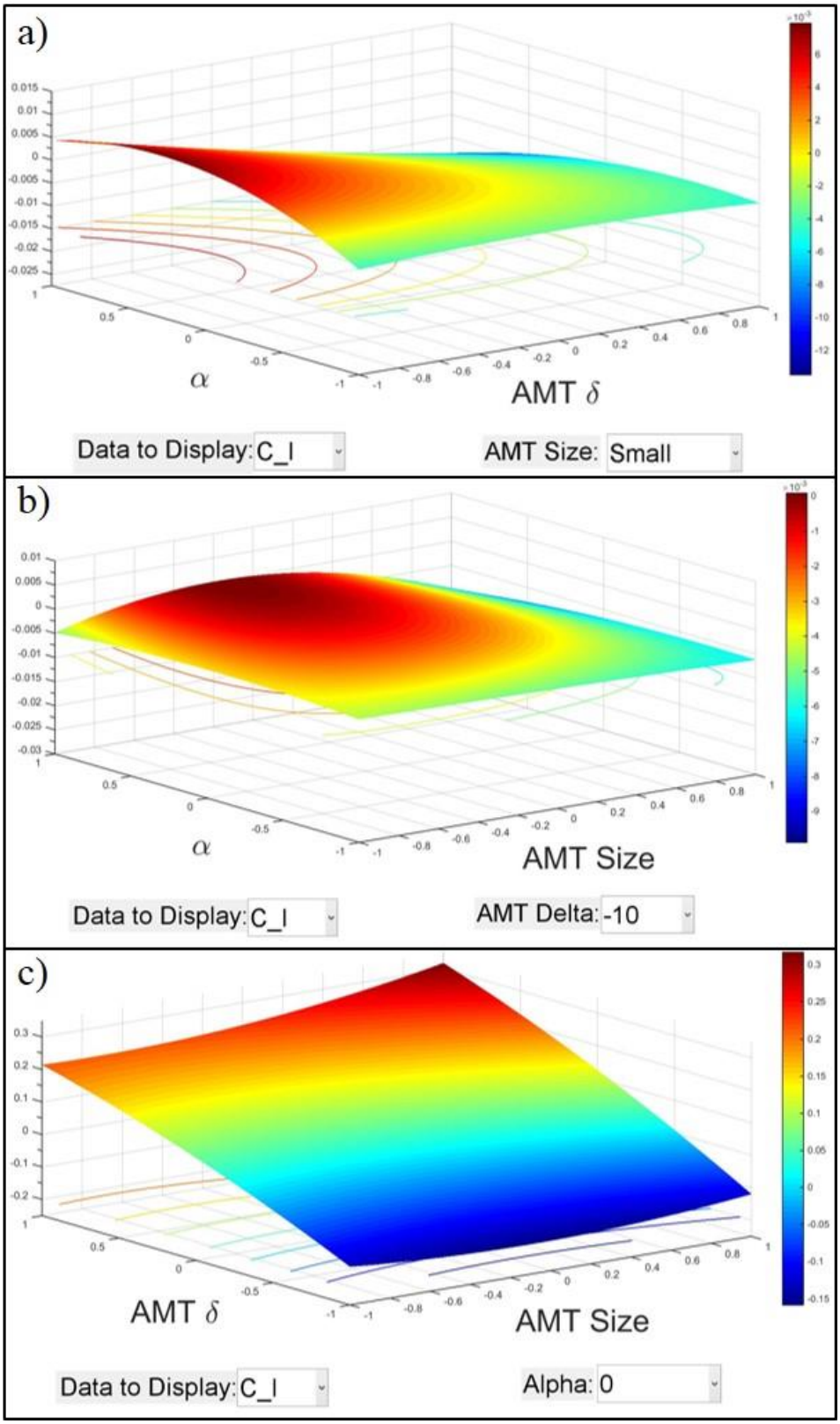


**Figure 6.22: Three factor ICE 101 LMTAS data analysis, a) constant AMT size, b) constant AMT deflection, c) constant AoA.**

## 6.2 NACA 0012

The results of the ICE 101 LMTAS AMT data analysis drive the split-plot design for the NACA 0012 WT testing. A split-plot design with 7 WPs and 35 total runs is used for NACA 0012 WT testing. The WP factor is the flap deflection angle and the SP factor is AoA. Even though there are 7 WPs in the design, the flap deflection angle has only 5 levels; two of the WPs are replications for error variance determination. Therefore, NACA 0012 0.2c flaps were printed at 5 deflection angles: 0, 5, 10, 15, and 20 degrees. For each WP, the corresponding flap is placed on the NACA 0012 main body. Then, the strain gage balance is recalibrated, and data is gathered at the prescribed AoA sequence with ETC resetting between each point. The order of testing is shown in Table A.7.

Previously determined experimental data for a NACA 0012 airfoil with plain flap at deflection angles of 0, 5, 10, 15, and 20 degrees could not be located, so an empirical increment from Thin Airfoil Theory was derived for comparison of Open-Jet WT data. Young [96] gives a derivation for the lift coefficient increments, $\Delta C_L$, for various flap types. The increment for a plain flap is given as

$$\Delta C_L = C_{L_\alpha} \lambda_1 \left(\frac{c_f}{c}\right) \delta \,, \tag{6.1}$$

where $C_{L_\alpha}$ is the lift curve slope of a NACA 0012 airfoil, $c_f$ is the flap chord, $\lambda_1 \left(\frac{c_f}{c}\right)$ is a constant value determined from Figure 6.23 at a specific percent chord flap, and $\delta$ is the flap angle (rad).

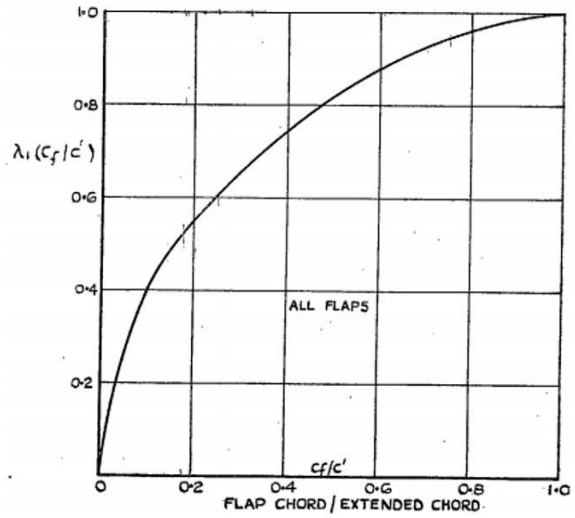


**Figure 6.23: $\lambda_1$ value for $\Delta C_L$ calculation. Young, A. D., ARC, "The Aerodynamic Characteristics of Flaps." London, England. 1947. Report Number: RAE-TM-AERO-2185. Used under fair use, 2015.**

The lift curve slope for the NACA 0012 airfoil in the Open-Jet WT at a Reynolds Number of 0.23 x $10^6$, is approximately 5.897 which is close to $2\pi$, a standard value for 2D symmetric airfoils. Also, the $\lambda_1$ for a NACA 0012 airfoil with plain flap of 0.2c is approximately 0.55.

The $\Delta C_m$ increment is derived from Ames and Sears [97]. Since the airfoil in this problem is symmetric, the equation presented by Ames and Sears for a pitching moment flap increment becomes

$$\Delta C_m = C_{m_\delta} \delta \,, \tag{6.2}$$

where $C_{m_\delta}$ is the change in pitching moment coefficient with respect to change in flap deflection angle and $\delta$ is the flap deflection angle in degrees. $C_{m_\delta}$ was estimated to be -0.004 from NACA 0012 data in "Theory of Wing Sections" [98]. The lift coefficient and pitching moment coefficient results with empirical increments for comparison are shown in Figure 6.24 and in Figure 6.25. The historical data used is a NACA 0012 airfoil at Reynolds Numbers of 170,000 and 330,000 [92]. The baseline used for the empirical increment was the average of those two data sets since the Reynolds Number for this testing falls between the two values.

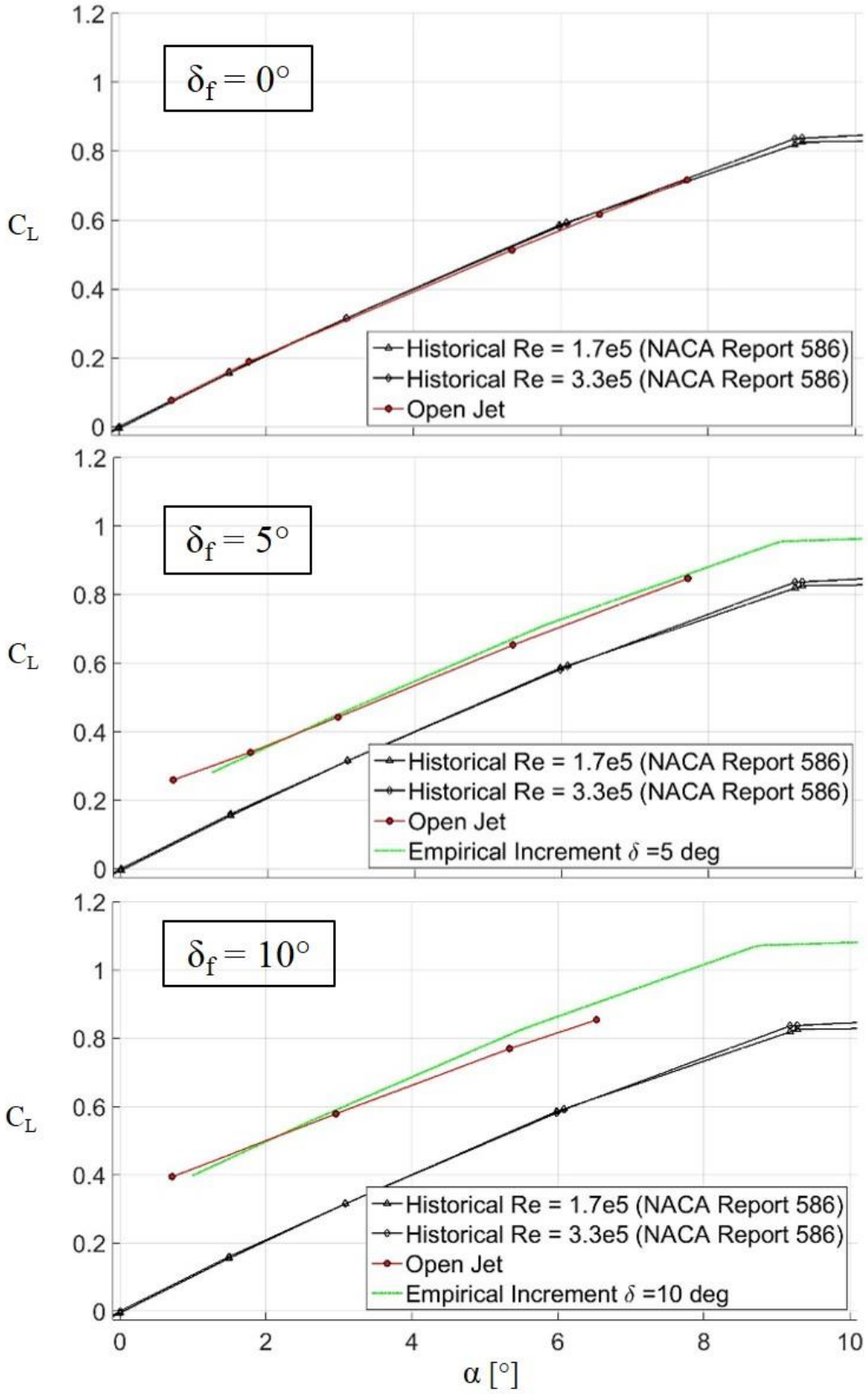


**Figure 6.24: NACA 0012 $C_L$ data with empirical increment.**

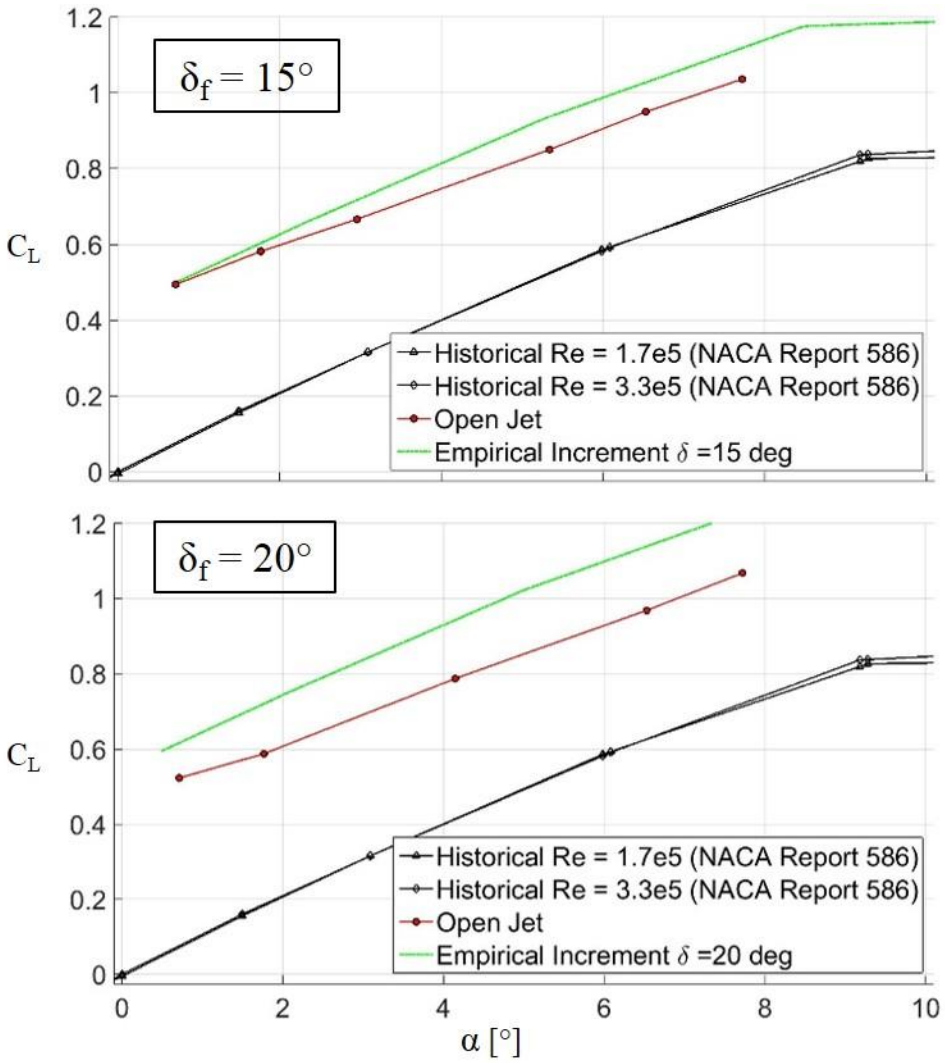


**Figure 6.24 continued: NACA 0012 $C_L$ data with empirical increment.**

Descriptions of the corrections applied to the raw Open-Jet WT data can be found in Appendix B. Flap deflections of 0, 5, and 10 degrees match well with the empirical increment in the 1 to 9 degree range of AoA. Flap deflections of above 10 degrees are not comparable to the empirical increment due to the flow at these conditions being deflected out of the open test section. Even though the Open-Jet data for these flap deflections is not accurate, the data is still useful for testing WT data incorporation into the SBO strategy.

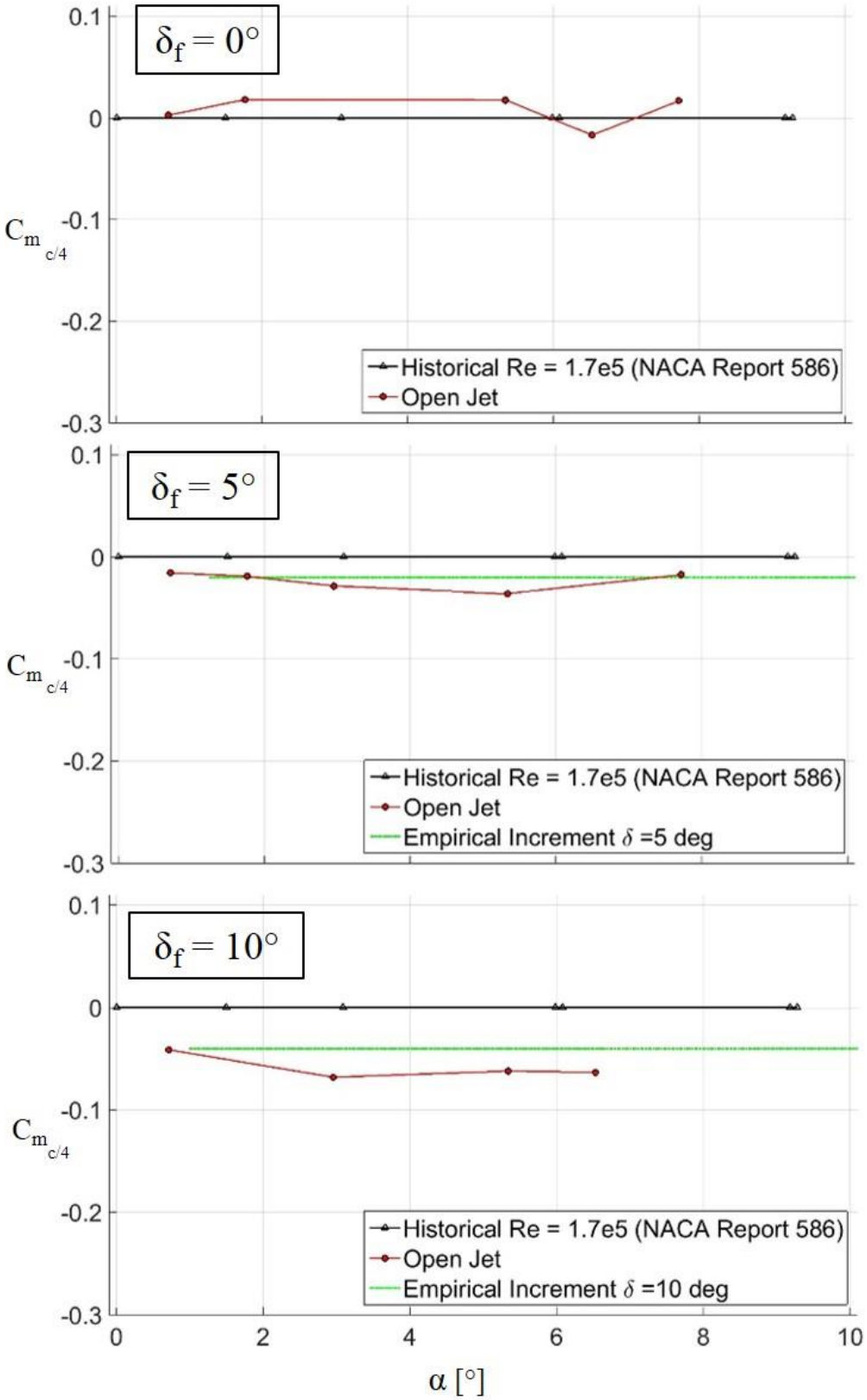


**Figure 6.25: NACA 0012 $C_m$ data with empirical increment.**

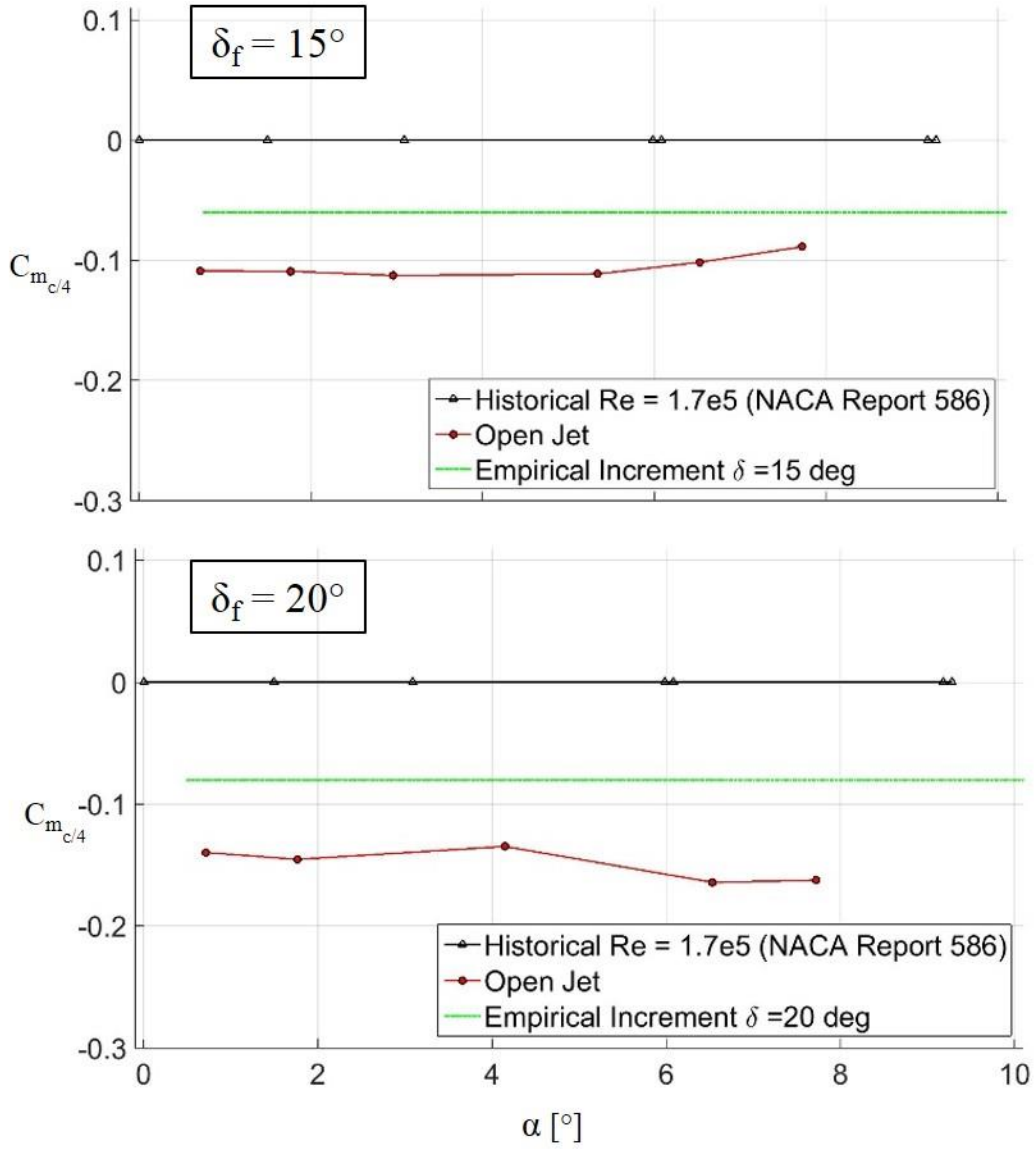


**Figure 6.25 continued: NACA 0012 $C_m$ data with empirical increment.**

The differences in the Open-Jet data and the empirical increment in Figure 6.25 are due to the lack of knowledge of the drag due to the strut balance and the uncertainties in the mounting arrangement. As with the lift coefficient, even though the pitching moment coefficient data does not compare well with the empirical increments, the data is still useful for implementation in the WT SBO strategy.

### 6.2.1 Response Surface Models

The RSM results from Open-Jet WT testing of an AM NACA 0012 model is given in this section. Three different RSMs are applied to the NACA 0012 WT data: quadratic polynomial, cubic/quintic

polynomial, and artificial neural network models. The first RSM applied is a quadratic model with two-factor interactions. The second RSM applied is a polynomial to the 3rd power in flap deflection angle and to the 5th power in AoA with two-factor interactions to the first power as with the quadratic model. The third RSM applied is the neural network model in JMP® Pro, which is a combination of three tangent functions. For each of the models, the Open-Jet data points are plotted on the surface for NRMSE determination. Furthermore, the empirical increment data points are plotted for comparison to the Open-Jet data. After each of the models is introduced, the NRMSE for each model is analyzed.

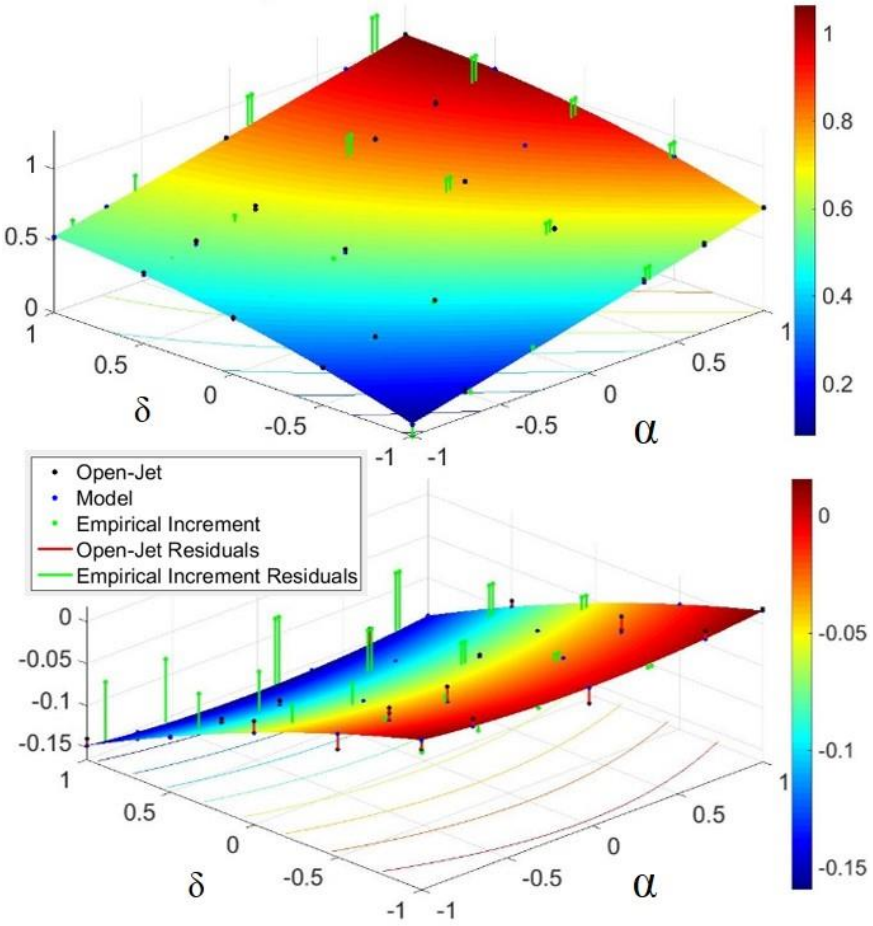


**Figure 6.26: NACA 0012 Open-Jet WT Quadratic RSMs: $C_L$ (top), $C_{mc/4}$ (bottom).**

The two RSMs in Figure 6.26 are quadratic regression fits to the Open-Jet lift coefficient and pitching moment coefficient data versus AoA and flap deflection angle. The black points are the actual Open-Jet data points from the split-plot design, and the blue points are the force and moment values on the RSM corresponding the split-plot design AoA and deflection angle. The differences in the black and blue points are difficult to see in the $C_L$ plot due to the data being

mostly linear, which an RSM fits with accuracy. The black and blue points are used for determination of the NRMSE. This NRMSE is used for comparison of the different RSMs. The green points are the empirical increment data points generated from baseline NACA 0012 historical data. These points are used to compute other NRMSE values for comparison of the Open-Jet data to the empirical increment data. The differences between the Open-Jet data and empirical increment become large at the 15° and 20° flap deflections for $C_L$ which are attributed to the flow being deflected out of the open test section. Also, the Open-Jet and empirical increment differences are large for $C_m$ due to the open test section, difficulties estimating drag due to the strut balance, and the resolution of the balance for pitching moment.

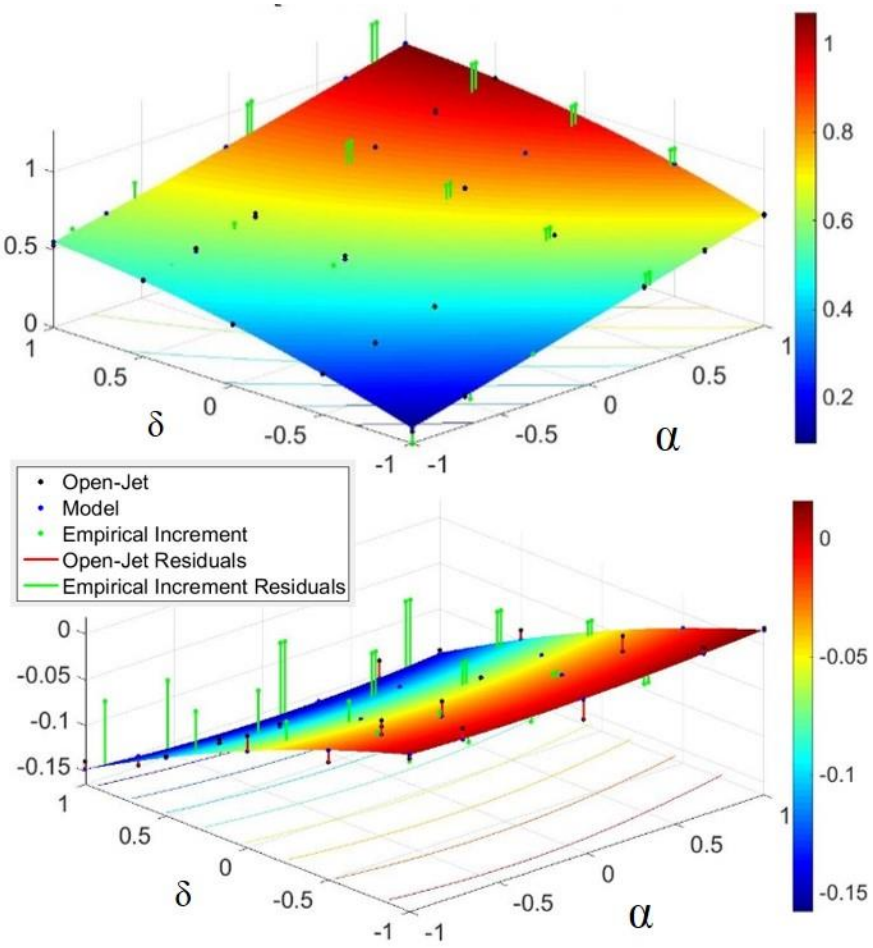


**Figure 6.27: NACA 0012 Open-Jet WT Cubic/Quintic RSMs: $C_L$ (top), $C_{mc/4}$ (bottom).**

Next, a higher-order polynomial RSM was applied to the Open-Jet data. The RSMs in Figure 6.27 are polynomials to the 3rd power in flap deflection and to the 5th power in AoA with 1st order two factor interaction effects. The order of the polynomial was increased to fit the

variation in $C_m$ better. However, the $C_m$ has large variation from the various issues previously discussed with acquiring pitching moment data in the Open-Jet WT with the strut balance. As with the quadratic RSMs, two different residuals are defined for computation of NRMSE. The empirical increment residuals for $C_m$ appear to have decreased for this model. A quantitative measure of this is given in the NRMSE figures below.

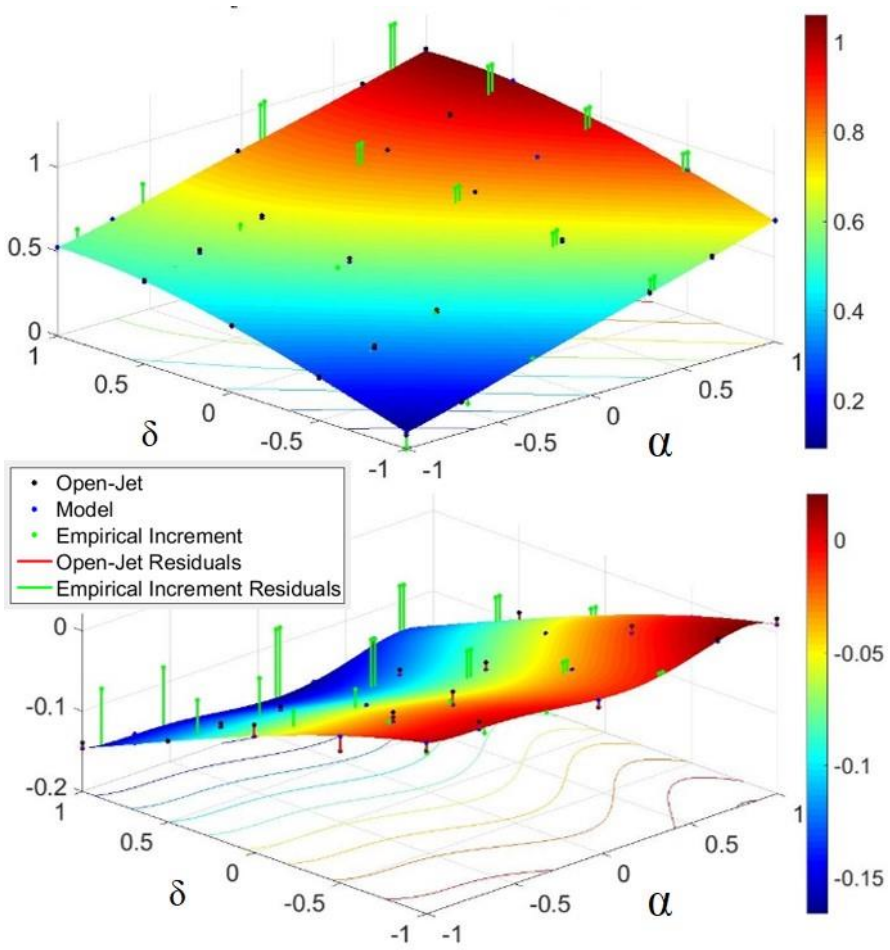


**Figure 6.28: NACA 0012 Open-Jet WT Neural Network RSMs: $C_L$ (top), $C_{mc/4}$ (bottom).**

The third RSM applied to the NACA 0012 Open-Jet WT data is a neural network model computed with JMP® Pro. The neural model is composed of three tangent functions; the tool to create the model does have the capability to add linear terms, but for simplicity just the three tangent functions are applied. From visual inspection of the neural RSMs, the models appear to have similar shape to the quadratic RSMs in Figure 6.26.

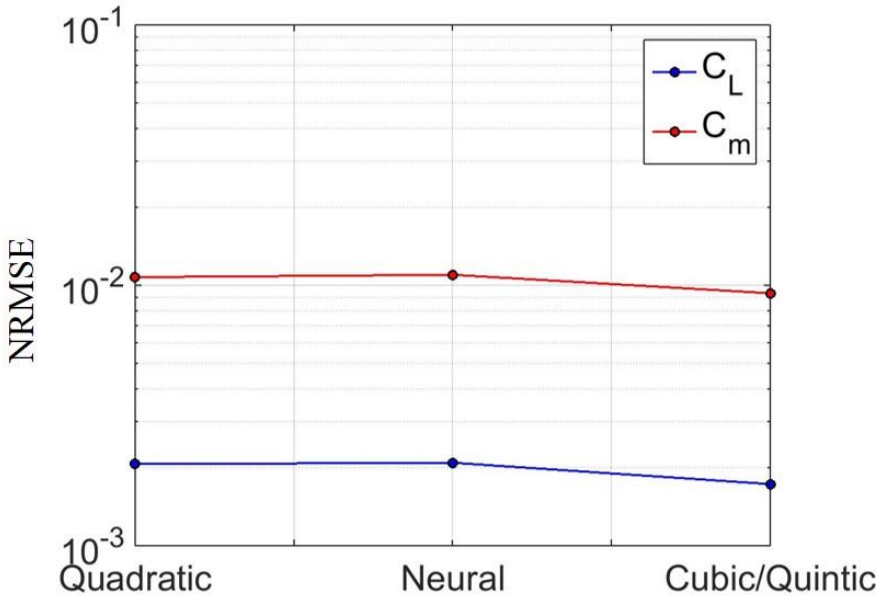


**Figure 6.29: NRMSE for RSM type comparison.**

The first NRMSE plot, Figure 6.29, is generated from the Open-Jet data points and data points on each of the RSMs, corresponding to the black and blue points in Figure 6.26 through Figure 6.28. The NRMSE was computed for each of the points in the design space. These residual values are a measure of how well a RSM fit the Open-Jet data; therefore, the NRMSEs determine which of the 3 models best fit the data. The cubic/quintic RSM has the smallest NRMSE, and thus is the best fit to the Open-Jet data for the split-plot design tested. The $C_m$ Open-Jet data was nonlinear due to challenges in the data acquisition, and this nonlinearity results in a higher-order polynomial being a better fit to the data. If the $C_m$ data were mostly linear as Thin Airfoil Theory about the quarter chord would suggest, a linear model would be suitable for fitting the $C_m$ data. However, a quadratic model would still need to be applied for $C_L$ if the design space extended into the stall region of the airfoil. The neural model has a comparable NRMSE to that of the quadratic model. Furthermore, the residuals were normalized by the maximum value in the Open-Jet data for $C_L$ and $C_m$ which enables the NRMSE $C_L$ and NRMSE $C_m$ plots to be compared. As expected, the $C_m$ NRMSE is larger due to the multiple issues presented with the pitching moment data acquisition.

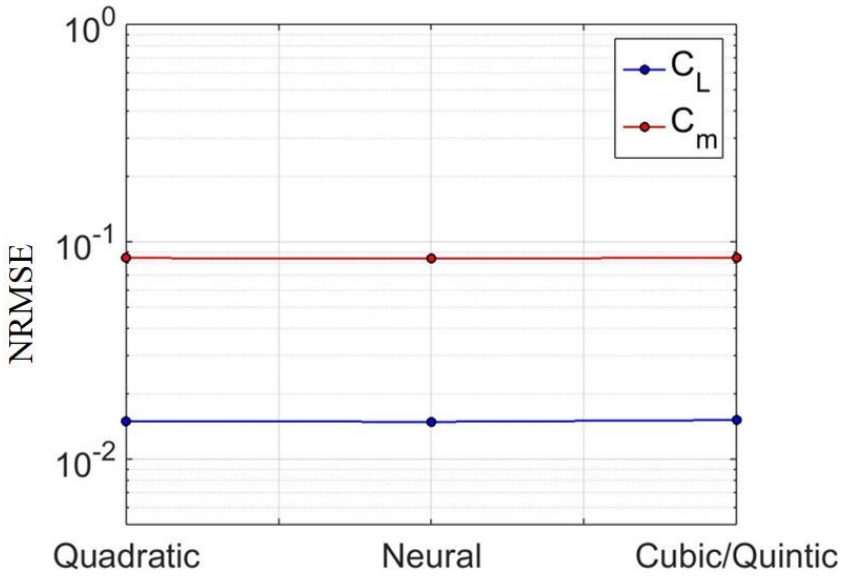


**Figure 6.30: NRMSE for Open-Jet data and empirical increment data comparison.**

The second NRMSE plot, Figure 6.30, is presented for comparison of the Open-Jet RSM model data to the empirical increment data. The green points in the RSMs above are used for computation of empirical increment residuals. $C_L$ and $C_m$ data was generated on the RSMs at each of the AoA and flap deflection points of the empirical increment data. The residuals were then used for NRMSE computation. The residuals in this case were normalized by the maximum $C_L$ and $C_m$ values of the empirical increment data. The NRMSE of $C_m$ is much larger than the NRMSE of $C_L$ due to $C_m$ data acquisition issues.

Three different RSMs were applied above to the Open-Jet WT data from an AM NACA 0012 model with a plain flap. An empirical increment, derived from Thin Airfoil Theory, was included for comparison to the Open-Jet data. The $C_L$ data of the Open-Jet compares well with the empirical increment. The $C_m$ data has large differences when compared to the empirical increment. For an airfoil, pitching moment about the quarter-chord should be independent of AoA resulting in a horizontal line. However, the Open-Jet data was not smooth, but the mean slope of the $C_m$ data is approximately 0. Moreover, the error in the $C_m$ Open-Jet data results from difficulties estimating drag due to the strut balance and deflection of the flow out of the test section at higher flap deflection angles.

For a more complicated design space of more levels, a process will need to be developed for determining how many data points are need in a split-plot design for an accurate RSM. Even

though the higher-order polynomial model above successfully decreased the NRMSE for the Open-Jet data, caution is advised when applying a higher-order fit to data. As the order of a polynomial increases, the residuals at the extremities of a data set can grow resulting in a fit which does not improve from a lower order fit. Results from performing gradient-based constraint optimization using the RSMs above are presented in the next section.

### 6.2.2 Optimization Results

Results of the constraint optimization problem adapted from Snyder are given in Table 6.4. Furthermore, another optimization is performed but with the $C_L$ and $C_m$ constraints both being equality constraints.

| RSM Type | Quadratic | Cubic ($\delta$)/Quintic ($\alpha$) | Neural | Quadratic Empirical Increments |
|---|---|---|---|---|
| $\alpha$ (°) | 4.22 | 4.06 | 4.22 | 5.47 |
| $\delta$ (°) | 10.87 | 11.66 | 10.57 | 19.50 |
| $\alpha^2 + \delta^2$ | 136.09 | 152.48 | 129.69 | 410.21 |
| $C_L$ | 0.6897 | 0.6977 | 0.6839 | 1.06 |
| $C_m$ | -0.0600 | -0.0600 | -0.0600 | -0.060 |

**Table 6.4: NACA 0012 WT optimization results; Targets: $C_L \geq 0.6$, $C_m = -0.06$.**

The three RSMs of the Open-Jet WT data are fairly consistent in their optimum AoA and flap deflection angle. Some variation in the optimum results are expected due to different RSMs applied to the data. An optimum was also determined from a quadratic RSM of empirical increment data. The same target conditions are applied as constraints for this data set. However, the optimum AoA and flap angle deflection differs from the other RSMs because of Open-Jet $C_m$ error.

| RSM Type | Quadratic | Cubic ($\delta$)/Quintic ($\alpha$) | Neural | Quadratic Empirical Increments |
|---|---|---|---|---|
| $\alpha$ (°) | 3.16 | 3.12 | 3.21 | 0.67 |
| $\delta$ (°) | 10.76 | 10.73 | 10.56 | 19.50 |
| $\alpha^2 + \delta^2$ | 125.82 | 124.90 | 121.80 | 380.70 |
| $C_L$ | 0.6000 | 0.6000 | 0.6000 | 0.6000 |
| $C_m$ | -0.0600 | -0.0600 | -0.0600 | -0.0600 |

**Table 6.5: Two equality optimization results; Targets: $C_L = 0.6$, $C_m = -0.06$.**

The second optimization problem performed has the constraint conditions as equalities rather than $C_L$ being an inequality condition. This change was made for a better comparison of the

three RSMs. When the $C_L$ condition was an inequality, the optimum AoA and flap deflection angles could result in a $C_L$ of much larger than the minimum 0.60. The empirical increment $C_L$ for the first optimization problem was even over 1.0. By forcing the optimizer to obtain an optimum at the target conditions, differences in optimum due to RSM differences can be shown. The results from the three RSMs are now even closer than in the first optimization problem which indicates the models selected are comparable in their ability to fit the NACA 0012 Open-Jet WT data. Due to challenges in acquiring accurate $C_m$ data from the Open-Jet WT, a direct comparison of the optimum to the empirical increment or high-fidelity CFD data cannot be made.

## 6.3 WT SBO Strategy Effectiveness

An equation of effectiveness and a definition of each factor is given by Equation 1.1 and given in Section 1.3, respectively. The effectiveness of the WT SBO strategy is evaluated in this section. The problems for effectiveness evaluation are the ICE 101 LMTAS data analysis, Sections 4.2 and 6.1, as well as the NACA 0012 Open-Jet WT testing, Sections 4.4 and 6.2. The effectiveness of the WT SBO strategy is broken down into two parts, the quality of the data from strategy and the time and cost to produce the data. The quality is addressed in Section 6.3.1 below by discussing the data quality from the Open-Jet WT, the accuracy of the RSMs, and the ability of the split-plot design to fit the data. Next, the acceptance is addressed in Section 6.3.2 by a discussion of the cost and time of the SBO strategy, which includes WT model production, testing, and RSM construction.

### 6.3.1 Quality Factors of WT SBO Strategy

ICE 101 LMTAS data with AMT control surface deflections was used in the WT SBO strategy first to test the viability of the split-plot designs developed for WT testing. Determining the quality of the output from an SBO requires examination of the RSMs generated from WT data. The quality of a RSM is dependent on the WT testing, and the quality of the WT data is in part due to the DoE design generated for the testing. Therefore, an inspection of WT SBO strategy quality must first look at the experimental design for WT testing. A split-plot design was decided upon for this work due to the need to shut down the tunnel to replace control surfaces rather than increased complexity with mechanically actuated control surfaces.

The ICE 101 LMTAS data was used to determine the number of levels needed for WT testing. This was an important metric to have prior to model creation because the different NACA 0012 flaps needed to be printed all at the same time. For testing of a full aircraft configuration, many of the control surfaces will be much smaller than the flaps for a 21" span NACA 0012 airfoil. Since the flaps are so large, the number of flaps need to be known prior to testing due to the amount of time to print each flap. The LMTAS data analysis began with normal force and pitching moment coefficient data with varying AMT flap deflections for AoA sweeps. Setting the AoA factor to continuous was not effective for accurately capturing the data, which resulted in changing the AoA factor to discrete numeric of 7 levels. Since there was not much variation in the AMT deflection angle data, the next data set investigated was the roll and yaw moment coefficient data. From this analysis, the AMT deflection angle factor was changed from continuous to discrete numeric of 5 levels. When this process is applied to a new aircraft configuration with no prior data, there will need to be some method for determining how many levels are needed for a certain factor. The ETC factors can have a large number of factors without much of a cost or time penalty, but attempts should be made to limit the number of HTC factor levels. The results of 7 levels for ETC factors and 5 levels for HTC factors can be used as a starting split-plot design for a new aircraft configuration, but there must be some way to analyze whether the design space is captured by the split-plot design. This may be accomplish by low- or medium- fidelity CFD analysis. Even though the low-fidelity CFD analysis may not be suitable for design optimization, it may help determine how the design space should be partitioned for a split-plot experimental design.

A challenge faced in this work was the quality of data resulting from the Open-Jet WT. Due to the open test section, there is a limited AoA range that can be tested where the data is of any quality, roughly -10 to 10 degrees. Furthermore, the strut balance used had significant interference effect on the model drag, which could not be determined completely using methods described in Barlow *et al* [99], resulting in inaccurate pitching moment data. WT testing in a closed test section with a sting balance should aid in acquisition of higher quality data.

Another challenge faced in this work is how to determine the best RSM to fit the WT data. This is a problem with any SBO strategy that uses a limited number of points for RSM generation. The initial surface used was a simple quadratic polynomial regression. The power of the polynomial model was increased in an attempt to improve the NRMSE; however, there are consequences to increasing a polynomial fit to higher powers. Near the design space limits high

errors can often be seen where a polynomial of high power overestimated the data. This was seen from the transition of the 2nd to the 3rd design of roll and yaw moment data analysis.

The quality of data from the Open-Jet results in a process that is not fully effective. The NACA 0012 $C_L$ data did compare well to empirical increments of 0, 5, and 10 degree flap deflections. However, the $C_m$ WT data only compared well to the empirical increments for flap deflections of 0 and 5 degrees. Furthermore, the $C_m$ data was noisy, which results in the RSMs attempting to fit the increased curvature of the data. Once the quality of WT data is resolved, the WT SBO strategy can be effective. Additional processes for determination of number of needed levels in the split-plot design and for selection of RSM type will further increase the quality of results from the WT SBO strategy.

### 6.3.2 Acceptance Factors of WT SBO Strategy

The acceptance factors of the WT SBO strategy depend on the cost and time to produce the WT model, to test the WT model, and to process the resulting data into an RSM for optimization. The cost and time to produce a WT model with AM is addressed in Section 5.5.2. A split-plot DoE design reduces the time, and thus cost for WT testing when compared to OFAT testing or compared to a completely randomized DoE. A completely randomized DoE, all factors treated the same when considering changing their value, would considerably decrease the number of points to test in a WT from OFAT testing. However, WT testing of control surfaces is a design space with split-plot structure if the control surfaces are not mechanically actuated. Changing control surface deflections requires stopping the flow in the WT, which is a detailed process taking more time than modifying AoA during testing. Furthermore, mechanically actuated parts increase the complexity of a model design. For these reasons, a split-plot design is suitable for a WT testing design space when considering cost and time to produce and test a model. WT testing cost and time could be reduced by incorporating mechanically or electrically actuated control surfaces, but this does add complexity to the model and control surface design.

Another comparison to be drawn for the WT SBO strategy is to a SBO strategy using CFD analysis for data generation. According to Aeronautical Testing Service (ATS), Inc., the major differences between cost of WT testing and CFD analysis is the cost per data point and the initial

cost. CFD analysis has a low initial cost when compared to the cost of WT model construction; however, the cost per data point of CFD analysis is high when compared to that of WT testing [8].

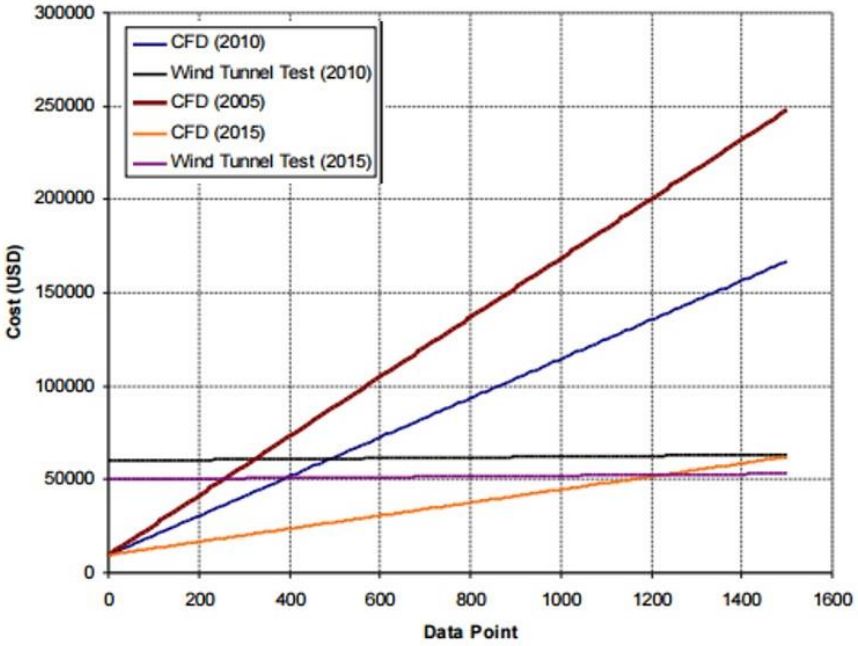


**Figure 6.31: Estimated cost for WT and CFD data based on ATS experience and computer hardware availability. (April 5, 2015) Leighton, T. "CFD and Wind Tunnel Testing: Complimentary Methods for Aircraft Design." Aeronautical Testing Service, Inc., 2014. Available: http://www.cd-adapco.com/sites/default/files/Presentation/Todd_Leighton.pdf. Used under fair use, 2015.**

Figure 6.31 compares cost of CFD analysis and WT testing. The data is based on ATS experience and projections to 2015, as the study was conducted in 2010. Also, due to dependence on turbulence models even at the highest-fidelity CFD analysis, the data quality from testing in Figure 6.31 will not be the same. Moreover, the WT testing above is for a traditionally manufactured model using OFAT testing. Therefore, using DoE would further decrease the cost of WT testing by reducing the testing time. For aircraft design, the number of points is in the thousands even with DoE to populate the design space, which makes WT testing a good data generation technique since the cost does not increase with the number of design points tested in the figure above.

The acceptance of the WT SBO strategy is high due to cost and time saving techniques of DoE and AM models. When more accurate WT data can be acquired from a tunnel other than the Open-Jet WT, the WT SBO strategy should be fully effective for incorporation of WT data into an

aircraft conceptual design MDO. Future technologies and techniques for improving the effectiveness of a WT SBO strategy with AM models are presented in the following chapter.

# 7 Conclusions

An approach for incorporating AM and RP testing into an aircraft conceptual design MDO is developed in this work. Effectiveness is the measure used to determine whether WT data generated from AM models is feasible for aircraft conceptual design. A representative tailless configuration, ICE 101, is used to produce WT models for evaluation of the current SOTA in AM and RP technology. Furthermore, a SBO strategy, including DoE split-plot designs and RSMs, is modified for WT data incorporation.

## 7.1 AM Effectiveness

The current SOTA in FDM™ AM technology is not fully effective for ICE 101 WT model production. The thin wing tips of the ICE 101 configuration result in a scale model having thicknesses that are too small for FDM™ to manufacture. PolyJet technology would be able to produce parts with such thickness, but material strength is a concern for such a thin part produced using PolyJet. Alternative FDM™ model production methods are a topic of future work. The cost and time to produce models with AM are effective for incorporation into an MDO environment. Cost is reduced from tens of thousands of dollars to hundreds of dollars, and time is reduced from weeks and months to days. The future goal for cost and time reduction is a human out of the loop system that can AM a model, automatically post-process, and fix the model in a WT. When the challenges of thin wing tips for the ICE 101 model are overcome, AM should become fully effective for incorporation into an MDO environment.

## 7.2 SBO Effectiveness

The challenges of SBO effectiveness in this work come predominantly from data generation in the Open-Jet WT. The quality of data acquired results in an ineffective strategy; however, testing in a WT capable of more accurate moment data, while increasing testing cost, should result in a more effective SBO strategy for MDO. Development of DoE and RSM components of the SBO strategy will further improve the feasibility of SBO for aircraft conceptual design MDO.

With alternative AM methods for ICE 101 model production and more accurate WT testing, the WT SBO strategy developed in this work can be fully effective for WT incorporation into aircraft conceptual design MDO.

## 7.3 Future Work

The future areas of research are for making AM fully effective for the ICE 101 configuration and improving the effectiveness of the SBO strategy components. FDM™ technology can be used for production of carbon fiber models by producing an internal structure with FDM™ materials and then wrapping the structure with carbon fiber. This would improve the strength of the ICE 101 model and enable the thin wing tips to be machined down to the proper thickness. A concern with this method is ensuring dimensional accuracy of the model since post-processing steps will modify the AM geometry. Furthermore, this method will increase the cost and time by a factor of 2 or 3, but this is still a vast improvement from traditional manufacturing processes. Other potential improvements for AM model production are addition of electroactive polymer actuators and rubber-like materials for control surface deflections. Multi-material AM printers, like the Objet500 Connex3, can print materials with different properties that adhere to each other during printing. An example of this would be printing an airfoil with a plain flap which uses digital ABS material for the main body and flap, but the connection between the two bodies is made from a rubber-like material that is flexible. Furthermore, by adding an electroactive polymer internal to this model during printing would enable the flap to be actuated with addition of an electric field. The future goals for AM model production is the full production of a WT model which contains force and moment measurement sensors as well as actuated control surfaces for complete human out of the loop WT model production. A WT model with all of the needed sensors and actuators could be printed with AM and then immediately tested in a WT.

Future work for the WT SBO strategy investigates processes for DoE design and RSM selection. The number of levels required for each factor in an aircraft design problem is unknown. Engineering judgement must be used to determine the range that a specific factor should be tested; however, a process determining the number of levels for each factor, which impacts the DoE design, needs to be developed. The DoE design selected and generated has a large impact on how well an RSM will represent the true aircraft design space. Moreover, a process for selection of an RSM to fit the WT data is a topic of future work. If a RSM does not accurately represent the WT data, the optimum results from searching the RSM will not be accurate. Therefore, further work will investigate methods for generating RSMs to fit a data set without prior knowledge of how the data set. Future technological advancements in AM and improvements to the WT SBO strategy

are promising for a fully effective approach to incorporation of WT and RP testing for aircraft conceptual design. Once that is accomplished, the WT SBO strategy using AM will be applied to the design of a next-generation tailless aircraft configuration with a suite of innovative control effectors.

# Bibliography


[1] Allison, D. "Multidisciplinary Analysis and Design Optimization of an Efficient Supersonic Air Vehicle," Ph.D. Dissertation, Aerospace and Ocean Engineering Dept., Virginia Polytechnic Institute and State University, Blacksburg, Virginia, 2013.

[2] Morris, C. C. "Flight Dynamic Constraints in Conceptual Aircraft Multidisciplinary Analysis and Design Optimization," Ph.D. Dissertation, Aerospace and Ocean Engineering Dept., Virginia Polytechnic Institute and State University, Blacksburg, VA, 2013.

[3] Raj, P., and Friedman, A. M. "On timely and cost-effective prediction of aerodynamic data to meet aircraft design needs," presented at the RAeS Applied Aerodynamic Conference, Bristol, UK. 22-24 July 2014.

[4] Miranda, L. R. "Application of Computational Aerodynamics to Airplane Design," *Journal of Aircraft* Vol. 21, No. 6, pp. 355-370.

[5] Personal Communication, Choi, S., "CFD Analysis Times," 2014.

[6] Frink, N. T., Tormalm, M., and Schmidt, S. "Three Unstructured Computational Fluid Dynamics Studies on Generic Unmanned Combat Aerial Vehicle," *Journal of Aircraft* Vol. 49, No. 6, 2012, pp. 1619-1637.

[7] Personal Communication, Thomeer, P., "Budgetary Cost Estimate - Low Speed Wind Tunnel Model," Advanced Technologies Incorporated, 2015.

[8] (April 5, 2015) Leighton, T. "CFD and Wind Tunnel Testing: Complimentary Methods for Aircraft Design." Aeronautical Testing Service, Inc., 2014. Available: http://www.cd-adapco.com/sites/default/files/Presentation/Todd_Leighton.pdf.

[9] Kodama, H. "Automatic method for fabricating a three-dimensional plastic model with photo-hardening polymer," *Review of scientific instruments* Vol. 79, No. 11, 1981, pp. 1770-1773.

[10] Hull, C. W. "Apparatus For Production Of Three-Dimensional Objects By Stereolithography." Google Patents, 1986.

[11] Pham, D. T., and Gault, R. S. "A comparison of rapid prototyping technologies," *International Journal of Machine Tools and Manufacture* Vol. 38, 1997, pp. 1257-1287.

[12] (14 October 2014) "How PolyJet 3D Printing Works." Stratasys Ltd., 2014. Available: http://www.stratasys.com/3d-printers/technologies/polyjet-technology.

[13] Kim, G. D., and Oh, Y. T. "A benchmark study on rapid prototyping processes and machines: quantitative comparisons of mechanical properties, accuracy, roughness, speed, and material cost," *Proceedings of the Institution of Mechanical Engineers, Part B: Journal of Engineering Manufacture* Vol. 222, No. 2, 2008, pp. 201-215.

[14] (July 10, 2014) Fischer, F. "FDM and PolyJet 3d Printing: Determining which technology is right for your application." Stratasys Ltd., 2014. Available: http://www.stratasys.com/~/media/Main/Files/White%20Papers/SSYS-WP-SSYS-InkjetComparison-07-13.pdf.

[15] (July 12, 2014) Winker, R. "The Truth About Speed: Is the hare really fastest?." Stratasys Ltd. Available: http://www.stratasys.com/resources/~/media/5CA5D33C45C148F48C813DB2137EEC3C.pdf.

[16] Landrum, D. B., Beard, R. M., LaSarge, P. A., and von Sprecken, N. "Evaluation of stereolithography rapid prototyping for low speed airfoil design," presented at the 35th Aerospace Sciences Meeting & Exhibit, Reno, NV. Jan. 6-9, 1997. AIAA-97-0719.

[17] Heyes, A. L., and Smith, D. A. R. "Rapid Technique for Wind-Tunnel Model Manufacture," *Journal of Aircraft* Vol. 41, No. 2, 2004, pp. 413-415.

[18] Heisler, R. R., and Ratliff, C. L., "Wind Tunnel Model Design and Test Using Rapid Prototype Material Processes." Unclassified Proceedings. 2001. Report Number: ADP011186.

[19] Springer, A. "Evaluating Aerodynamic Characteristics of Wind-Tunnel Models Produced by Rapid Prototyping Methods," *Journal of Spacecraft and Rockets* Vol. 35, No. 6, 1998, pp. 755-759.

[20] Springer, A., and Cooper, K. "Comparing the Aerodynamic Characteristics of Wind Tunnel Models Produced by Rapid Prototyping and Conventional Methods," presented at the 15th Applied Aerodynamics Conference, Atlanta, GA. 1997. AIAA-97-2222.

[21] Springer, A. M., NASA, "Application of Rapid Prototyping Methods to High-Speed Wind Tunnel Testing." Marshall Space Flight Center, Alabama. May 1998. Report Number: NASA/TP—1998–208396.

[22] Nadooshan, A. A., Daneshmand, S., and Aghanajafi, C. "Evaluation of Surface Finish Affect on Aerodynamic Coefficients of Wind Tunnel RP Models Production with ABSi Material," *Materials Science Forum* Vol. 594, 2008, pp. 255-260.

[23] Hildebrand, R. J., Eidson, R. C., and Tyler, C. "Development of a Low Cost, Rapid Prototype Lambda Wing-Body Wind Tunnel Model," presented at the 21st Applied Aerodynamics Conference, Orlando, FL. June 23-26, 2003. AIAA-2003-3818.

[24] Gebbie, D. A., Reeder, M. F., Tyler, C., Fonov, V., and Crafton, J. "Lift and Drag Characteristics of a Blended-Wing Body Aircraft," *Journal of Aircraft* Vol. 44, No. 5, 2007, pp. 1409-1421.

[25] Gebbie, D. A., Reeder, M. F., Tyler, C., Fonov, V., and Crafton, J. "PSP-Based Experimental Investigation of a Blended Wing-Body Aircraft," presented at the 23rd AIAA Applied Aerodynamics Conference, Toronto, Ontario Canada. June 6-9, 2005. AIAA-2005-4719.

[26] Tyler, C., Braisted, W., and Higgins, J. "Evaluation of Rapid Prototyping Technologies for Use in Wind Tunnel Model Fabrication," presented at the 43rd AIAA Aerospace Sciences Meeting and Exhibit, Reno, NV. January 10-13, 2005. AIAA-2005-1301.

[27] Tyler, C., Reeder, M. F., Braisted, W., Higgins, J., and Gebbie, D. "Rapid Technology Focused Experimental and Computational Aerodynamic Investigation of a Strike Tanker," presented at the USAF Developmental Test and Evaluation Summit, Woodland Hills, CA. November 16-18, 2004. AIAA-2004-6870.

[28] Zhu, W., Zhao, X., Zhang, W., Ren, K., Zhang, Z., and Li, D. "Design and Evaluation of Fully Configured Models Built by Additive Manufacturing," *AIAA Journal* Vol. 52, No. 7, 2014, pp. 1441-1451.

[29] Artzi, D., and Kroll, E. "Lessons From Wind Tunnel Models Made By Rapid Prototyping," *Rapid Prototyping Journal* Vol. 17, No. 5, 2011.

[30] Kroll, E., and Artzi, D. "Enhancing aerospace engineering students' learning with 3D printing wind-tunnel models," *Rapid Prototyping Journal* Vol. 17, No. 5, 2011, pp. 393-402.

[31] Kroll, E., Artzi, D., and Ralbag, G. "Structural Design Guidelines for Wind Tunnel Models Made by Rapid Prototyping," presented at the 27th International Congress of the Aeronautal Sciences, Nice, France. September 19-24, 2010. ICAS 2010-3.2.4.

[32] Cummings, R., Schuette, A., and Huebner, A. "Overview of Stability and Control Estimation Methods from NATO STO Task Group AVT-201," presented at the 51st AIAA Aerospace Sciences Meeting, Grapevine (Dallas/Ft. Worth Region), Texas. 07-10 January 2013.

[33] Cummings, R. M. "Introduction: SACCON Unihabited Combat Aerial Vehicle Experimental and Numerical Simulations," *Journal of Aircraft* Vol. 49, No. 6, 2012, pp. 1541-1541.

[34] Cummings, R. M., and Schutte, A. "The NATO STO Task Group AVT-201 on 'Extended Assessment of Stability and Control Prediction Methods for NATO Air Vehicles'," presented at the 32nd AIAA Applied Aerodynamics Conference, Atlanta, GA. June 16-20, 2014. AIAA-2014-2000.

[35] Cummings, R. M., and Schütte, A. "Integrated Computational/Experimental Approach to Unmanned Combat Air Vehicle Stability and Control Estimation," *Journal of Aircraft* Vol. 49, No. 6, 2012, pp. 1542-1557.

[36] Loeser, T. D., Vicroy, D. D., and Schutte, A. "SACCON Static Wind Tunnel Tests at DNW-NWB and 14'x22' NASA LaRC," presented at the 28th AIAA Applied Aerodynamics Conference, Chicago, IL. June 28 - July 1, 2010. AIAA-2010-4393.

[37] Tomac, M., Rizzi, A., Nangia, R. K., Mendenhall, M. R., and Perkins, S. C. "Engineering Methods Applied to an Unmanned Combat Air Vehicle Configuration," *Journal of Aircraft* Vol. 49, No. 6, 2012, pp. 1610-1618.

[38] Vicroy, D. D., Loeser, T. D., and Schutte, A. "SACCON Forced Oscillation Tests at DNW-NWB and NASA Langley 14x22-Foot Tunnel," presented at the 28th AIAA Applied Aerodynamics Conference, Chicago, IL. June 28 - July 1, 2010.

[39] Dorsett, K. M., LMTAS, "Low-Speed Wind Tunnel Data Analysis of a 1/18th Scale Tailless Fighter." 1994. Report Number: ERR-FW-4323.

[40] Dorsett, K. M., and Mehl, D. R., AFRL, "Innovative Control Effectors (ICE)." LMTAS. 1996. Report Number: WL-TR-96-3043.

[41] Dorsett, K. M., Fears, S. P., and Houlden, H. P., AFRL, "Innovative Control Effectors (ICE) Phase II." LMTAS. 1997. Report Number: WL-TR-97-3059.

[42] Hammond, A. D., NASA, "Aerodynamic characteristics of a spoiler-slot-deflector control on a 45° sweptback-wing-fuselage model at high subsonic speeds." Langley Research Center, VA. 1957. Report Number: NASA TM X-205.

[43] Brown, A. E., and Hammond, A. D., NACA, "Results of an investigation at high subsonic speeds to determine lateral-control and hinge-moment characteristics of a spoiler-slot-deflector configuration on a 35 degree sweptback wing." Langley Aeronautical Lab, VA. 1957. Report Number: NACA RM L57C20.

[44] Vogler, R. D., NACA, "Wind-Tunnel Investigation at High Subsonic Speeds of a Spoiler-Slot-Deflector Combination on a NACA 65A006 Wing with Quarter-Chord Line Swept Back 32.6." Langley Aeronautical Laboratory, VA. 1953. Report Number: NACA RM L53D17.

[45] Queipo, N. V., Haftka, R. T., Shyy, W., Goel, T., Vaidyanathan, R., and Kevin Tucker, P. "Surrogate-based analysis and optimization," *Progress in Aerospace Sciences* Vol. 41, No. 1, 2005, pp. 1-28.

[46] Montgomery, D. C. *Design and Analysis of Experiments*. Hoboken, NJ: John Wiley & Sons, Inc., 2013.

[47] Rushing, H. *Design and Analysis of Experiments by Douglas Montgomery: A Supplement for Using JMP*: SAS Institute, 2013.

[48] DeLoach, R. "Formal Experimental Design in Wind Tunnel Testing at Langley Research Center," presented at the 46th Annual Fall Technical Conference of the American Society for Quality.

[49] DeLoach, R. "Analysis of Variance in the Modern Design of Experiments," presented at the 48th AIAA Aerospace Sciences Meeting, Orlando, FL. 4-7 Jan. 2010. AIAA-2010-1111.

[50] DeLoach, R., and Micol, J. "Analysis of Wind Tunnel Polar Replicates Using the Modern Design of Experiments (Invited)," presented at the 27th AIAA Aerodynamic Measurement Technology and Ground Testing Conference, Chicago, IL. 28 June - 1 July 2010. AIAA-2010-4927.

[51] DeLoach, R. "The Role of Hierarchy in Response Surface Modeling of Wind Tunnel Data," presented at the 48th AIAA Aerospace Sciences Meeting, Orlando, FL. 4-7 Jan. 2010. AIAA-2010-931.

[52] DeLoach, R. "Improved Quality in Aerospace Testing Through the Modern Design of Experiments," presented at the 38th Aerospace Sciences Meeting & Exhibit, Reno, Nevada. 10-13 Jan. 2000. AIAA-2000-825.

[53] DeLoach, R. "The Modern Design of Experiments for Configuration Aerodynamics: A Case Study," presented at the 44th AIAA Aerospace Sciences Meeting and Exhibit, Reno, NV. 9-12 Jan. 2006. AIAA-2006-923.

[54] DeLoach, R. "Blocking: A Defense Against Long-Period Unexplained Variance in Aerospace Ground Testing," presented at the 41st Aerospace Sciences Meeting and Exhibit, Reno, NV. 6-9 Jan. 2003. AIAA-2003-650.

[55] Dowgwillo, R., and DeLoach, R. "Using Modern Design of Experiments to Create a Surface Pressure Database From a Low Speed Wind Tunnel Test," presented at the 24th AIAA Aerodynamic Measurement Technology and Ground Testing Conference, Portland, OR. 28 June - 1 July 2004. AIAA-2004-2200.

[56] Jones, B., and Nachtsheim, C. "Split-Plot Designs: What, Why, and How," *Journal of Quality Technology* Vol. 41, No. 4, 2009, pp. 340 - 361.

[57] Goos, P., and Jones, B. "A Split-Plot Design," *Optimal Design of Experiments: A Case Study Approach*. Wiley, 2011.

[58] Goos, P., and Vanderbroek, M. "D-Optimal Split-Plot Designs With Given Numbers and Sizes of Whole Plots," *Technometrics* Vol. 45, No. 3, 2003, pp. 235-245.

[59] English, T. G., Simpson, J. R., Landman, D., and Parker, P. A. "An Efficient Split-Plot Approach for Modeling Nonlinear Aerodynamic Effects," *Quality Engineering* Vol. 24, No. 4, 2012, pp. 522-530.

[60] Parker, P., Kowalski, S. M., and Vining, G. G. "Classes of Split-Plot Response Surface Designs for Equivalent Estimation," *Quality and Reliability Engineering International* Vol. 22, No. 3, pp. 291 - 305.

[61] Parker, P. A., Kowalski, S. M., and Vining, G. G. "Construction of Balanced Equivalent Estimation Second-Order Split-Plot Designs," *Technometrics* Vol. 49, No. 1, 2007, pp. 56-65.

[62] Myers, R. H., Montgomery, D. C., and Anderson-Cook, C. M. *Response surface methodology: process and product optimization using designed experiments*. Hoboken, NJ: Wiley, 2009.
[63] Vining, G. G., and Kowalski, S. M. "Exact Inference for Response Surface Designs Within a Split-Plot Structure," *Journal of Quality Technology* Vol. 40, No. 4, 2008, pp. 394 - 406.
[64] Goos, P., and Gilmour, S. "Testing for Lack of Fit in Blocked and Split-Plot Response Surface Designs," 2012.
[65] Jones, B., and Goos, P. "I-Optimal Versus D-Optimal Split-Plot Response Surface Designs," *Journal of Quality Technology* Vol. 44, No. 2, 2012, pp. 85 - 101.
[66] Vining, G. G., Kowalski, S. M., and Montgomery, D. C. "Response Surface Designs Within a Split-Plot Structure," *Journal of Quality Technology* Vol. 37, No. 2, 2005, pp. 115 - 129.
[67] Letsinger, J., Myers, R. H., and Lentner, M. "Response Surface Methods for Bi-Randomization Structures," *Journal of Quality Technology* Vol. 28, No. 4, 1996, pp. 381 - 397.
[68] Khuri, A. I., and Mukhopadhyay, S. "Response Surface Methodology," *Wiley Interdisciplinary Reviews: Computational Statistics*. Vol. 2, 2010, pp. 128-149.
[69] (February 10, 2015) SAS. "JMP Pro." Available: http://www.jmp.com/en_us/software/jmp-pro.html.
[70] Cavazzuti, M. *Optimization Methods: From Theory to Scientific Design and Technological Aspects in Mechanics*: Springer Berlin Heidelberg, 2012.
[71] Foulds, L. R. *Optimization techniques: an introduction*. New York: Springer-Verlag, 1981.
[72] Hooker, J. *Integrated methods for optimization*: Springer, 2012.
[73] Rao, S. S. *Engineering optimization: theory and practice*. Hoboken, NJ: John Wiley & Sons, 2009.
[74] Rustagi, J. S. *Optimization Techniques in Statistics: A volume in Statistical Modeling and Decision Science*. Boston, MA: Academic Press, 1994.
[75] (March 17, 2015) MakerBot. "MakerBot Replicator 2: Specifications." Available: http://downloads.makerbot.com/replicator2/MakerBot_Replicator2_brochure.pdf.
[76] (March 17, 2015) MakeItFrom.com. "Polylactic Acid (PLA) Material Properties." Available: http://www.makeitfrom.com/material-properties/Polylactic-Acid-PLA-Polylactide/.
[77] (March 17, 2015) MatWeb.com. "6061 Aluminum Material Property Data Sheet." Available: http://elginfasteners.com/resources/raw-material-technical-data-specifications/6061-aluminum-material-property-data-sheet/.
[78] (March 17, 2015) Ltd., S. "uPrint SE Plus Specifications." Available: http://www.stratasys.com/3d-printers/idea-series/uprint-se-plus.
[79] (March 17, 2015) Ltd., S. "ABSplus-P430." Available: http://www.stratasys.com/~/media/Main/Secure/Material%20Specs%20MS/Fortus-Material-Specs/Fortus-MS-ABSplus-01-13-web.pdf.
[80] (March 17, 2015) Ltd., S. "ABS-M30." Available: http://www.stratasys.com/~/media/Main/Secure/Material%20Specs%20MS/Fortus-Material-Specs/FortusABSM30MaterialSpecSheet-US-09-14-Web.pdf.
[81] (March 17, 2015) Ltd., S. "Fortus 360mc and 400mc Product Specs." Available: http://www.stratasys.com/3d-printers/production-series/fortus-360-400mc.

[82] (March 17, 2015) Ltd., S. "Objet30 Pro Specifications." Available: http://www.stratasys.com/3d-printers/design-series/objet30-pro.
[83] (March 17, 2015) Ltd., S. "PolyJet Materials Data Sheet: Rigid Opaque Materials." 2013. Available: http://www.stratasys.com/~/media/Main/Secure/Material%20Specs%20MS/PolyJet-Material-Specs/PolyJet_Materials_Data_Sheet.pdf.
[84] (March 17, 2015) Ltd., S. "Connex3 Systems Specifications." Available: http://www.stratasys.com/3d-printers/production-series/connex3-systems.
[85] Personal Communication, Blake, B., "ICE 101 CAD Geometry," 2014.
[86] "Virginia Tech Stability Wind Tunnel - Instrumentation: Forces and Moments." Available: http://www.aoe.vt.edu/research/facilities/stabilitytunnel/instrumentation-stabilitytunnel.html.
[87] (April 8, 2015) Ltd., S. "Fortus 900mc Product Specs." Available: http://www.stratasys.com/3d-printers/production-series/fortus-900mc.
[88] (April 8, 2015) Ltd., S. "Objet1000 3D Printer Specifications." Available: http://www.stratasys.com/3d-printers/production-series/objet1000-plus.
[89] Personal Communication, Wolf, J., "AM of the ICE 101 1/15th Scale Model," Stratasys Direct Manufacturing, 2015.
[90] Forrester, A. I. J., Keane, A. J., and Bressloff, N. W. "Optimization using surrogate models and partially converged computational fluid dynamics simulations," *Proceedings of the Royal Society A: Mathematical, Physical and Engineering Sciences* Vol. 462, No. 2071, 2006, pp. 2177-2204.
[91] Personal Communication, Snyder, R., "A Toolkit for Trim," 2015.
[92] Jacobs, E., and Sherman, A., NACA, "Airfoil Section Characteristics as Affected by Variations of the Reynolds Number." Langley Aeronautics Laboratory, VA. Report Number: NACA TR 586.
[93] Ashby, D. L., NASA, "Experimental and Computational Investigation of Lift-Enhancing Tabs on a Multi-Element Airfoil." NASA Ames Research Center, CA. 1996. Report Number: NASA TM 110432.
[94] Melin, T. "A Vortex Lattice MATLAB Implementation for Linear Aerodynamic Wing Applications," M.S. Thesis, Aeronautics Dept., Royal Institute of Technology (KTH), 2000.
[95] Fang, K., Li, R.-z., and Sudjianto, A. "Latin Hypercube Sampling and Its Modifications," *Design and modeling for computer experiments*. Chapman & Hall/CRC, Boca Raton, FL, 2006.
[96] Young, A. D., ARC, "The Aerodynamic Characteristics of Flaps." London, England. 1947. Report Number: RAE-TM-AERO-2185.
[97] Ames, M., and Sears, R., NACA, "Determination of Control-Surface Characteristics from NACA Plain-Flap and Tab Data." Langley Aeronautical Laboratory, VA. 1941. Report Number: NACA TR 721.
[98] Abbott, I. H., and von Doenhoff, A. E. *Theory of Wing Sections, Including a Summary of Airfoil Data*. New York: Dover Publications, 1959.
[99] Barlow, J. B., Rae, W. H., and Pope, A. *Low-speed wind tunnel testing*. New York: Wiley, 1999.
[100] (October 14, 2014) "0.7m Subsonic Open Jet Wind Tunnel." Virginia Tech. Available: http://www.aoe.vt.edu/research/facilities/openjet.html.

[101] Brooks, T. F., Marcolini, M. A., and Pope, D. S. "Airfoil trailing edge flow measurements and comparison with theory incorporating open wind tunnel corrections," presented at the AIAA/NASA 9th Aeroacoustics Conference, Williamsburg, Virginia. October 15-17, 1984. AIAA-84-2266.

[102] Brooks, T. F., Marcolini, M. A., and Pope, D. S. "Airfoil trailing-edge flow measurements," *AIAA Journal* Vol. 24, No. 8, 1986, pp. 1245-1251.

# Appendix A Split-Plot Designs: ICE 101 LMTAS Data & NACA 0012

| Run # | WP # | AMT | AoA |
|---|---|---|---|
| **1** | 1 | -1 | 0 |
| **2** | 1 | -1 | -1 |
| **3** | 1 | -1 | 1 |
| **4** | 2 | 0 | 0.16 |
| **5** | 2 | 0 | 0 |
| **6** | 2 | 0 | -1 |
| **7** | 3 | 1 | -1 |
| **8** | 3 | 1 | 0 |
| **9** | 3 | 1 | 1 |
| **10** | 4 | 0 | 0 |
| **11** | 4 | 0 | 1 |
| **12** | 4 | 0 | 0 |

**Table A.1: $C_N$ & $C_m$ data 1st design.**

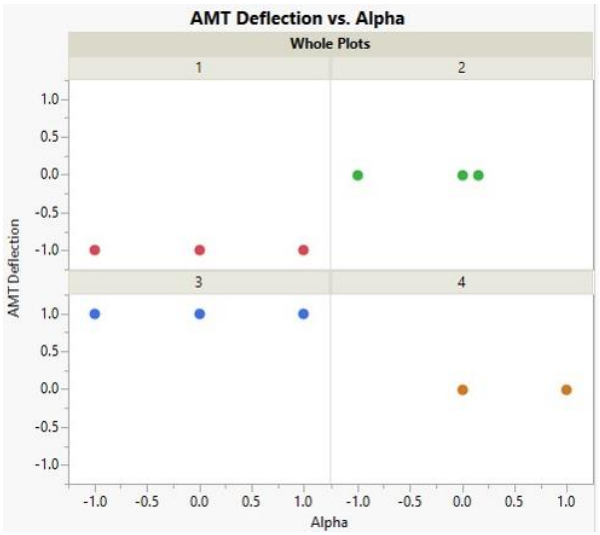


**Figure A.1:Visualization of $C_N$ & $C_m$ 1st design.**

| Run # | WP # | AMT | AoA |
|---|---|---|---|
| **1** | 1 | 0 | -1 |
| **2** | 1 | 0 | 0.6667 |
| **3** | 1 | 0 | -0.3333 |
| **4** | 1 | 0 | -0.3333 |
| **5** | 1 | 0 | 0.6667 |
| **6** | 2 | 1 | -0.6667 |
| **7** | 2 | 1 | 0 |
| **8** | 2 | 1 | 1 |
| **9** | 2 | 1 | -1 |
| **10** | 2 | 1 | 0.6667 |
| **11** | 3 | -1 | -0.6667 |
| **12** | 3 | -1 | 0 |
| **13** | 3 | -1 | -1 |
| **14** | 3 | -1 | 0.6667 |
| **15** | 3 | -1 | 1 |
| **16** | 4 | 0 | 1 |
| **17** | 4 | 0 | 1 |
| **18** | 4 | 0 | 0.3333 |
| **19** | 4 | 0 | -0.3333 |
| **20** | 4 | 0 | -0.6667 |

**Table A.2: $C_N$ & $C_m$ data 2nd design.**

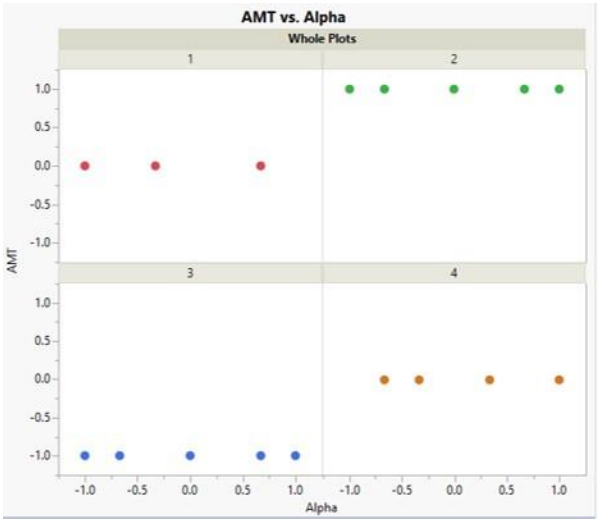


**Figure A.2: Visualization of $C_N$ & $C_m$ 2nd design.**

| Run # | WP # | AMT | AoA | Run # | WP # | AMT | AoA |
|---|---|---|---|---|---|---|---|
| **1** | 1 | -1 | 0.6 | **21** | 3 | 0 | -0.6 |
| **2** | 1 | -1 | 1 | **22** | 3 | 0 | 0.6 |
| **3** | 1 | -1 | -0.6 | **23** | 3 | 0 | 0.6 |
| **4** | 1 | -1 | 1 | **24** | 3 | 0 | 1 |
| **5** | 1 | -1 | -0.6 | **25** | 3 | 0 | -0.4 |
| **6** | 1 | -1 | -1 | **26** | 3 | 0 | -1 |
| **7** | 1 | -1 | -1 | **27** | 3 | 0 | 0 |
| **8** | 1 | -1 | 0.4 | **28** | 3 | 0 | 0.6 |
| **9** | 1 | -1 | -0.4 | **29** | 3 | 0 | -0.6 |
| **10** | 1 | -1 | 0.6 | **30** | 3 | 0 | 0 |
| **11** | 2 | 0 | 0 | **31** | 4 | 1 | -0.6 |
| **12** | 2 | 0 | 0.6 | **32** | 4 | 1 | 0.4 |
| **13** | 2 | 0 | -0.6 | **33** | 4 | 1 | 0.6 |
| **14** | 2 | 0 | 0.6 | **34** | 4 | 1 | 1 |
| **15** | 2 | 0 | -1 | **35** | 4 | 1 | 1 |
| **16** | 2 | 0 | 0 | **36** | 4 | 1 | -1 |
| **17** | 2 | 0 | 0.4 | **37** | 4 | 1 | -1 |
| **18** | 2 | 0 | -0.6 | **38** | 4 | 1 | -0.4 |
| **19** | 2 | 0 | 1 | **39** | 4 | 1 | -0.6 |
| **20** | 2 | 0 | -0.6 | **40** | 4 | 1 | 0.6 |

**Table A.3: $C_N$ & $C_m$ data 3rd design.**

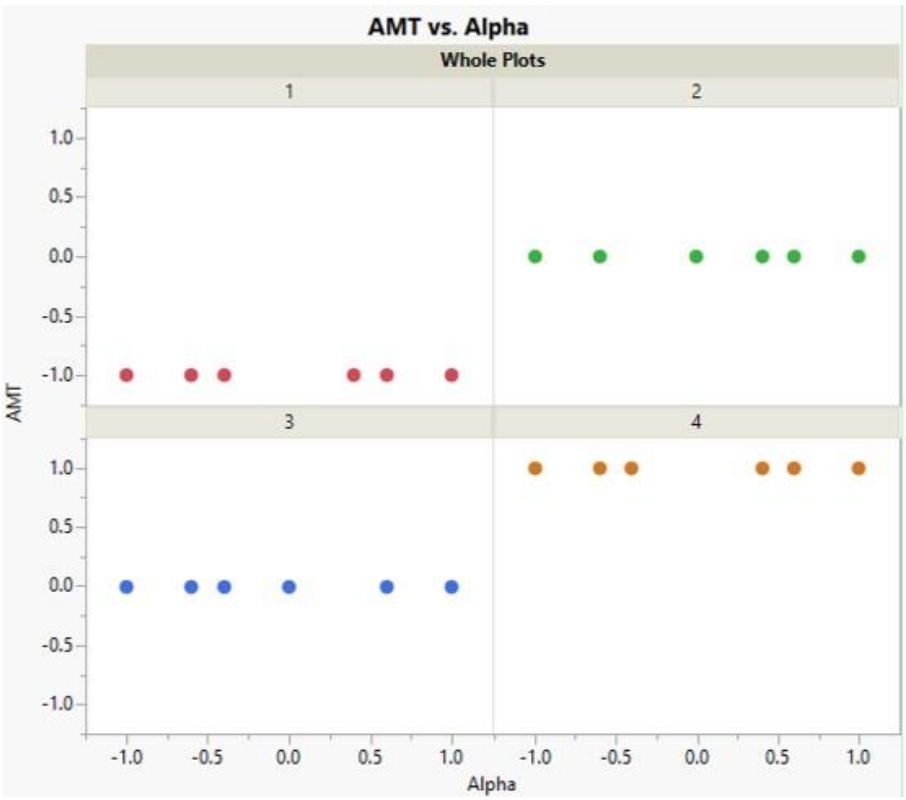


**Figure A.3: Visualization of $C_N$ & $C_m$ 3rd design.**

| Run # | WP # | AMT | AoA |
|---|---|---|---|
| **1** | 1 | 0 | -1 |
| **2** | 1 | 0 | 0.6667 |
| **3** | 1 | 0 | -0.3333 |
| **4** | 1 | 0 | -0.3333 |
| **5** | 1 | 0 | 0.6667 |
| **6** | 2 | 1 | -0.6667 |
| **7** | 2 | 1 | 0 |
| **8** | 2 | 1 | 1 |
| **9** | 2 | 1 | -1 |
| **10** | 2 | 1 | 0.6667 |
| **11** | 3 | -1 | -0.6667 |
| **12** | 3 | -1 | 0 |
| **13** | 3 | -1 | -1 |
| **14** | 3 | -1 | 0.6667 |
| **15** | 3 | -1 | 1 |
| **16** | 4 | 0 | 1 |
| **17** | 4 | 0 | 1 |
| **18** | 4 | 0 | 0.3333 |
| **19** | 4 | 0 | -0.3333 |
| **20** | 4 | 0 | -0.6667 |

**Table A.4: $C_l$ & $C_n$ data 1st design.**

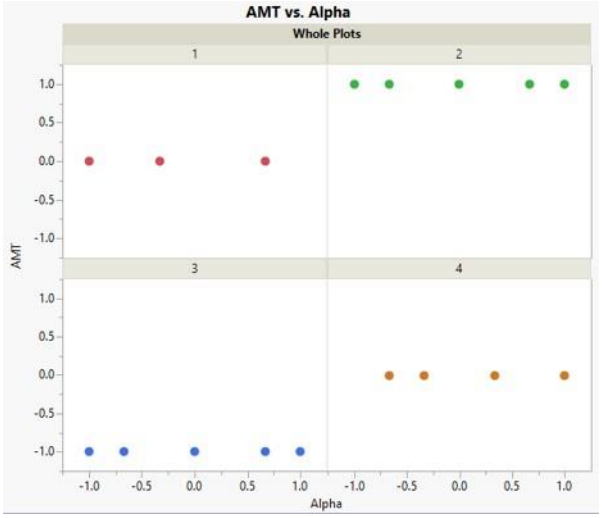


**Figure A.4: Visualization of $C_l$ & $C_n$ 1st design.**

| Run # | WP # | AMT | AoA | Run # | WP # | AMT | AoA |
|---|---|---|---|---|---|---|---|
| **1** | 1 | 0 | -1 | **21** | 5 | -0.5 | 1 |
| **2** | 1 | 0 | 0.667 | **22** | 5 | -0.5 | -0.333 |
| **3** | 1 | 0 | -0.333 | **23** | 5 | -0.5 | -0.333 |
| **4** | 1 | 0 | -0.333 | **24** | 5 | -0.5 | -0.333 |
| **5** | 1 | 0 | 0.333 | **25** | 5 | -0.5 | -1 |
| **6** | 2 | 0.5 | 0.667 | **26** | 6 | 0.5 | 1 |
| **7** | 2 | 0.5 | -0.333 | **27** | 6 | 0.5 | -0.667 |
| **8** | 2 | 0.5 | 0.667 | **28** | 6 | 0.5 | 0.333 |
| **9** | 2 | 0.5 | -1 | **29** | 6 | 0.5 | 0.333 |
| **10** | 2 | 0.5 | -0.333 | **30** | 6 | 0.5 | -0.667 |
| **11** | 3 | -0.5 | -0.667 | **31** | 7 | -1 | 0.667 |
| **12** | 3 | -0.5 | -0.667 | **32** | 7 | -1 | 0.333 |
| **13** | 3 | -0.5 | -0.667 | **33** | 7 | -1 | -1 |
| **14** | 3 | -0.5 | 0.333 | **34** | 7 | -1 | 1 |
| **15** | 3 | -0.5 | 1 | **35** | 7 | -1 | -0.667 |
| **16** | 4 | 1 | 0 | | | | |
| **17** | 4 | 1 | 0.667 | | | | |
| **18** | 4 | 1 | -1 | | | | |
| **19** | 4 | 1 | -0.667 | | | | |
| **20** | 4 | 1 | 1 | | | | |

**Table A.5: $C_l$ & $C_n$ data 2nd and 3rd designs.**

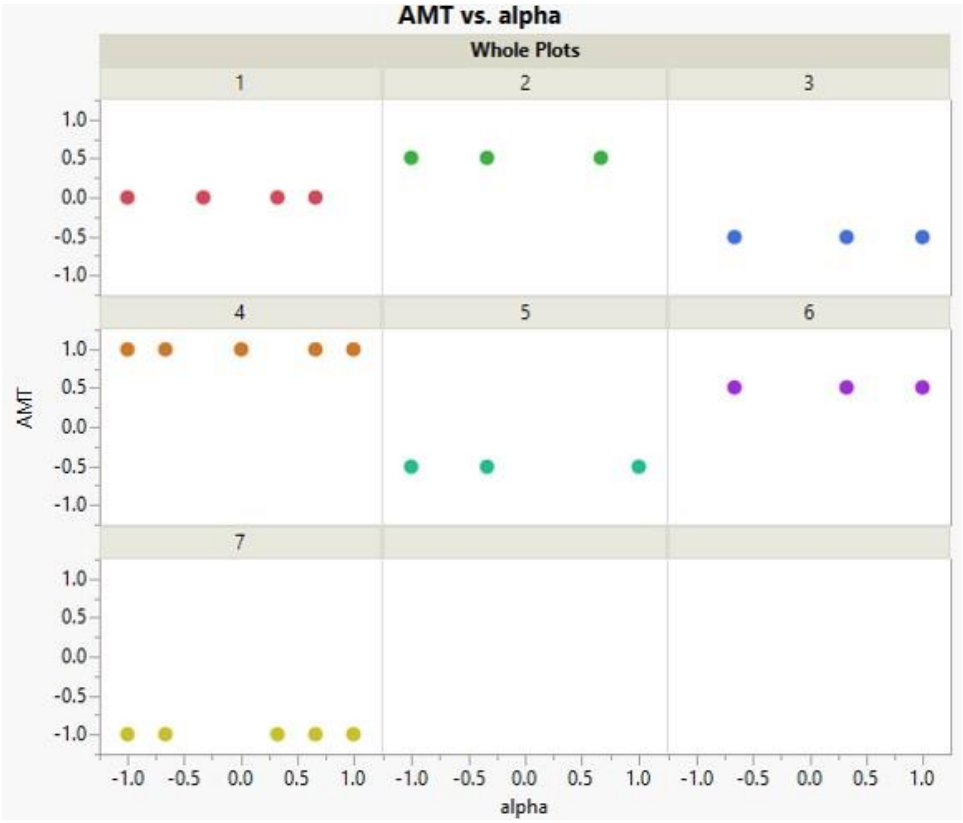


**Figure A.5: Visualization of $C_l$ & $C_n$ data for 2nd and 3rd designs..**

| Run # | WP # | AMT delta | AoA | AMT size | Run # | WP # | AMT delta | AoA | AMT size |
|---|---|---|---|---|---|---|---|---|---|
| **1** | 1 | 0.5 | 0 | 0.3333 | **26** | 6 | 1 | -1 | 0.0000 |
| **2** | 1 | 0.5 | 0 | -0.6667 | **27** | 6 | 1 | -1 | -1.0000 |
| **3** | 1 | 0.5 | 0 | 1.0000 | **28** | 6 | 1 | -1 | -0.6667 |
| **4** | 1 | 0.5 | 0 | 1.0000 | **29** | 6 | 1 | -1 | 1.0000 |
| **5** | 1 | 0.5 | 0 | 0.3333 | **30** | 6 | 1 | -1 | 0.6667 |
| **6** | 2 | 0.5 | 0 | -0.6667 | **31** | 7 | -0.5 | 0 | 0.6667 |
| **7** | 2 | 0.5 | 0 | 0.6667 | **32** | 7 | -0.5 | 0 | 0.3333 |
| **8** | 2 | 0.5 | 0 | 0.0000 | **33** | 7 | -0.5 | 0 | -0.3333 |
| **9** | 2 | 0.5 | 0 | 0.6667 | **34** | 7 | -0.5 | 0 | -1.0000 |
| **10** | 2 | 0.5 | 0 | -0.6667 | **35** | 7 | -0.5 | 0 | -0.3333 |
| **11** | 3 | 0 | -1 | 1.0000 | **36** | 8 | 1 | 1 | 1.0000 |
| **12** | 3 | 0 | -1 | -0.6667 | **37** | 8 | 1 | 1 | -1.0000 |
| **13** | 3 | 0 | -1 | -1.0000 | **38** | 8 | 1 | 1 | -0.6667 |
| **14** | 3 | 0 | -1 | 0.0000 | **39** | 8 | 1 | 1 | 0.6667 |
| **15** | 3 | 0 | -1 | 0.0000 | **40** | 8 | 1 | 1 | 0.0000 |
| **16** | 4 | -1 | 1 | 1.0000 | **41** | 9 | 0 | 1 | 0.0000 |
| **17** | 4 | -1 | 1 | -1.0000 | **42** | 9 | 0 | 1 | -1.0000 |
| **18** | 4 | -1 | 1 | 0.0000 | **43** | 9 | 0 | 1 | 0.0000 |
| **19** | 4 | -1 | 1 | 0.6667 | **44** | 9 | 0 | 1 | 0.0000 |
| **20** | 4 | -1 | 1 | -0.6667 | **45** | 9 | 0 | 1 | 1.0000 |
| **21** | 5 | -1 | -1 | -1.0000 | **46** | 10 | -0.5 | 0 | -0.6667 |
| **22** | 5 | -1 | -1 | -0.3333 | **47** | 10 | -0.5 | 0 | 0.6667 |
| **23** | 5 | -1 | -1 | -0.6667 | **48** | 10 | -0.5 | 0 | 0.6667 |
| **24** | 5 | -1 | -1 | 1.0000 | **49** | 10 | -0.5 | 0 | 0.0000 |
| **25** | 5 | -1 | -1 | 0.6667 | **50** | 10 | -0.5 | 0 | -0.6667 |

**Table A.6: ICE 101 LMTAS AMT three factor design.**

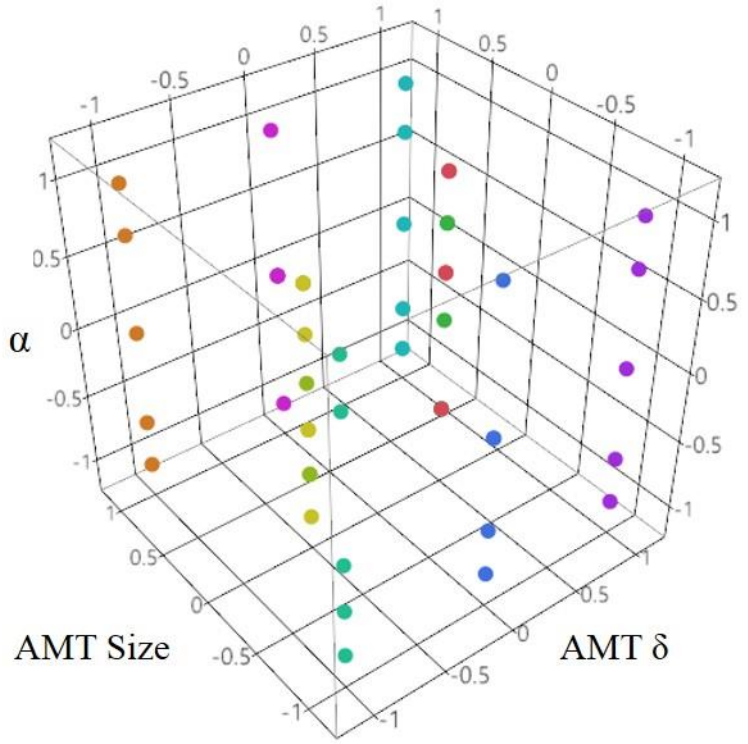


**Figure A.6: ICE 101 LMTAS AMT three factor design space.**

| Run # | WP # | Delta | AoA | Run # | WP # | Delta | AoA |
|---|---|---|---|---|---|---|---|
| **1** | 1 | 0 | -1 | **21** | 5 | -0.5 | 1 |
| **2** | 1 | 0 | 0.667 | **22** | 5 | -0.5 | -0.333 |
| **3** | 1 | 0 | -0.333 | **23** | 5 | -0.5 | -0.333 |
| **4** | 1 | 0 | -0.333 | **24** | 5 | -0.5 | -0.333 |
| **5** | 1 | 0 | 0.333 | **25** | 5 | -0.5 | -1 |
| **6** | 2 | 0.5 | 0.667 | **26** | 6 | 0.5 | 1 |
| **7** | 2 | 0.5 | -0.333 | **27** | 6 | 0.5 | -0.667 |
| **8** | 2 | 0.5 | 0.667 | **28** | 6 | 0.5 | 0.333 |
| **9** | 2 | 0.5 | -1 | **29** | 6 | 0.5 | 0.333 |
| **10** | 2 | 0.5 | -0.333 | **30** | 6 | 0.5 | -0.667 |
| **11** | 3 | -0.5 | -0.667 | **31** | 7 | -1 | 0.667 |
| **12** | 3 | -0.5 | -0.667 | **32** | 7 | -1 | 0.333 |
| **13** | 3 | -0.5 | -0.667 | **33** | 7 | -1 | -1 |
| **14** | 3 | -0.5 | 0.333 | **34** | 7 | -1 | 1 |
| **15** | 3 | -0.5 | 1 | **35** | 7 | -1 | -0.667 |
| **16** | 4 | 1 | 0 | | | | |
| **17** | 4 | 1 | 0.667 | | | | |
| **18** | 4 | 1 | -1 | | | | |
| **19** | 4 | 1 | -0.667 | | | | |
| **20** | 4 | 1 | 1 | | | | |

**Table A.7: NACA 0012 WT testing design.**

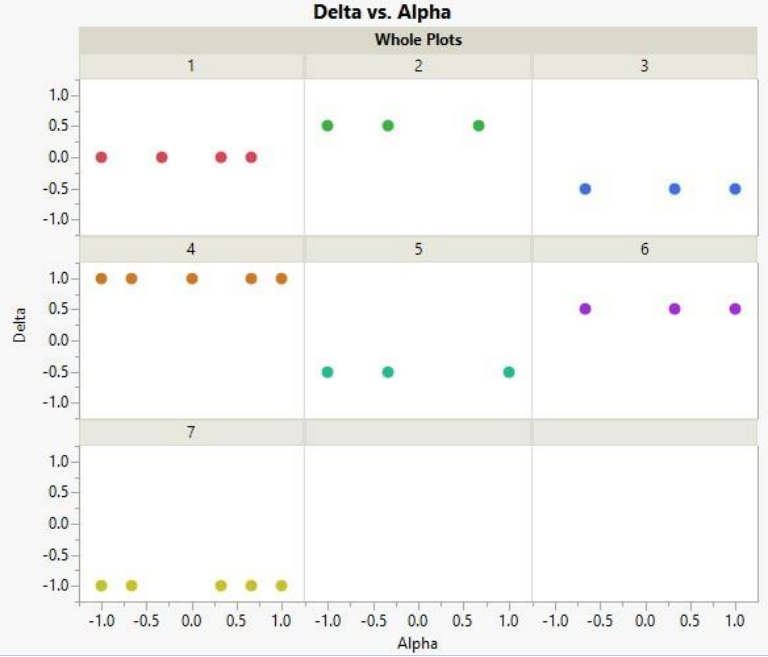


**Figure A.7: Graphical representation of NACA 0012 WT testing design.**

# Appendix B Open-Jet WT and Corrections

## B.1 Facilities and Testing Setup

The Open-Jet WT of the AOE department at VT has been selected for testing of the AM models in this work. The tunnel consists of a 0.7 m square open test section and can be operated at a max flow speed of approximately 27 m/s. The tunnel is readily available, easy to use, and has a low operation cost. Furthermore, the model will be tested using a six-axis strut mounted strain gage balance for determining the forces and moments on the aircraft while in the flow [100].

**Figure B.1: VT AOE department Open-Jet WT. (October 14, 2014) "0.7m Subsonic Open Jet Wind Tunnel." Virginia Tech. Available: http://www.aoe.vt.edu/research/facilities/openjet.html. Used under fair use, 2015.**

## B.2 WT Corrections

Brooks *et al* [101, 102] use lifting surface theory for two-dimensional Open-Jet WT corrections. The analysis takes into account the curvature of tunnel flow on the effective camber shape of the airfoil. However, streamwise buoyancy (due to any tunnel static pressure variation) and lateral constraint effects (due to flow blocking of the model) were ignored. Note that the corrections presented by Brooks *et al* are for an open test section with walled sides but open top and bottom. However, these corrections can still be applied to a fully open test section with good results. The Open-Jet corrections to apply are as follows:

$$\sigma = \left(\frac{\pi^2}{48}\right)\left(\frac{c}{H}\right)^2, \tag{B.1}$$

$$\zeta = (1+2\sigma)^2 + \sqrt{12\sigma}, \tag{B.2}$$

$$\alpha_* = \frac{\alpha_t}{\zeta}\ , \tag{B.3}$$

where $c$ is the model chord, $H$ is the tunnel height*, $\alpha_t$ is the tunnel AoA, and $\alpha_*$ is the corrected AoA. Note that $H$ is the tunnel height if the model is placed in the exact center of the flow. Also, $H$ is the clean flow of the tunnel.

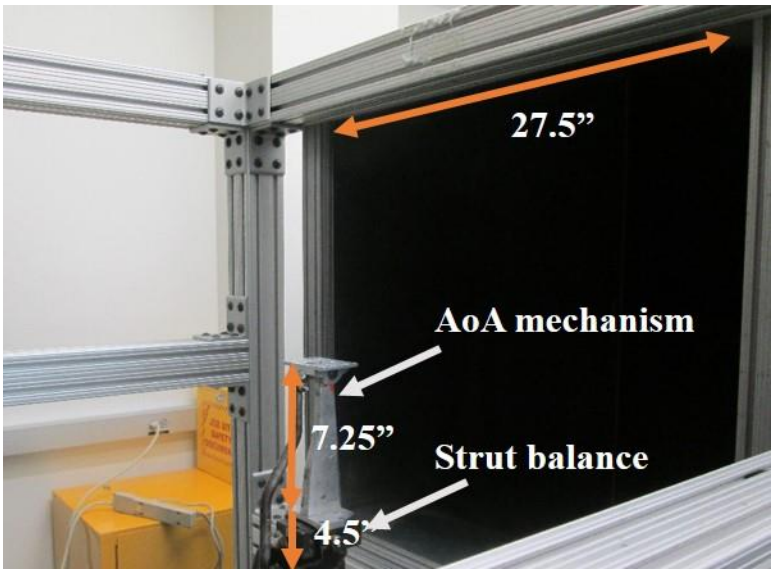


**Figure B.2: Open-Jet WT with AoA mechanism attached to strut balance.**

In the case of the VT Open-Jet WT, $H = 26.5$” with the strut balance and the AoA mounting attachment in the tunnel. H was decreased by 1” to account for the region of clean flow in the tunnel. If a model is placed away from the center and since the correction derivation uses the method of images, the effective tunnel height is 26.5” – 2*(distance from the tunnel center). For this work with a chord of 6”, the ζ correction value is 1.3983. Each time a new model is tested, measurements should be made to locate the position of the model relative to the tunnel center. Another correction applied to AoA is due to the “slop” in the AoA mechanism. The age of the AoA mechanism has resulted in considerable movement. Therefore, with the use of a digital protractor, the resulting “slop” correction added to the AoA, after the above correction, is 0.8°.

Figure B.2 shows the dimensions for the AoA mechanism and the distance from the top of the strut balance to the force measurement location of the balance, 7.25” and 4.5”, respectively. Furthermore, the vertical distance to the center of the model must be accounted for, 0.5” in the case of this work for the NACA 0012 model. To move the pitching moment location, the drag must first be corrected. The coordinate system shown by the data acquisition system shows normal

and axial forces instead of lift and drag. However, these are normal and axial forces of the balance coordinate system and not the body fixed coordinate system. Therefore, the normal and axial forces of the balance are lift and drag of the model. The drag due to the strut balance is not possible to determine for the current strut configuration. A close approximation can be made by determining the drag on the balance alone without a model. However, this is not a true representation of the drag due to the balance since there are no interaction effects with the model. The methods presented in Barlow *et al* [99] for determining balance drag corrections are helpful for coming up with a method for estimating drag due to the balance that is as close as a full representation as possible.

For this work, the drag (axial force from the balance) correction applied is approximately 4.2 N. The drag correction is important for this work due to the need to transform the pitching moment from the balance moment center to the quarter chord of the model. The NACA 0012 model of this work was designed so that the mounting plate was centered on the quarter chord of the model, resulting in the only needed shift being the pitching moment due to drag. Finally, as noted above, the pitching moment was corrected by subtracting 12.25" multiplied by the corrected drag (axial of the balance) force.

In summary, the corrections to apply to the VT Open-Jet WT data are AoA corrections from Brooks *et al*, a correction to the drag (axial of the balance) force, and a transformation of the moment from the moment center of the balance to the moment center of the model.